UNIVERSITÀ DEGLI STUDI DI PADOVA

DIPARTIMENTO DI BIOLOGIA

Corso di Laurea magistrale in Molecular Biology

TESI DI LAUREA

Anatomical, behavioral and functional characterization of novel zebrafish mutant lines for *nlgn2*, a high confidence ASD risk-gene

Relatore: Prof. Marco Dal Maschio
Dipartimento di Scienze Biomediche
Università degli Studi di Padova

Correlatore: Prof. Nicola Facchinello
CNR- Istituto di Neuroscienze

Laureando: Alessandro Tollardo

ANNO ACCADEMICO 2025/2026

SUMMARY

1. ABSTRACT

Neuroligin-2 (NLGN2) is a postsynaptic structural component of GABAergic synapses, and it is predicted as high-confidence autism spectrum disorder risk-gene. To investigate the relevance of this gene in the development of the brain circuits and functions, two newly-generated CRISPR-CAS9 *nlgn2(a/b)* mutant lines were characterized focusing on viability, neuronal anatomy and functional aspects. Both *nlgn2* mutant fish exhibit decreased survival rate, gross anatomical alterations in head morphometry and body length. From the functional point of view, mutant fish show alterations in basic photo-response and in the *nlgn2a* brain activity, with higher power in the infra-slow range (<0.1 Hz). At the anatomical level, in *nlgn2a* mutants, the population of periventricular pyramidal neurons in the tectum show differences in dendritic spine densities, retinotopic areas and neuronal branching properties. An electron microscopy analysis revealed a reduced extension of the active zones at the synapse for both mutants. To better characterize the spatial distribution of PSD95- and gephyrin-positive synapses during development, two Gal4/UAS-transgenic lines were established. In parallel, a transcriptomic analysis highlighted differential expression patterns for genes involved in synaptic and axonal structural organization. In conclusion, the developed approaches allowed to identify a number of alterations consistent with the pathological traits of a neurodevelopmental disease.

2. INTRODUCTION

2.1.Autism Spectrum Disorder

Autism Spectrum Disorder (ASD) is a neurodevelopmental multifactorial condition that affects 3.2% of children aged 8 years and is reportedly over 3 times more common among boys than among girls in the U.S.[1] In adults, the prevalence estimate is approximately 2.21% [1].In Italy, the percentage is 1.34% in children aged 7-9 years, with a male-to-female ratio of 4:1 [2].

ASD prevalence has increased over time, and factors such as diagnostic criteria, awareness of the condition and greater access to services could have contributed to this. As the name suggests, this condition shows a broad diversity of symptoms with high degree of severity, ranging from repetitive behaviors, communication impairments, intellectual disabilities, restricted interests, to difficulties in adhering to prescribed or social rules [4].Also, language disorders and medical and psychiatric conditions (i.e. epilepsy, depression, sleep disorders) are common.

ASD is diagnosed mainly through clinical interviews and behavioral observations. The American Psychiatric Association (APA) Diagnostic and Statistical Manual of Mental Disorders (DSM-5) is used in the U.S. as diagnostic tool for ASD and is defined by two main domains with several sub-domains and severity levels[2]:

1) Social communication and interaction differences
2) Restricted, repetitive patterns of behavior or interests

The absence of validated biomarkers underlies the importance of behavioral-based diagnostic tools [4].

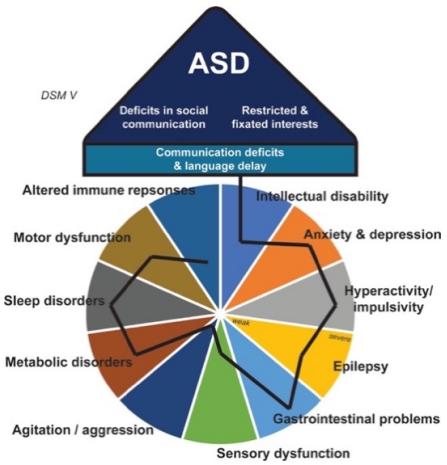

***Figure 1**: **Overview and clinical features of ASD** [5]. Among the most severe dysfunctions, intellectual disability, altered emotional states, epilepsy, gastrointestinal problems, metabolic and sleep disorders and motor dysfunction.*

[1] According to estimates from U.S. Centers for Disease Control and Prevention (CDC) Autism and Developmental Disabilities Monitoring (ADDM) Network (www.cdc.gov), updated April 2025.
[2] A detailed explanation of the DSM-5 manual is available on www.autismspeaks.org

To alleviate symptoms and improve quality of life, there is a range of clinical and pharmacological treatments, although there's no definitive cure for ASD now.
Treatments comprise behavioral and educational interventions that aim to improve behavioral and social dysfunctions typical of the condition. Applied Behavioral Analysis (ABA) is a highly individualized technique based on behavioral psychology that starts from a detailed behavioral assessment followed by tailored intervention strategies. Learned behaviors are then reinforced through one-to-one lessons. Along ABA strategy, also Social Skill Training (SST) is useful in cases where social behaviors and patterns are altered and has been shown to be significantly effective in restoration of interpersonal interactions in ASD.
Along with these, also pharmacological treatments can be used as adjunctive interventions to manage psychological symptoms associated with ASD, as mentioned before. The main agents are antipsychotics for irritability and aggression, antidepressants and anxiolytics and melatonin for mood and sleep disturbances [6].

2.1.1. ASD-risk genes

The clinical heterogeneity of ASD emerges from a contribution of genetic, developmental and environmental factors. Genome-wide association studies (GWAS) based on the Psychiatric Consortium Major Depression (PCMD) dataset showed that genetic contribution, the strongest one, accounts for ~80% in ASD emergence, while environmental factors range between 14% and 22% [7].
Focusing on the genetic component, there are three main categories of genetic risks: common polygenic variations, rare inherited and *de novo* mutations (DNVs) [8].
While common polygenic variation can affect the susceptibility to ASD, DNVs, although rarer, are major contributors to the disorder.
A relatively small number of genes (~100) are associated with significant risk, while a much larger number comprises genes which are characterized by a lower risk alone but, when in combination with each other, show additive features and account for the majority of cases [9].

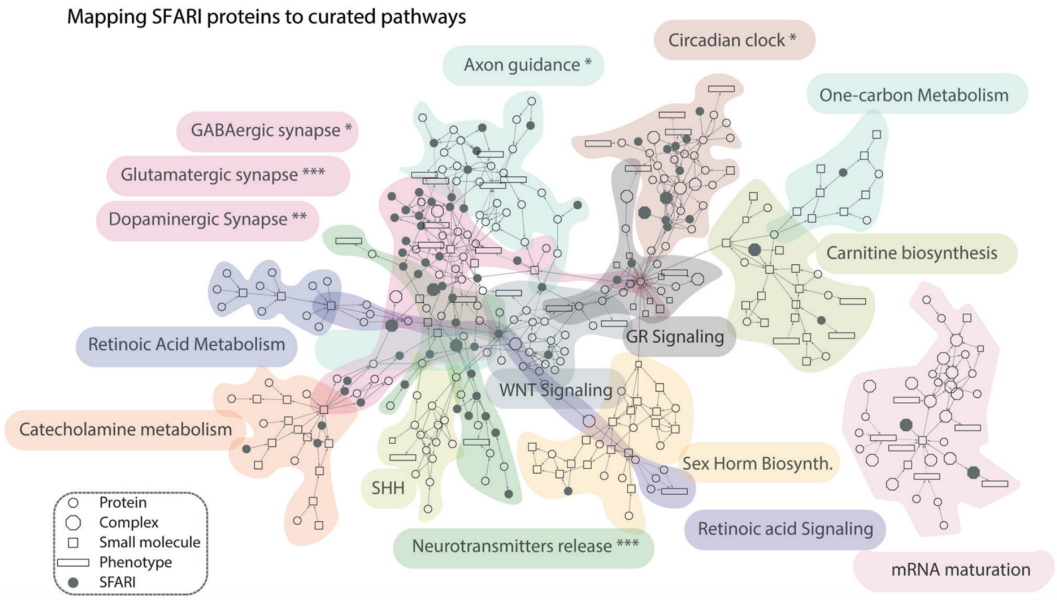

***Figure 2**:Scaffold network of biological pathways of neurological relevance curated in SIGnaling Network Open Resource (SIGNOR)**. The individual nodes can refer to protein, complexes, small molecules, phenotypes or proteins annotated on SFARI, according to the legend. The main pathways in which SFARI genes converge are involved in different synaptic phenotypes, axon guidance, circadian rhythm and neurotransmitter release [10].*

It is also important to note that many of the ASD-risk genes are not exclusive to this disorder, but in many cases contribute to many other neurodevelopmental and psychiatric diseases (i.e. ADHD, intellectual disability, schizophrenia etc.). Although the risk genes are numerous and many of them are still to be identified, the two main biological processes where they converge are regulation of gene expression and neuronal communication [11]. Furthermore, many of these genes are involved in key cellular and neurodevelopmental processes, such as synapse formation, axonal growth and synaptic pruning. These cellular defects can thus alter the brain circuitry, and ultimately behavior [12]

Among the ASD-associated genes, *neurexins (NRXNs), neuroligins, shank3, tuberous sclerosis complex (tsc1/2), Fragile X Messenger Ribonucleoprotein 1 (fmr1) and Methyl-CpG Binding Protein 2 (mecp2)* emerge as regulators of synaptic function. When mutated, they can contribute to synaptopathies typical of the condition [11]. Both rare and recurrent variants are identified in the SHANK3 and NRX proteins, and both interact with neuroligin (NLGN) proteins, suggesting a role for the NLGN/NRXN signaling cascade in the biological mechanisms underlying cognition and social behavior [11].

2.2.Neuroligins and neurodevelopment

The family of neuroligins (NLGNs) comprises postsynaptic cell-adhesion proteins that stabilize synaptic contacts, mediate signaling and specify synaptic functions.

They are single-pass-type-I transmembrane proteins, and their functions are based on the interaction with their presynaptic partners, belonging to the family of neurexins (NRXNs).
In human there are five NLGN genes, four members common to mammals (*nlgn1, 2, 3* and *nlgn4*) and an additional homologue on the Y chromosome.

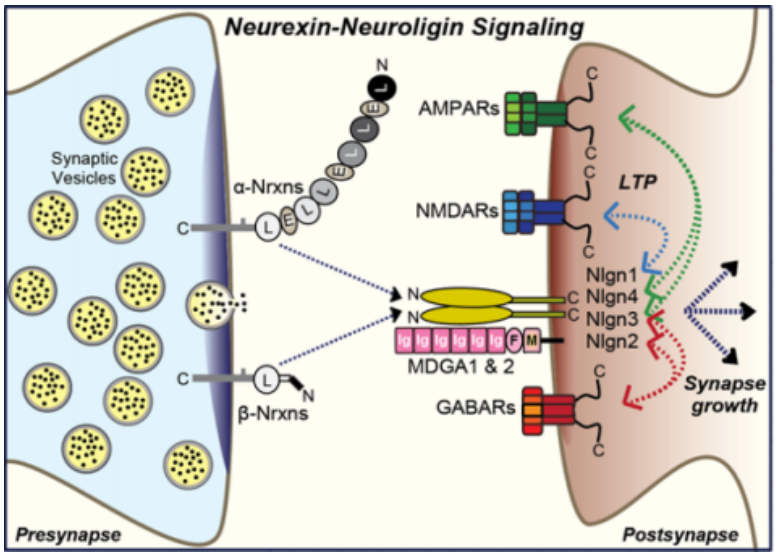

Figure 3*:*Overview of localization and binding partners neuroligins. *The 4 members of the postsynaptic protein family bind extracellularly to α- and β-neurexins through the N-terminal domain. Nlgn1 regulates NDMARs recruitment, AMPARs are recruited by Nlgn4 and Nlgn3, and GABARs are recruited by Nlgn3 and Nlgn2. (from www.med.stanford.edu).*

While the NLGN-NRXN complex stabilizes the pre- and post-synaptic compartments, NLGNs are crucial for proper synaptic function, as a *nlgn1/2/3* triple knock-out (KO) mice is lethal shortly after birth [11].
Several point mutations have been found to be associated with ASD, specifically on the extracellular domain.

2.2.1. Neuroligin-2

This thesis will take in examination the *nlgn2* gene, a high confidence ASD-risk gene[3]. NLGN2 possesses an extracellular domain that mediates binding to neurexins, its presynaptic partner, as well as neuroligin dimerization, in two primary interaction sites located on opposite sites. Neuroligins contain two splice sites, A and B, and exclusion of the latter promotes localization of the protein at GABAergic

[3] According to SFARI Gene database for the autism research community https://gene.sfari.org

synapses; that's the case of NLGN2 that is indeed exclusively present in this type of inhibitory synapses [3].On the other hand, GABAergic synapses display a greater localization of the short α isoform of neurexins, which include the splicing site 4 (SS4+), at the presynaptic level. NLGN2 dimerization can effectively cluster α-neurexin monomers at the presynaptic terminal, an event that acts as a signal that promotes the recruitment and alignment of presynaptic active zone components.

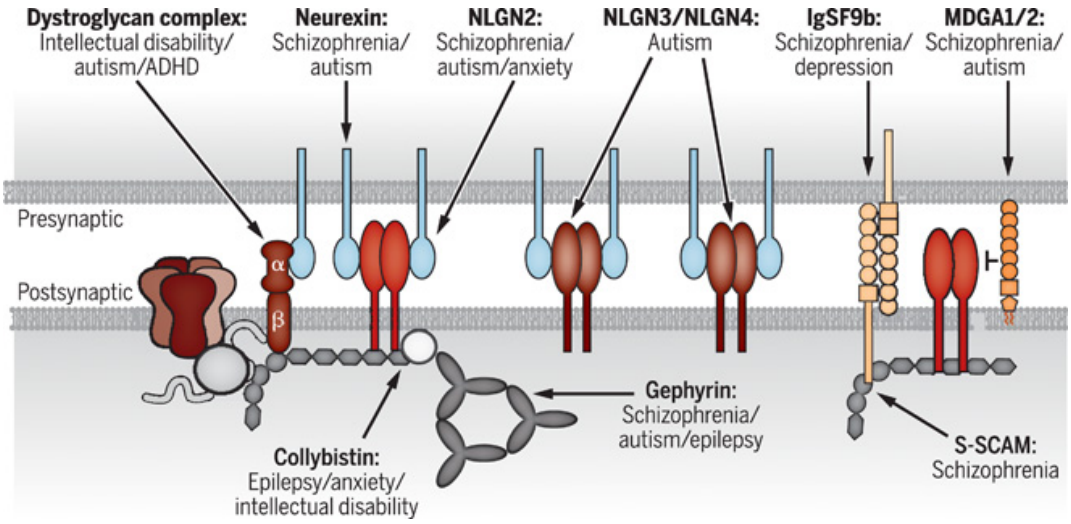

***Figure 4**: **Presynaptic and postsynaptic partners of Nlgn2 and pathologies in which are involved**. The main postsynaptic partners are collybistin and gephyrin, both involved in neurodevelopmental and psychiatric disorders. On the other side, the main presynaptic partner is neurexin, involved in autism too.[3].*

In this way, NLGN2 dimerization converts the transsynaptic binding event into a presynaptic assembly signal [3]. The dimerization interface is largely conserved among different neuroligins, thus not excluding the possibility of formation of heterodimers, even though NLGN2 forms primarily homodimers. At the postsynaptic compartment, NLGN2 short C-terminal domain mediates the interaction with the postsynaptic complex containing $GABA_A$ receptors, ligand-gated chloride channels that mediate fast inhibitory transmission.

NLGN2 interacts also with gephyrin, a scaffolding protein involved in the structural organization of inhibitory postsynaptic compartments [3].The recruitment of these two postsynaptic elements depends on the binding of NLGN2 to the collybistin (Cb) exchange factor. Standing to the actual model, NLGN2 clusters are formed in the postsynaptic compartment thanks to the early interaction with neurexins. Then, a tripartite complex comprising NLGN2, gephyrin and Cb is formed.

The binding of NLGN2 to a proline-rich motif of Cb results in an open conformation of the latter, with subsequent local assembly of a gephyrin scaffold and recruitment of $GABA_A$Rs. The main partners for the structural establishment and maintenance of inhibitory synapses comprise β-dystroglycan, which can bind

both NRXN and NLGN2 through the S-SCAM scaffolding protein, and the family of membrane-associated mucin domain-containing glycosylphosphatidylinositol anchor (MGDA) proteins, localized in the synaptic cleft. Recently, also SLIT And NTRK Like Family Member 3 (SLITRK3) was shown to interact with NLGN2 through its extracellular domain [3]. Studies in mice highlighted a reduced level of $GABA_A$Rs and gephyrin in *nlgn2* KO mutants, as well as a decrease in both amplitude and frequency of miniature inhibitory postsynaptic currents (mIPSCs) in most regions, suggesting a role for NLGN2 in functional connectivity and hence excitation/inhibition (E/I) balance in the neural network. In this context, mouse cortical neurons transfected with either neuroligin-2 short hairpin RNA (NL2shRNA) or neuroligin-2 microRNA (NLmiR) exhibit a reduced expression of KCC2, a K^+-Cl^- cotransporter fundamental for homeostasis of intracellular Cl^- [13]. KCC2 is a regulator of the GABA functional switch from excitatory to inhibitory during early development, a key developmental process typically complete around two weeks in mouse dissociated neuronal cultures. In human, the GABA switch is cell-type and region-specific, with some brain regions in which occurs earlier (e.g. sensory cortices) and some other in which occurs later (e.g. hippocampus). It also occurs earlier in females than males and likely within the first year of life [14]. Defects in these process have been associated also to ASD, and early study suggested identify it as potential therapeutic target [15]. KCC2 regulates this mechanism because capable of altering intracellular [Cl^-] and thus the direction of the ionic currents after $GABA_A$R opening by extruding chloride ions from the cell, thereby lowering intracellular [Cl^-]. Based on this, the opening of $GABA_A$R can induce either depolarization or hyperpolarization of the membrane, depending on whether the GABA E_{rev} potential is more negative (hyperpolarization) or positive (depolarization) compared to the membrane resting potential. Accordingly, over 90% of mouse 8 days in vitro (DIV) mouse NLmiR-transfected neurons exhibited large Ca^{2+} responses when treated with GABA, suggesting a disrupted GABA functional switch mechanism. Moreover, even in more than 80% of transfected 12 DIV neurons, when usually the functional switch should have been completed, large Ca^{2+} responses after GABA administration were observed. Moreover, NL2shRNA

transfected cortical neurons unexpectedly induced both a reduction of excitatory glutamatergic synaptic transmission and dendritic spine densities.

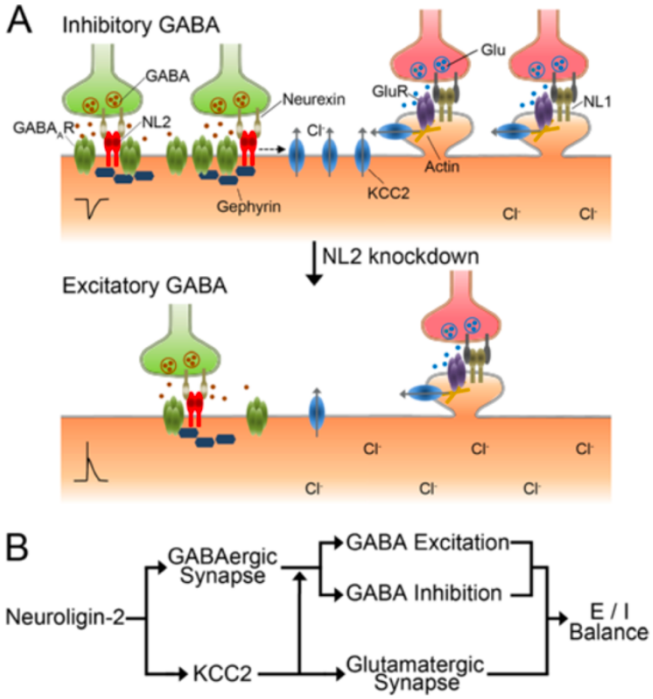

***Figure 5**: **Schematic model of proposed regulation mechanism of excitatory and inhibitory synapses mediated by neuroligin-2 through KCC2**. According to this model, NLGN2 knockdown interfere with the functional GABA switch occurring during early development, thus prolonging the excitatory phenotype of GABAergic synapses. It has also been proposed a role for NLGN2 in the indirect regulation of glutamatergic synapses through the KCC2 cotransporter. Both these alterations caused by NLGN2 defect finally alter the excitation/inhibition (E/I) balance, often altered in ASD [13].*

Homozygous mice models carrying the arginine to histidine (R215H) mutation on *nlgn2* gene showed also growth retardation compared to WT mice [3]. Focusing on the behavioral aspects, through open field (OF), elevated plus maze (EPM) and light-dark box (LDB) tests, it has been observed a general tendency of *nlgn2* KO mice to an increase of avoidance behaviors, a typical feature of ASD in human, while moderate overexpression of the protein resulted in anxiety-like phenotypes.
Although mutations on other members of the neuroligin family have been studied and show behavioral features of ASD in mice, such as increased repetitive behaviors for NLGN1, reduced vocalization and impaired social memory for NLGN3, and highly selective deficits in social interactions for NLGN4 (the member with the highest number of ASD-associated mutations) [11], NLGN2 mutants do not show such canonical behavioral phenotypes, but this does not necessarily imply any contribution to ASD. In fact, functional connectivity, neuronal morphology and brain circuitry alterations data are missing, thus preventing a linear and comprehensive understanding of the function and effects of the absence of the

protein, starting from the molecular, to the cellular, to the network and finally at behavioral level.

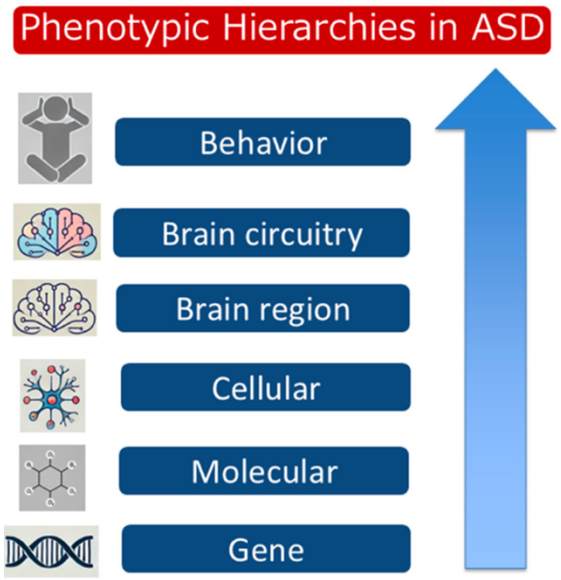

***Figure 6**: **Schematic representation of phenotypic impacts of ASD on different levels**. The scheme highlights the different levels at which ASD alterations can occur, starting from the molecular up to the behavioral level [12].*

This complete characterization of the protein, and the compartments and mechanisms at which the mutation causes defects, is of fundamental importance and a prerequisite also for the design of specific pharmacological treatments aiming at the restoration of correct brain function.
From the experimental point of view, a suitable in vivo model through which is possible to understand neurodevelopmental defects at these levels can be zebrafish, explained in the next chapters.

2.3. Zebrafish as a model to study neurodevelopmental disorders

Danio rerio, commonly named zebrafish, is a tropical ray-finned fish belonging to the order of Cypriniformes, native of southern Asia, specifically India, Pakistan, Bangladesh, Nepal and Bhutan. In natural environment, it can be found in stagnant clear water typical of ponds, canals, oxbow lakes and streams. Their optimal pH is slightly basic, and optimal temperature is ~28°C.Zebrafish gets his name from the typical blue stripes on its body side. Its characterized also by a fusiform shape and specimens can be distinguished by the more pronounced belly and paler pigment of the females, opposed to the slenderer shape and brighter color of the males. Even though zebrafish takes its name from this typical striping, several strains and mutations causing differences in pigmentation are known and commonly used for research purposes, such as the albino phenotypes given by the *nacre* (*mitfa* $^{-/-}$) and

casper (*mitfa* $^{-/-}$, *mpv17* $^{-/-}$) strains. Lifespan in captivity is ~3 years and sexual determination and maturation covers the first three months of development.
Focusing on embryogenesis, development from zygote to early larva lasts 3 days and the juvenile phase starts at ~7 days-post-fertilization (dpf).

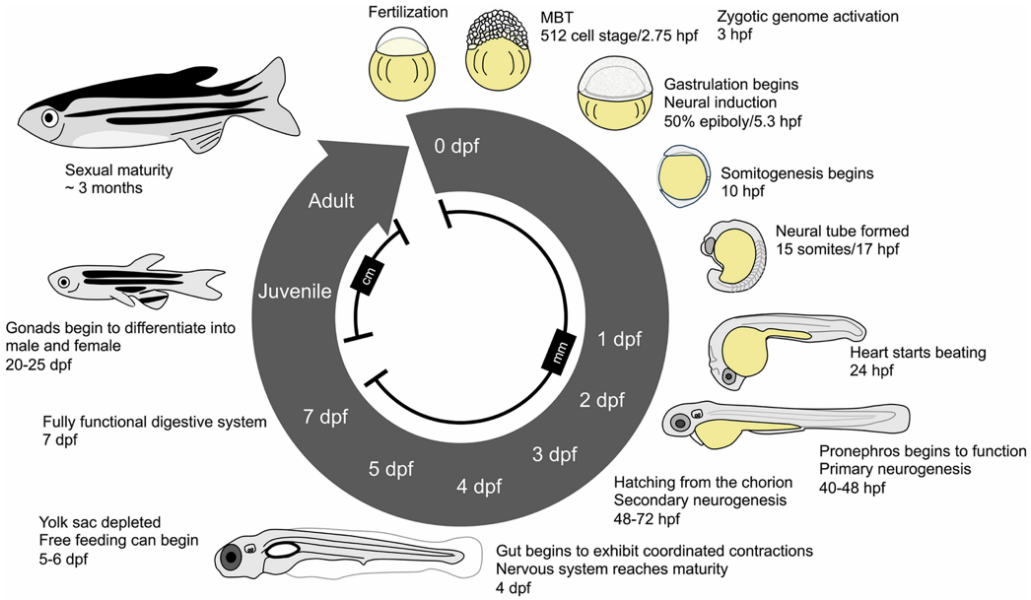

***Figure** 7: **Zebrafish embryogenesis and development**. The scheme highlights the main developmental stages such as MBT, gastrulation and neural tube formation and heart beating occurring within 24 hpf. Nervous system reaches maturation at 4 dpf, and at 7 dpf the digestive system is fully functional. In the juvenile phase the gonads start differentiation ~ 20 dpf and at 3 mpf the fish is sexually mature (Bedell V.M. et al., 2025)*

A fertilized egg starts cleaving at 0.75-2.25 hours-post-fertilization (hpf), with Mid-Blastula Transition (MBT) occurring at 2.75 hpf. MBT is characterized by slowing of the cell cycle with emergence of G1 and G2 phases, asynchronous cell division and together with zygotic genome activation, overpassing the dependance from maternal mRNA and protein products. At ~ 5.3 hpf gastrulation begins. This phase is characterized by coordinated cell movements that reorganize the embryo in three distinct germ layers, namely ectoderm, mesoderm and endoderm, and establishes the body axes required for subsequent organogenesis. At 10 hpf, paraxial mesoderm is regularly segmented into somites, structures that will lately give rise to vertebral column, skeletal muscles and dermis, in a process named somitogenesis. At 17 hpf, the neural plate undergoes bending to close and form the neural tube. Zebrafish develops a mature nervous system at 4 dpf [16]. Zebrafish is a consolidated model organism for developmental biology, toxicology and cancer research, and emerged to be useful also for neuroscience and neurodevelopmental studies. The reasons for this are several, but we can point out the major ones. Firstly, genome-wide studies have revealed that approximately 70% of human genes have at least one zebrafish

orthologue, with the largest sequenced gene set available for any vertebrate so far, comprising more than 26.000 protein-coding genes [17]. Secondly, the rapid life cycle, with sexual maturity reached within approximately three months, together with fast embryonic development, represents a significant advantage in terms of experimental time. Thirdly, zebrafish is a model prone to genetic manipulation, with two main techniques established for this purpose.

Morpholino oligonucleotides (MOs) are antisense DNA analogs usually 22-25 nucleotide (nt) in length that are widely used for loss-of-function studies [18]. They are engineered to hybridize mRNAs/pre-mRNAs at the translation initiation or splicing/acceptor/donor sites, causing knockdown of the gene of interest when injected into fertilized eggs [19]. In the most recent years, also CRISPR-Cas9 based genome engineering has spread widely. This endonuclease can induce double strand breaks (DSBs) thanks to a single guide (sgRNA) RNA molecule engineered to target genomic sites of interests. The sgRNA is composed of a CRISPR RNA (crRNA) molecule, that contains the target sequence, and a trans-activating crRNA (tracrRNA) molecule connected through a linker loop. The crRNA/tracrRNA hybrid guides the Cas9 endonuclease to the genomic site of interest, but in order to induce DSBs, CRISPR requires a protospacer adjacent motif (PAM) located next to the crRNA target region. Precise DSBs then promote DNA repair mechanisms that ultimately result in the so-called non-homologous end joining (NHEJ) event, causing a shift in the open reading frame (ORF) thus adding a premature stop codon to the mRNA, with gene silencing as result. The mutant model object of this study was also generated via CRISPR-Cas9 gene silencing. In the field of neuroscience and in the study of neurodevelopmental disorders, zebrafish emerged as pivotal model for imaging, given its external and fast development, the translucence typical of the larval stage that allows direct observation of developing brain regions, a feature that can be further optimized using the pigmentation mutants mentioned before (i.e. *nacre* and *casper* strains), that offers optimal conditions for *in vivo* imaging. Moreover, there are functional similarities to the mammal brain, as well as behavioral parallels with humans, sensitivity to neurotropic drugs and the possibility of conducting high-throughput behavioral analyses at early developmental stages.

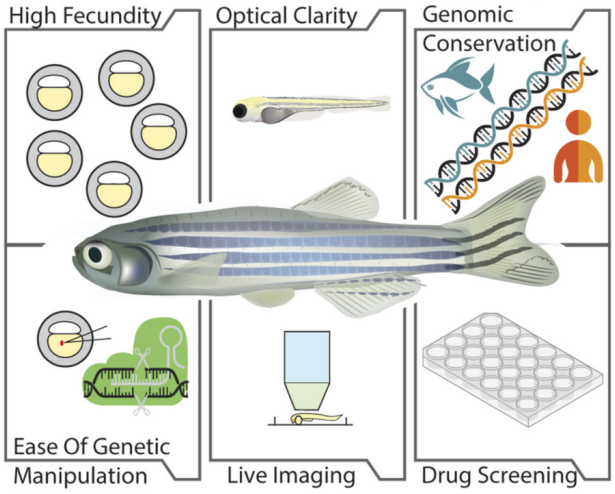

***Figure 8**:**Advantages of zebrafish as model organism**. Among the features that make it a suitable model, the high fecundity, ease of genetic manipulation through Mos and CRISPR-Cas9, possibility of high-throughput drug screening, genomic conservation compared to human (70% of human genes possess one or more zebrafish hortologs), and optical clarity that allows to perform live imaging with confocal or two-photon microscopy. [20]*

For behavioral studies, several tools became available in these last years. For example, Noldus DanioVision is a zebrafish larvae observation chamber where live tracking and data collection under different types of stimuli (i.e. luminance changes or vibrations) allows unbiased quantification of motion parameters in behaving larvae. Other than this, a consolidated system for the study of sensory information processing and related motor outputs, and its alterations in ASD, is the visuomotor one. For all the reasons mentioned above, this was the model chosen for the study of NLGN2.

2.4.Neuroligin-2 in zebrafish. Generation of mutants

Zebrafish possesses 7 *nlgn* genes, 3 of which are duplicates of mammalian *nlgn2, 3* and *4* genes, while *nlgn1* is found as a single copy. Neuroligin-2 indeed has 2 paralogs, namely *nlg2a* and *nlg2b*, result of a genomic duplication event. In zebrafish, both paralogs are expressed in the nervous system, gills, gonads, heart and swim bladder. RT-PCR showed *nlg2na* expression starting from ~16 hpf and *nlgn2b* from ~11 hpf, while in situ hybridization (ISH) detected expression of the transcripts in the dorsal-rostral and ventral-rostral telencephalon at 24hpf, while adult brain ISH highlighted broad expression in the periventricular zone of the optic tectum, pretectal nucleus, thalamus and hypothalamus [21].The *nlgn2a* and *nlgn2b* mutants were previously generated in the laboratory using CRISPR-Cas9.
sgRNAs specific for each paralog were designed to induce the DNA cut within the first exon of the sequences, resulting in NHEJ and premature stop codon.

1-cell stage embryo microinjections were performed, followed by PCR and sequencing to verify the efficacy of the gene editing.

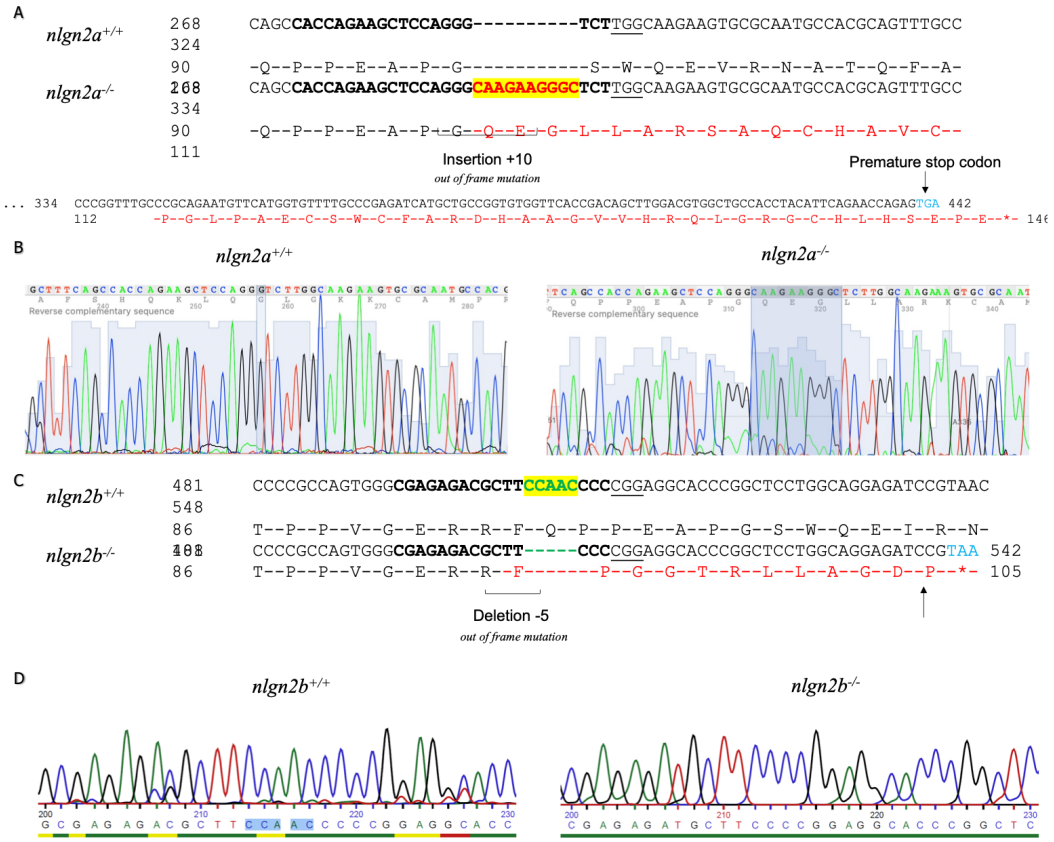

***Figure 9**: **Characterization of the mutation in nlgn2a$^{-/-}$ and nlgn2b$^{-/-}$ fish**. (**A**) nlg2na$^{+/+}$ and nlgn2a$^{-/-}$ cDNA (top) and aminoacidic (down) sequences. The genomic insertion is highlighted in yellow. (**B**) Representative sequence chromatographs for nlgn2a$^{+/+}$ and nlgn2a$^{-/-}$. On the right, the inserted sequence is highlighted. (**C** and **D**) Similar sequence alignments and chromatographs for the nlgn2b mutation, characterized by an insertion of 5 nucleotides.*

The *nlgn2a* mutant line harbors an insertion of 10 nucleotides in exon 3, while the *nlgn2b* mutant line a deletion of 5 nucleotides in exon 4, both leading to a truncated protein product.

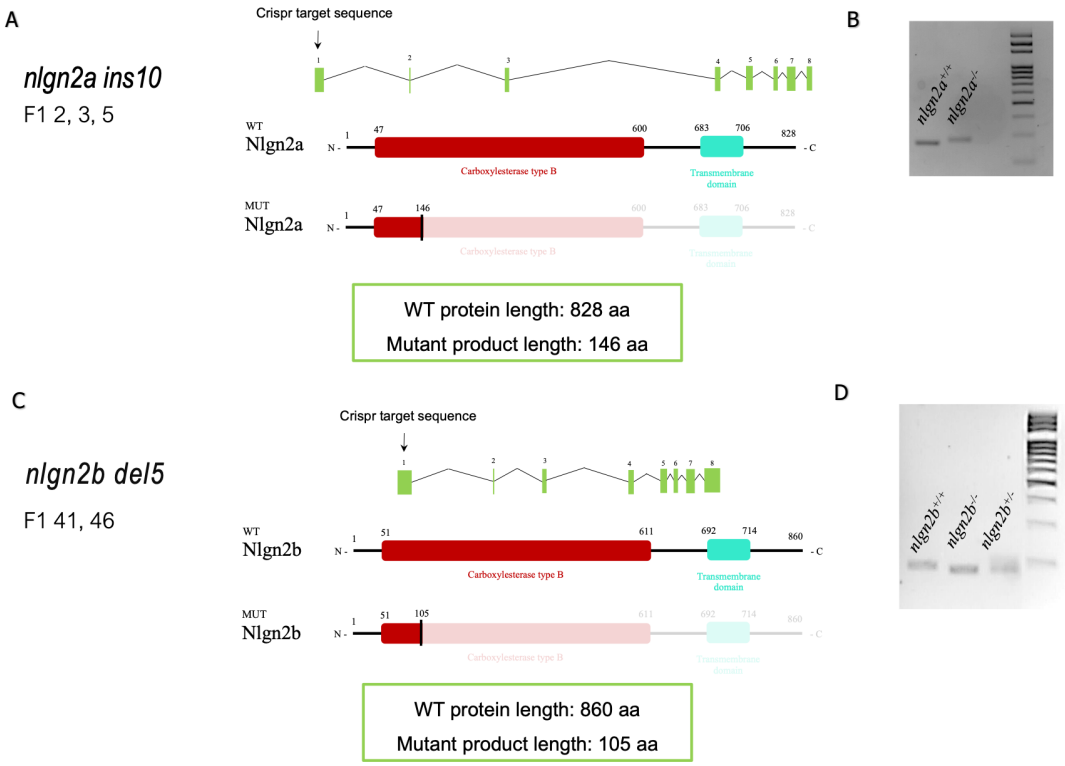

***Figure 10**: **Overview of mutagenesis using CRISPR-Cas9 for nlgn2a and nlgn2b**. (A) Overview of exons and Crispr target (top) and WT and mutant protein structure. nlgn2a mutants have a portein length of 146 aminoacids. (B) Representative PCR products of tail fin clips obtained by adults (3 months old) WT and nlgn2a$^{-/-}$ fish. (C and D) Similar schematics and representative gel images for nlgn2b mutants.*

2.5. The zebrafish visual system to investigate neural basis of behavior

To link behavioral patterns with the underlying neuronal circuitry, zebrafish and its visual system emerged as useful model, thanks to the possibility of simultaneous imaging of live brain activity and motor responses together. This system can be indicatively grouped in three components: the eye, specifically the retina, the retinofugal projections originated in it, and the retinorecipient visual centers in the brain [22], with the optic tectum (OT) being the largest one. Initially, the signal resulting from the phototransduction of light from the outer retinal layer of rod and four types of cone photoreceptors is transmitted to an internal layer of bipolar cells and then to retinal ganglion cells (RGCs), the output cells of the retina. Visual information is split from the beginning into features such as luminance, transience, contrast, color, size, speed and direction of the visual stimulus by the amacrine and bipolar cells, resulting in RGCs spiking activity [23]. RGCs have been subdivided into 14 morphological classes based on dendritic stratification patterns in the inner plexiform layer (IPL) of the retina, a number that surpasses 50 when considering the different axonal projection patterns observed [24].

RGCs projections terminate in 10 distinct arborization fields (AFs), localized in different retinorecipient regions of the brain, namely hypothalamus (AF1 and AF2), prethalamus and thalamus (AF3 and AF4), pretectum (AF5-9) and tectum (AF10). ~97% of RGCs project to the tectum, with half of them exclusively terminating in it [24].

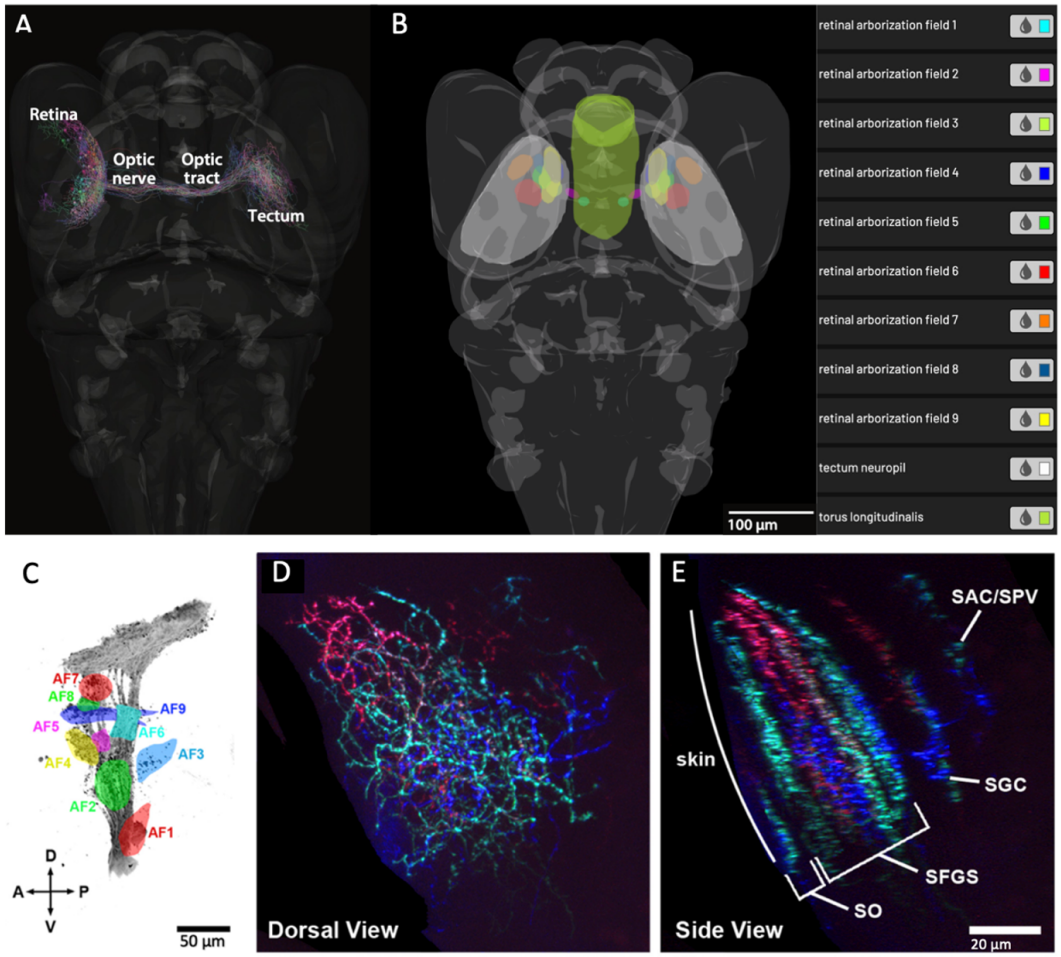

***Figure 11**: **Anatomical organization and components of the zebrafish visual system**. (A) Retinal Ganglion Cells (RGCs) localization and projections along to the tectum along the optic tract, visualized in the Max Planck zebrafish brain Atlas [23]. (**B**) Localization of the 10 retinal Arborization Fields (AFs) and Torus longitudinalis (TL), a region establishing bilateral connections with the tectum, the largest AF. Visualized in the Max Planck zebrafish brain Atlas. (**C**) Schematized lateral view of the optic tract and the AFs [24]. (**D-E**) Dorsal and lateral views optic tectum lamination of a 7dpf transgenic larva obtained with multicolor Brainbow labeling [25].*

This anatomical classification, and the spatial division of retinorecipient regions, underlies a functional segregation of retinal outputs. In parallel, RGCs can be functionally classified on their responses to changes in luminance, with distinct populations selectively activated by increases (ON), decreases (OFF), or both increases and decreases (ON-OFF) in light intensity. Furthermore, also the AFs are functionally subdivided; for example, AF9 dorsal region is mainly innervated by RGCs with dendrites stratified in the ON sublayer of the IPL, while the ventral is equally innervated by ON and OFF-responsive axon terminals [24].

In general, the visual channels resulting from different combinations of RGCs morphological types, transmit ethologically important information to premotor and motor circuits, resulting in behavior.

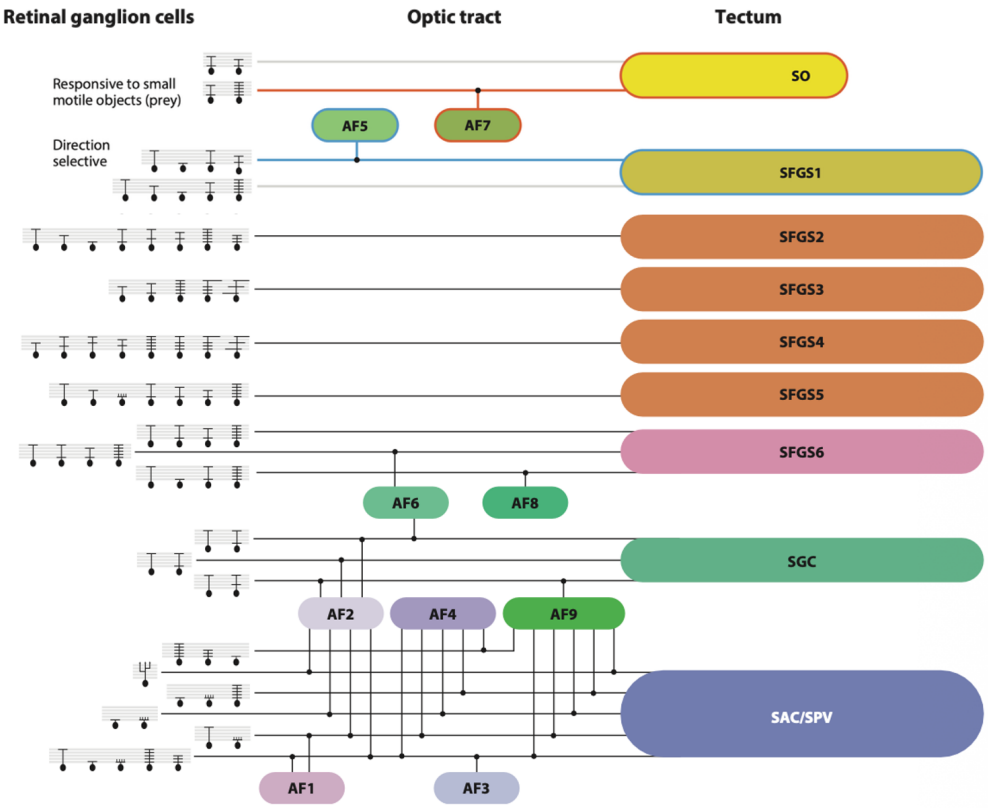

***Figure 12**: **Combination of dendritic and axonal projection patterns and targets establish roughly 20 visual channels**. For example, two distinct types of RGCs projecting to AF7 and SO are involved in hunting behavior, while four RGC types projecting to AF5 and SFGS1 are direction selective (modified from Baier H. & Scott E., 2024).*

The OT is a bilateral region localized in the dorsal midbrain, homologue to the mammalian superior colliculus (SC) and the largest visual center of the developing zebrafish brain.

Beside the main inputs coming from the retina, the OT establishes bilateral connections with other regions, such as pretectum, dorsal thalamus and tegmentum, nucleus isthmi, reticular formation contralateral tectum, and torus longitudinalis (TL), a relay center of telencephalic inputs.

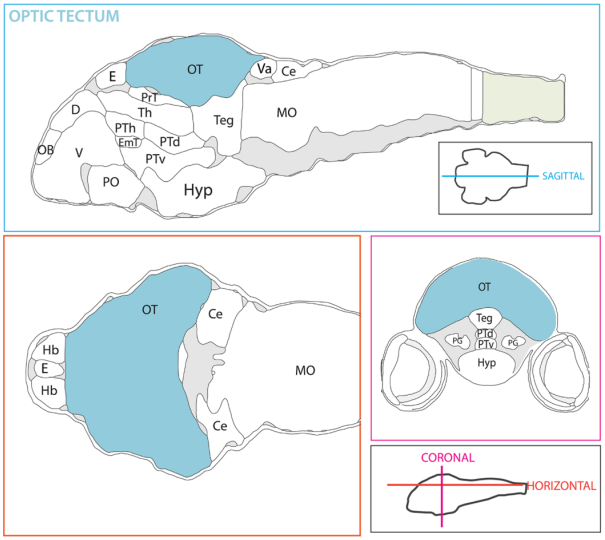

***Figure 13**:**The optic tectum in zebrafish 3dpf brain**. Based on anatomical segmentation from Müller T. et al., 2012. Schematic image from www.zebrafishucl.org.*

Structurally, the OT can be divided in three major laminated structures: the superficial, central and periventricular (SPV) zones. The superficial zone consists of the stratum marginale (SM) and stratum opticum (SO), the central zone consists of stratum fibrosus and griseum superficiale (SFGS), stratum griseum centrale (SGC) and stratum album centrale (SAC). The majority of tectal cell bodies reside in the deep SPV layer.

Lamination is crucial for accurate sensory information processing and motor outputs. It achieves this by spatially segregating different synaptic functions, separating input, processing, and output layers.

Furthermore, axonal projections are organized in such a way that preserves the spatial relationship between points in the retina, creating an ordered spatial map of the visual field, in a process named retinotopy.

The OT has been demonstrated to be involved in behavioral patterns such as prey detection and capture, predator avoidance, and visually evoked escape responses [26]. In this context, one strong behavioral response has emerged as useful paradigm for the study of neuronal circuitry, the optomotor response (OMR).

The OMR is a locomotor behavior where the fish swims in the direction of the perceived optic flow to maintain its position in the natural environment.

This paradigm can be easily elicited and exploited in an experimental setup; in fact, the fish head can be immobilized in agar, the tail can be left free to move and a visual grating can be presented.

In such manner, it is possible to simultaneously induce OMR, track the motor output and image at high resolution the concurrent neuronal activity in the brain.

2.6. Anatomical, behavioral characterization and high-resolution imaging for a multilevel approach on ASD study

On the basis of what introduced in the previous chapters, zebrafish emerges as one of the most suitable organisms for ASD modeling and characterization.

Firstly, the ease of manipulability and the fast developmental time allows researchers to obtain functional, morphological and anatomical data at different developmental time points and with large number of individuals. This is extremely useful when considering the gross anatomical alterations (i.e. head and brain morphology) as indicative of delayed neurodevelopment [27].

For this purpose, several parameters can be considered, such as total body length, head width and height, providing a first overview of the general anatomical alterations, if present, of the mutants.

Secondly, it's possible to conduct behavioral analyses and verify whether these are resembling known ASD patterns. As anticipated before, several tools such as Danio Vision and a specific setup meant to elicit OMR can be employed.

Finally, to study the cellular and functional aspects several techniques and instruments became available in the latest years.

In fact, a wide range of transgenic reporter lines allows specific targeting of neuronal populations depending on region, morphology or neurotransmitter phenotype.

For example, *gad1b* encodes for an enzyme that catalyzes the decarboxylation of L-glutamic acid into gamma-aminobutyric acid (GABA), the main inhibitory neurotransmitter, and accordingly is expressed in GABAergic neurons. This differential expression can be exploited to mark with a fluorescent label the GABAergic neuronal population in the brain, allowing researchers to conduct analysis restricted to the inhibitory GABAergic portion of the network.

On the other hand, for functional studies, genetically encoded calcium (GECIs) and voltage (GEVIs) indicators can fill the gap between canonical electrophysiological measurements and low-invasiveness *in vivo* imaging.

Electrophysiology, even if characterized by high temporal resolution capable of capturing all the fluctuations of the membrane potential, underpinning the different ionic currents resulting in the phases of an action potential (AP), is usually an invasive technique which requires either fresh and thin brain sections, or surgical intervention to attach the electrode to the behaving animal.

Conversely, non-invasive techniques such as electroencephalography (EEG) and functional magnetic resonance imaging (fMRI) allow recording of whole-brain neural activity effectively discriminating different areas but lack single-cell and precise temporal resolution.

Among the most common GECI employed for non-invasive high resolution functional imaging there is GCaMP, a calcium sensor consisting of a circularly permuted green fluorescent protein (cpGFP), calmodulin (CaM) for endogenous calcium binding, and M13 CaM-interacting peptide. Upon calcium binding to calmodulin, the major conformational changes in the Cam/M13 complex result in a stabilization of cpGFP, sharply increasing its fluorescence. In such way, it is possible to record calcium transient resulting from neuronal activity with a fluorescent signal as readout.

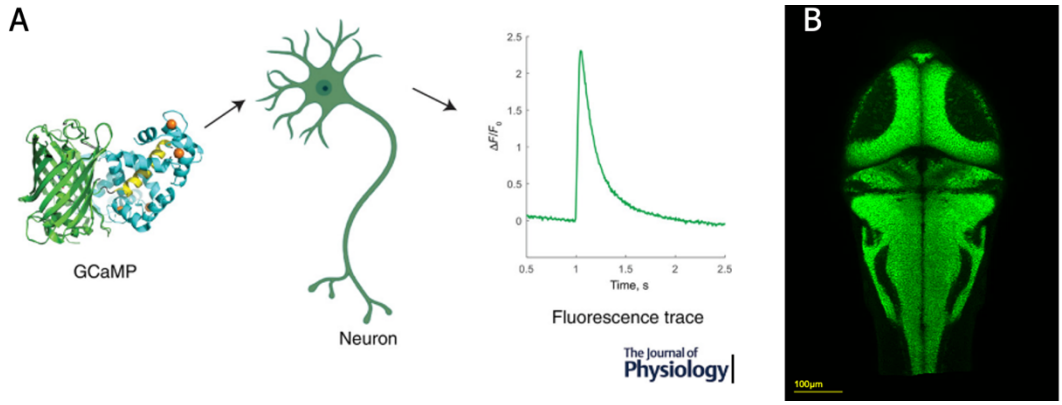

***Figure 14**: **Use of GCaMP for neuronal activity recordings** (**A**) Schematic image of GCaMP structure and example of fluorescence trace underlying neuronal activity. The fluorescent trace is characterized by a rapid increase in fluorescence followed by a slow decay [28]. (**B**) Whole-brain confocal image of Tg(elavl3:Hsa.H2B-GCaMP6s) 6 dpf fish visualized in the Max Planck zebrafish brain Atlas (www.mapzebrain.org).*

In this sense, GECIs and GEVIs are lying between electrophysiology and *in vivo* imaging, characterized by suitable temporal and spatial resolution (even though lower compared to electrophysiology) and low invasiveness when combined with specific imaging techniques.

Under the technical point of view, two-photon microscopy emerged as an important instrument for high-resolution functional imaging also coupled with behavior.

This technique is based on the near-simultaneous absorption of two low-energy photons to excite a fluorophore. Because excitation is confined to the focal volume, this technique enables deep tissue imaging with reduced photodamage compared to conventional confocal microscopy [29].

For the investigation of cellular morphologies and synaptic structures, confocal and electron microscopy (EM) are the most suitable techniques.

With confocal microscopy is possible to obtain volumetric image stacks that allow high-resolution acquisition of both large brain areas and single neuron axonal and dendritic branches and spines. Furthermore, is a type of microscopy compatible with fluorescent reporters and transgenic lines that enable cell-type specific

anatomical characterization and, since imaging is non-destructive, allows observation of the same individual at multiple developmental stages, an important factor when considering key aspects of ASD, such as developmental delay.

Finally, electron microscopy (EM) reaches the highest resolution level achievable, and detailed cellular compartments and structures, such as synaptic clefts, presynaptic vesicles, active zones and postsynaptic densities can be analyzed. With this level of resolution, it is possible to resolve the nanometer-scale structures of the synapse which hold the base of synaptopathies, common in ASD.

3. AIM OF THE STUDY

Autism spectrum disorder is a neurodevelopmental condition caused by defects across multiple biological levels, from nanometer-scale structural alterations in synapses, to core morphological neuronal defects, to circuit function and behavior. Among genes contributing to the condition, neuroligins emerge as important regulators of synaptic structure and maintenance.

Particularly, neuroligin-2 is a structural central organizer of inhibitory synapses involved also in excitation inhibition (E/I) balance, a dynamic equilibrium between excitatory and inhibitory signaling often disrupted in ASD.

Even though this gene is considered a high-confidence risk for ASD and the other members of the family have been studied, a comprehensive *in vivo* characterization of its function during early development is still missing.

For these reasons, this thesis' aim is to lay the foundations of an anatomical, functional and behavioral characterization of 2 zebrafish mutant lines, generated through CRISPR/Cas9, *nlgn2a* and *nlgn2b*.

Particularly, this work aims to:

1) Verify the transcriptional levels of the genes mutated to confirm the successful generation of the mutants and verify the presence of possible compensatory mechanisms.
2) Conduct gross anatomical morphological and survival analysis on *nlgn2a*$^{-/-}$ and *nlgn2b*$^{-/-}$ larvae at different developmental time points to determine whether loss of the protein contributes to structural abnormalities and/or alters the survival rate.
3) Conduct a first behavioral characterization of *nlgn2a*$^{-/-}$ and *nlgn2b*$^{-/-}$ mutants to verify whether locomotor activity and photoresponse are affected.
4) Validate a transgenic line meant for cellular characterization of a tectal pyramidal neurons (PyrNs) population labeled by the *id2b* transgene and conduct single neuron morphological analyses on PyrNs to verify whether *nlgn2a*$^{-/-}$ mutants exhibit structural defects or altered dendritic spine density, an unexpected result observed in a mice model for NLGN2.
5) Analyze the synaptic ultrastructure through electron microscopy to observe alterations in the transmission compartment.
6) Generate transgenic lines for imaging of excitatory and inhibitory synapses through FingR plasmids for postsynaptic density 95 (PSD95) and gephyrin (GPHN) proteins.
7) Obtain single-cell transcriptomics data to assess the cellular components that are affected and differentially regulated in *nlgn2* mutants.

By combining molecular, anatomical, imaging and behavioral analyses, this thesis aims to amplify the knowledge of the function and consequences of the mutation of neuroligin-2 *in vivo*, and to verify whether these mutants are suitable for future investigation on ASD research.

4. MATERIALS AND METHODS

4.1. Zebrafish larvae and adults' maintenance and husbandry

All experimental procedures regarding zebrafish were conducted following the Italian and European legislation (Directive 2010/63/EU) on the protection of animals used for scientific purposes.
Adult zebrafish are raised in a temperature-controlled environment (28°C) on a 12h light and 12h dark period, stimulating their natural circadian rhythm.
Adults are kept in specific tanks of different dimensions based on the age, size and number of individuals. The tanks are inserted in dedicated water recirculation systems, where correct oxygenation and cleanliness is assured by both mechanical and UV-based water cleaning systems. The tanks are also manually cleaned at least once per week by syphoning.
Juveniles and adults are fed three times a day by a mix of dry (AZ300) and live food (*Artemia salina*), respectively once a day in the morning, and twice in the morning and in the afternoon.
Administration of live food is important and considered as an enrichment because it stimulates an important behavior such as the predatory one, which would struggle to emerge with dry food feeding alone.
Once collected, zebrafish eggs and embryos are kept in a solution named "Fish Water", composed of nitrates-poor water and a composition of salts which, for a total volume of 15 liters, is the following:

Component	**Amount**
$CaSO_4$	23.5 g
$NaHCO_3$	3 g
Instant Ocean®	15 g

***Table 1**: Composition of Fish Water for zebrafish*

This solution is added also with methylene blue, a compound used for the prevention of fungal infections.
Zebrafish sex determination is primarily genetic, but also environmental factors such as the temperature can modulate sex determination [30]. Individuals are considered sexually mature when they reach ~12 weeks age (3 mpf).
To obtain eggs either for future breeding or experimental procedures, a specific protocol is followed.

The day prior to the mating, males and female adults are put in a dedicated breeding tank with a 1L capacity and kept separated by a divisor until the following morning, when it is removed.
Zebrafish mating behavior is characterized by the male following the female and swimming next to it to facilitate eggs fertilization. Once expelled and fertilized, eggs land on the bottom of the tank, separated by the adults thanks to a specific divider to prevent egg eating by the adults.
Eggs are collected with a strainer and kept in a 25 ml petri dish added with fish water. Unfertilized or rotten eggs are removed by visual inspection under a stereomicroscope.
Larvae begin to be fed with dry food starting from 6 dpf, with *Artemia salina* from ~10 dpf. At 3 weeks age, they are transferred to the adult tanks and fed accordingly.
For experimental procedures as well for euthanasia, fish are treated with Tricaine 1x (Sigma-Aldrich®), an anesthetic agent blocking voltage-gated sodium channels, thus preventing movement. [31].
On adults, 0.16 mg/mL tricaine is used for anesthesia, and 0.3 mg/mL for euthanasia.

4.2. Zebrafish mutant and reporter lines

The Tg(id2b:Gal4-VP16) line has been previously generated by BAC recombineering [32] and characterized [33].
The Id2 (inhibitor of DNA binding) protein family in zebrafish acts as transcriptional repressor and in zebrafish there are two isoforms, *id2a* and *id2b*. The *id2b* isoform is expressed in cardiovascular system, liver, notochord, pronephric duct and nervous system (*www.zfin.org*). In the CNS, it is expressed in the optic tectum, retina and hindbrain [32].
Briefly, the *id2b* BAC clone contained upstream and downstream Transcription Start Site (TSS) sequences with insertion of transcription regulatory elements.
Arabinose-induced homologous recombination was performed, according to the Bussmann and Schulte-Merker protocol [32], and a cardiac muscle cell marker was inserted as integration control for the Gal4VP16 construct, the so called "*bleeding heart*" (BH) (*cmlc2:mCherry*).
The F_1 offspring was screened under a fluorescent microscope to identify germline-transmitting founders, highlighting a founder rate of 3.6% for the id2b-Gal4VP16 reporter line.
The *nlgn2a* $^{-/-}$ and *nlgn2b* $^{-/-}$ mutant lines had been previously generated via Crispr-Cas9 mediated knockout (Introduction).

Both WT, *nlgn2a*$^{+/-}$ and *nlgn2a*$^{-/-}$ Tg(id2b:Gal4-VP16, UAS: epNTR-mCherry) lines used for confocal imaging were also *mitfa*$^{-/-}$ (*nacre*) mutants. The latter mutation results in an albino phenotype, which allows optimal confocal imaging acquisition without the need of chemical depigmentation with phenylthiourea (PTU) or hydrogen peroxide (H_2O_2).
All larvae used for neuronal morphology analyses were imaged on the confocal microscope at 8dpf, the developmental window in which fluorescence intensity signal was optimal [34].
For survival and anatomical analysis and for qPCR, mutants belonged to the Tüebingen (Tüe) WT pigmented strain.

4.3. Gene expression analyses

4.3.1. RNA extraction and purification

To obtain RNA samples from 5-7dpf zebrafish larvae, or adult brains, a specific RNA extraction kit was used (Qiagen Mini RNeasy kit).
Briefly, larvae or tissues were put in 600 µl buffer RLT added with 20 µl of 2 M dithiothreitol (DTT), a thiol-based reducing agent able to inactivate RNases by breaking their disulfide bonds, thus preventing RNA degradation.
Samples were then homogenized with the TissueLyser© system (Qiagen) at 300 Hz for 3 minutes.
After this step, the standard protocol for RNA extraction was followed[4]. Lysates were centrifuged, the supernatant was collected and added with ethanol. After a first round of filtration, in-column DNase digestion was performed followed by three washes with specific buffers. Finally, samples were eluted in RNase-free water.
Finally, RNA concentrations were measured with NanoDrop One spectrophotometer. For each sample, 1 µl of purified plasmid absorbance was measured by the instrument with RNase-free water as blank.

4.3.2. RNA retro-transcription

The purified and quantified RNA was then retrotranscribed into cDNA using the Applied Biosystem High-Capacity cDNA reverse transcription kit. 1 µg of RNA was diluted in RNase-free water to a final volume of 10 µl, which was then added with 10 µl of reverse transcription (RT) master mix, composed as follows:

[4] Detailed description of the kit's reagents and buffer composition can be found at www.qiagen.com.

Component	Volume (µl)
10X RT Buffer	2.0
25X dNTP Mix (100 mM)	0.8
10X Random Primers	2.0
MultiScribe^{TM} Reverse Transcriptase	1.0
RNase Inhibitor	1.0
Nuclease-free H_2O	3.2

Table 2: Composition of Reverse Transcription master mix.

Samples were then sealed, briefly centrifuged to spin down the whole content and incubated in a thermocycler to perform reverse transcription, according to the parameters below:

Step	Temperature	Time
Primer annealing	25°C	10 min
cDNA synthesis	37°C	120 min
Reaction termination	85°C	5 min
Hold	4°C	∞l

Table 3: Termocycler parameters for reverse transcription.

4.3.3. RT-qPCR

With the cDNA samples obtained with the reverse transcription assay, Real-Time quantitative Polymerase Chain Reaction (RT-qPCR) was performed on WT, *nlgn2a*$^{-/-}$ and *nlgn2b*$^{-/-}$ samples.

RT-qPCR is a widely used gene expression technique capable of quantifying gene expression in a fast, precise and reliable way.

RT-qPCR principle relies on the recording fluorescence emission given by a DNA-binding fluorescent probe after each PCR cycle.

One fundamental parameter for quantification is the cycle threshold (Ct) value, which represents the number of cycles required for surpassing of a defined fluorescence threshold value. Low Ct values indicate high cDNA and so high gene expression, while high Ct values low gene expression.

Normalization for fluorescence intensity is performed by computing the ΔCT value, given by the difference between Ct value of the target gene and Ct of a housekeeping gene, in our case *eef1l1α*.

After this normalization step, the ΔΔCT value is computed, indicating the difference of ΔCT between the sample of interest and the biological control, in our case WT samples.

The primers used for amplification of genes of interest were designed to amplify the sequences between exon 3 for *nlgn2a* and exon 4 for *nlgn2b*, found downstream the premature stop codon caused by NHEJ. The primers were the following:

Primer name	**Sequence**
nlgn2a_F_ex3	5'-GGGAACGTCATTGTAGTCACC–3'
nlgn2a_R_ex3	5'-GCCCCAGAGCCAAAGATA-3'
nlgn2b_F_ex4	5'-TTGCGGCCTATGGAAATGTG-3'
nlgn2b_R_ex4	5'-CAGGGCTTGAATCTGGTCCA-3'
eef11α_F	5'-TGCAGAGATGGGAAAGGGT-3'
eef11α_R	5'-GCTGGTCTCAAACTTCCACA-3'

Table 4: 5'-3' sequence of primers for RT-qPCR.

The RT-qPCR mix for each sample was composed as follows:

Component	**Volume (µl)**
5X HOT FIREPol Evagreen qPCR Supermix	2
Forward primer (10 µM)	0.25
Reverse primer (10 µM)	0.25
cDNA	2
H_2O	5.5

Table 5: Composition of RT-qPCR mix.

The RT-qPCR parameters were the following:

Step	**Temperature**	**Time**	**Number of cycles**
Initial denaturation	95°C	10 min	1
Denaturation	95°C	15 sec	45
Annealing	60°C	25 sec	45
Extension	72°C	25 sec	45
Final extension	75°C	10 min	1

Table 6: RT-qPCR parameters' temperature and duration

After the completion of the qPCR cycles, Ct, ΔCT and ΔΔCT values were computed and relative expression, derived from the latter value, were plotted and statistic were computed using GraphPad Prism.

4.4. Developmental, morphological and functional assays

4.4.1. Survival analysis

Survival analyses were conducted on 3 independent biological replicates of WT, *nlgn2a*$^{-/-}$ and *nlgn2b*$^{-/-}$ fish containing the GCaMP6^{+} calcium indicator, with a total number of 60 fish per condition. For each replica, eggs were collected and embryos were raised in separated Petri dish added with 25 mL of Fish Water.
At 7 dpf, 20 larvae from each plate were inserted in breeding tanks and set as reference (100%) for the subsequent analyses.
At 14, 21 and 28 dpf time points, the alive individuals were counted, and relative survival rate was annotated.
Finally, survival Kaplan-Meier curves were generated using GraphPad Prism and Log-Rank (Mantel-Cox) test was performed.

4.4.2. Anatomical analysis

To verify whether NLGN2 mutations could affect the gross anatomical organization of zebrafish during early development, several anatomical parameters were analyzed at 7, 14 and 21 dpf timepoints, for 4 independent biological replicates of 6-10 WT, *nlgn2a*$^{-/-}$ and *nlgn2b*$^{-/-}$ fish each.
At each time point, 4 fish at time were anesthetized in 1x tricaine, embedded in 2% methylcellulose in MilliQ water, positioned with a pipette tip, and lateral and dorsal images were acquired with brightfield Leica M165FC microscope equipped with a DFC7000T digital camera.
The parameters considered for the analyses were: tip to pectoral fin, posterior brain width and inter eye distance for dorsally orientated fish; head height, eye diameter and body length for laterally oriented ones.
The measurements were then performed using Fiji/ImageJ software and data obtained from each sample were normalized on its body length.
Finally, statistics and plots were generated using GraphPad Prism.

4.4.3. DanioVision locomotor assay

To investigate possible photoresponse changes in *nlgn2* mutants, the larvae locomotor activity was evaluated at 7 and 14 dpf through a DanioVision (Noldus) light-dark cycle protocol.
3 independent biological replicates for each genotype (WT vs *nlgn2a*$^{-/-}$, WT vs *nlgn2b*$^{-/-}$), with 12 fish for each replica, were put in a multi-well (24) plate added with 1 mL Fish Water. The DanioVision chamber is equipped with a water recirculation system that provides a continuous flux of deionized water at constant 28°C, creating a favorable environment for the fish' swimming activity.
The chamber is also equipped with a digital camera for live tracking of the animals. The protocol consists of a first 20-minute habituation phase, after which the trial starts, consisting of 10 minutes of light followed by 10 minutes of dark, repeated 3 times.
The EthoVision integrated software calculates the mean distance covered by each fish every 2 minutes. Finally, the resulting plots were generated using GraphPad Prism.

4.5. UAS Plasmids

All the plasmids amplified meant for single neuron labeling or identification of specific types of synapses took advantage of the Gal4-UAS system.
This system is composed of an activator (Gal4) and one or more effector (UAS) lines [35] and is a diffused technique for tissue/cell population targeting in zebrafish.
Briefly, the technique is based on the expression of the yeast Gal4 transcription factor expressed under the control of a tissue or cell-type-specific promoter, such as *id2b* or *vglut*. The effector lines carry in their construct the Upstream Activating Sequence (UAS), a ~15 base pairs (bp) sequence needed for the binding of Gal4 and the expression of the construct, usually encoding a fluorescent protein. This system allows to precisely identify specific cell populations with a fluorescent signal as readout.

4.5.1. Plasmids for single neuron labeling

Plasmids #64 (UAS:Tomato-caax), #245 (UAS:mCerulean-caax) and #300 (UAS: GFP-caax) were provided by Max Planck Institute for Neurobiology in Munich.
Each plasmid contains a 10x UAS element to which the Gal4 transcription factor expressed by the *id2b* transgenic construct will bind.

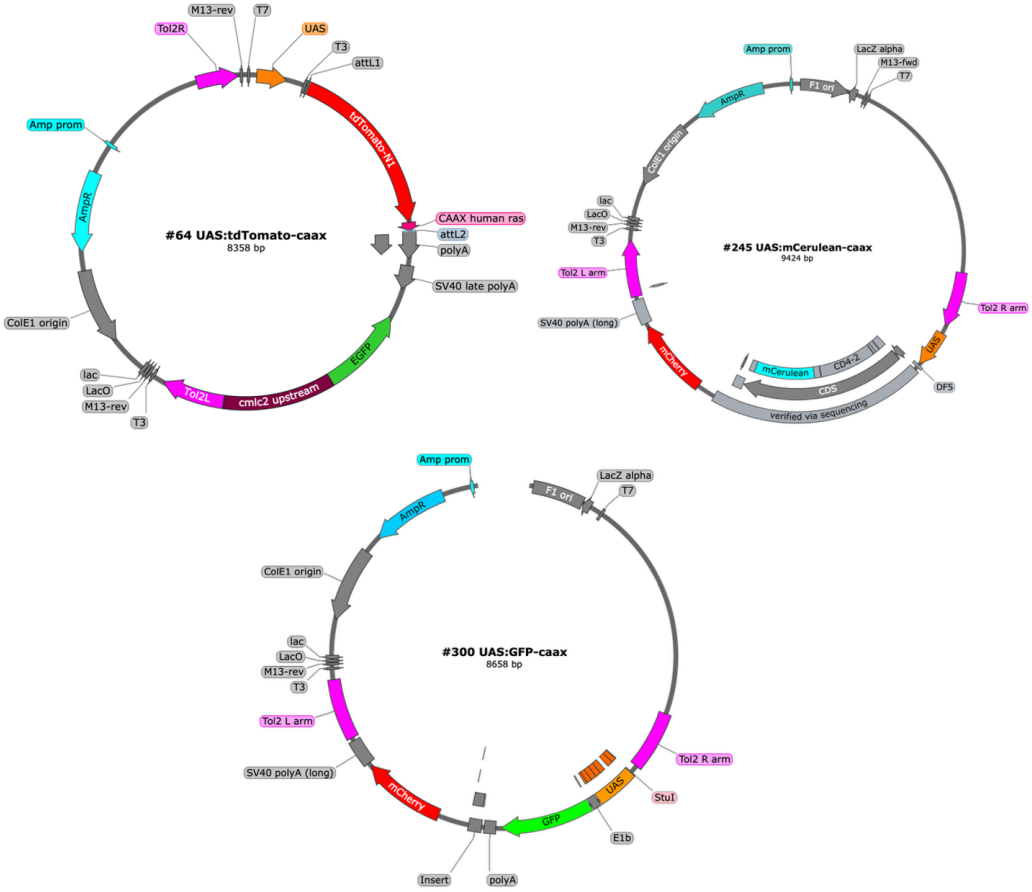

***Figure 15**: **UAS plasmids maps visualized in Snapgene**. Each plasmid is characterized by the presence of 10x UAS repeats with downstream elements such as the fluorescent marker (TdTomato, mCerulean or GFP) and the CAAX motif for membrane localization.*

Each of these plasmids contained an ampicillin resistance element which was later helpful in the selection of correctly transformed colonies when performing cell transformation.

Each fluorescent reporter was also added with a membrane-localizing element, the Cysteine-Alanine-Alanine-X (CAAX) motif. This C-terminal motif undergoes a series of post-translational modifications which result in the generation of a hydrophobic C-terminal domain, targeting the protein to the endomembrane system. Here, the protein will be additionally processed and transported to the plasma membrane (PM) [36].

This element was helpful in obtaining an acceptable fluorescent signal at the level of axons, dendrites and spines.

These plasmids also contain controls for the integration of the plasmid. These controls are based on the expression of a fluorescent protein (mCherry for plasmids #245 and #300, eGFP for #64) under the control of a cardiac-specific promoter (*cmlc2*). This promotes expression of fluorescent reporter at the level of the heart,

allowing identification of injection-positive samples even when the Gal4 expression is not present.

4.5.2. Plasmids for excitatory and inhibitory synapse imaging

Plasmids used for imaging of excitatory (UAS:FingR-PSD95-GFP) and inhibitory (UAS:FingR-GPHN-mKate) synapses were purchased from Joshua Bonkowsky lab (Addgene plasmids #72638 and #72639, respectively).

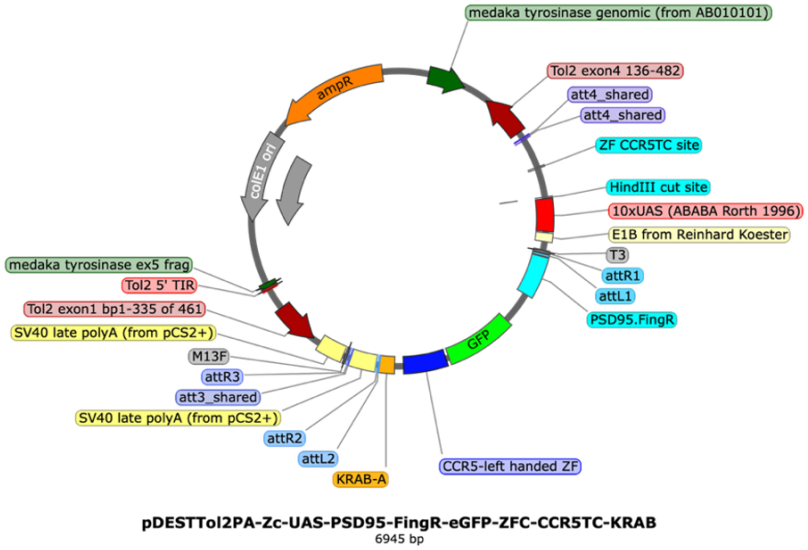

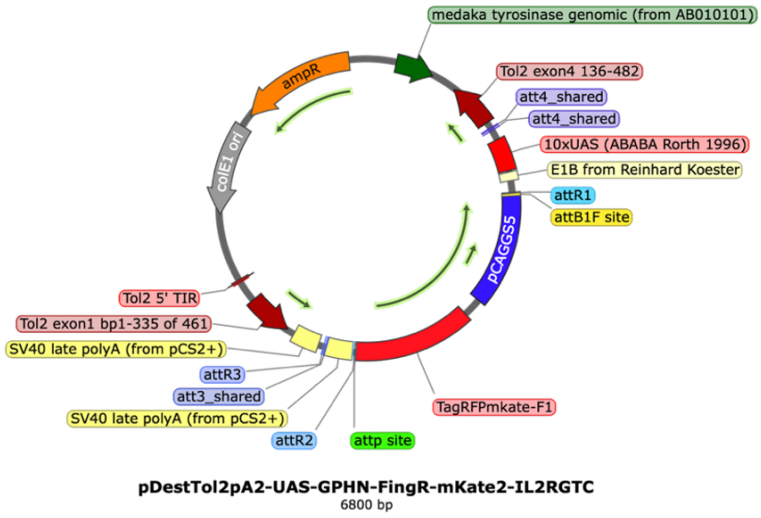

Figure 16: *UAS:FingR-PSD95/GPHN plasmid maps visualized in Snapgene. Each plasmid contains the 10x UAS element with downstream element that allow binding of the endogenous protein while controlling fluorescence through the KRAB-A element.*

The generation and function of these engineered plasmids has been previously described [37].
Briefly, PSD95-FingR and GPHN-FingR constructs were cloned into Tol2-based UAS plasmids, fused with GFP and mKate fluorophores, respectively.

Fibronectin antibodies generated by mRNA display (FingRs) are meant to target endogenous synaptic proteins, in this case postynaptic density 95 (PSD95) and gephyrin (GPHN).

PSD95 is a scaffolding protein belonging to the family of MAGUK (membrane-associated guanylate cyclase) proteins, localized in the postsynaptic compartment of excitatory (glutamatergic) synapses, enriched in dendritic spines. PSD95 interacts with N-methyl-D-aspartate receptors (NMDARs) and AMPA receptors (AMPARs) and is involved in synapse maturation [38].

Gephyrin, on the other hand, is a member of the postsynaptic compartment of inhibitory synapse and directly interacts with NLGN2.

Based on the different function and synaptic type localization, these two proteins can be employed to identify functional excitatory and inhibitory synapses, and UAS: FingR plasmids were employed for this purpose.

Briefly, Gal4 induces the expression of FingR protein, engineered to bind the specific protein of interest, emitting fluorescent signal in discrete synaptic puncta.

To prevent overexpression of the fluorescent protein which could reduce resolution, the excess FingRs, through the Zinc Finger domain, bind the zinc-finger binding site upstream the UAS, and the KRAB(A) domain inhibits further transcription.

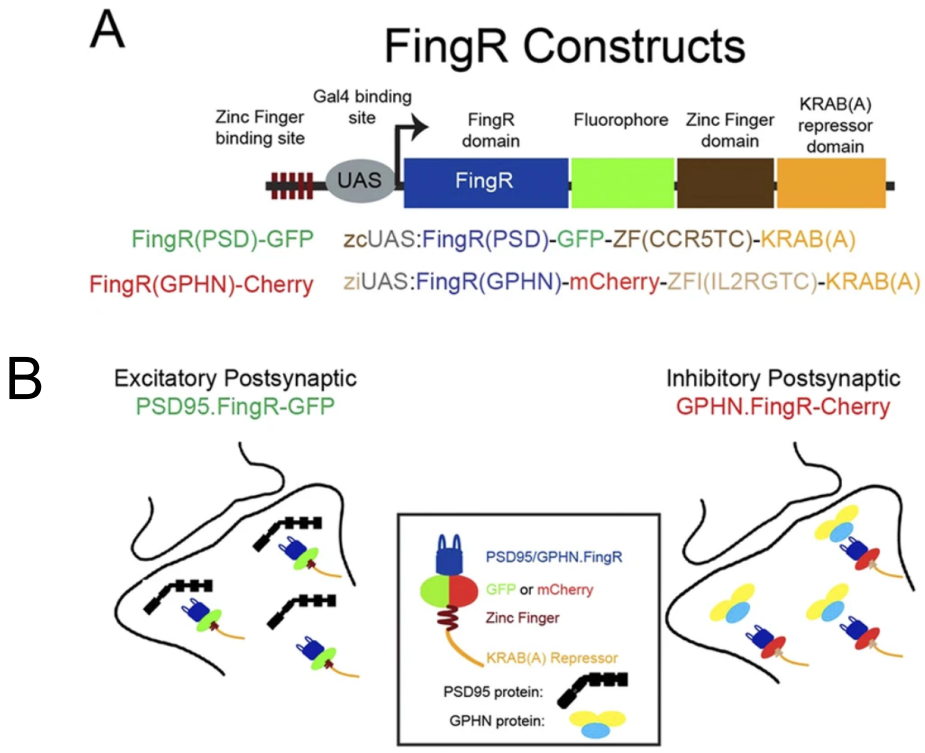

***Figure 17**: **Structure and components of the FingR-PSD95/GPHN plasmids and different synaptic localization**. (A) The FingR constructs contain the UAS sequence for Gal4 binding, the FingR domain for protein binding, the fluorophore for punctae imaging, and the zinc finger and KRAB(A) domains for regulation of the expression. (B) Overview of the functioning of the constructs in excitatory (PSD95.FingR-GFP) and inhibitory (GPHN.FingR-mCherry) synapses (modified from Son J. H. et al, 2016).*

4.6. Tol2 transgenesis

4.6.1. Plasmid amplification and purification

To obtain highly concentrated UAS plasmid vials for injections, DNA was amplified through bacterial transformation of chemically competent One Shot® TOP10® *E. coli* (ThermoFisher).

Briefly, for each plasmid 50 µl vial of One-Shot® cells was added with 1 µl of plasmid resuspended in RNase-free water. After 30 minutes of ice incubation, the samples were incubated for 30 seconds at 42°C in water bath. This step increases the membrane permeability to facilitate the plasmid uptake.

Cells were added with 250 µl of SOC medium and put in a shaker at 37°C at 225rpm for 1 hour.

100 µl of each ligation vial was spread and incubated in LB agar solid medium added with ampicillin 1:500 overnight at 37°C. LB solid medium composition was the following: 1% Tryptone (Sigma-Aldrich), 1%NaCl, 0,5% yeast extract (Sigma-Aldrich) and 1,5% Select agar (Sigma-Aldrich), added with ampicillin 1:500 in distilled water.

Selection of correctly transformed colonies was assessed through antibiotic resistance which was provided by the plasmid construct itself.

For each plasmid injected, 2 single positive colonies were picked and were grown in LB liquid culture on a shaker overnight at 37°C.

Subsequently, amplified plasmids were purified through a plasmid Midi kit (Qiagen®). Bacterial cells were first centrifuged at 6000 x g for 15 minutes and added with Buffer P1 (4 ml), P2 (4ml) and P3 (4ml) and incubated on ice for 15 minutes.

Then, samples were centrifuged for 30 min at ≥ 20.000 x g for 30 minutes at 4°C and the supernatant containing plasmid DNA was collected and centrifuged at ≥ 20.000 x g for 15 min at 4°C. Then, the the Qiagen-tip 100 was first equilibrated with 4 ml of QBT Buffer and the supernatant previously obtained was added. After two washes with 10 ml of Buffer QC, the DNA was eluted in 5 ml Buffer QF.

Finally, DNA was precipitated by adding 3.5 ml isopropanol and centrifuged at ≥ 15.000 x g for 30 min at 4°C. The obtained pellet was then washed with 2 ml 70% ethanol and centrifuged at ≥ 15.000 x g for 10 min. The pellet containing the purified plasmid was dried first and then redissolved in RNase-free water.

Resulting DNA concentrations were assessed using NanoDrop One spectrophotometer. For each sample, 1 µl of purified plasmid absorbance was measured by the instrument with resuspension buffer as blank.

After this step, samples could be conserved at -20°C for long-time storage**.**

4.6.2. Plasmid digestion with restriction enzymes

Correct DNA content of each plasmid was validated through a restriction enzyme digestion assay (Promega). All plasmids were incubated with restriction enzyme HindIII (Promega), and expected band number and bp sizes were predicted with the plasmid map editor ApE [39].
The reaction mix composition was the following:

Component	Volume/concentration
HindIII 10X Buffer	2 µl
Acetylated BSA, 10 µg/µl	0.2 µl
HindIII enzyme, 10 u/µl	0.5 µl
Plasmid DNA	1 µg/µl, 1 µl
RNase-free water	Up to 20 µl final volume

Table 7: Mix composition for HindIII restriction enzyme assay.

For each bacterial colony, a sample incubated with the restriction enzyme (cut) and without it (uncut) was prepared.
Samples were then incubated for 2 hours at 37°C. Finally, loading buffer OrangeG was added and electrophoresis was performed on a 0,8% agar gel in TBE for 30 minutes at constant 100V. Resulting gel images were acquired with Uvitec HD 9 Eppendorf.

4.6.3. Transposase amplification and in vitro transcription

In order to achieve stable insertion of the plasmids in zebrafish eggs, the transposase mRNA was needed in the injection mix. [40].
This enzyme catalyzes the excision of the donor plasmid by binding to the Tol2 elements flanking the sequence of interest, ultimately allowing stable insertion in the host genome.

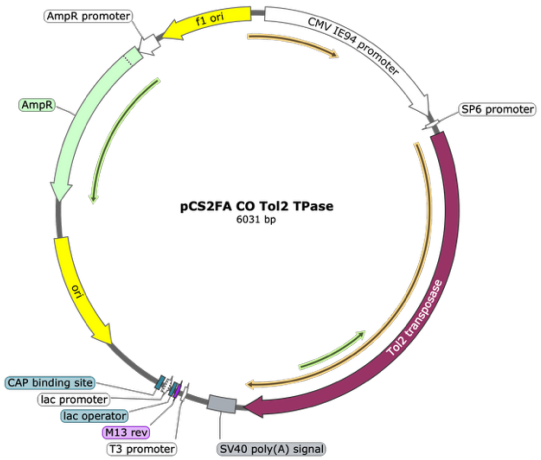

***Figure 18**: **Tol2 plasmid map visualized in SnapGene**. The plasmid contains an ampicillin resistance (AmpR) element, which was later useful in the selection of succesfully transformed colonies.*

After a first step of amplification similar to the one followed for the UAS plasmids amplification, the *in vitro* transcription was performed.

Firstly, the purified plasmid was linearized using NotI restriction enzyme (Promega) digestion protocol.

Briefly, 10 ng of plasmid were incubated with 0.5 µl NotI restriction enzyme 10u/µl, 2 µl RE 10X buffer, 0.2 µl acetylated BSA 10 µg/µl, diluted in RNase-free water to a total volume of 50 µl.

The reaction was held overnight at 37°C on a thermocycler.

To verify successful linearization reaction, 100 ng of uncut vector and 2 µl of cut vector was added with Orange G loading dye and electrophoresis was performed on a 2% agar gel in TAE.

After validation, the cut DNA was purified using GeneJet DNA cleanup Micro kit.

Once the DNA was purified and quantified, the mMESSAGE mMACHINE® in vitro transcription kit was used.

The reaction mix was composed as follows:

Component	**Amount**
Enzyme mix	2 µl
Linear template DNA	1 µg
10X reaction buffer	2 µl
2X NTP/CAP	10 µl
Nuclease-free water	To 20 µl

Table 8**: **Reaction mix for in vitro transcription

The reaction was incubated at 37°C for 1 hour and finally an RNA cleanup protocol was followed (RNeasy MinElute cleanup Kit, Qiagen).
Ultimately, DNA concentration was assessed using Nanodrop One spectrophotometer.

4.6.4. Microinjections and screening

To generate both the newly established UAS reporter lines and to obtain single-neuron labeling for confocal imaging, plasmid microinjections in eggs at early developmental stages were performed.
The day before the injection, selected males and females were put in the same breeding tank, separated by a divisor. In the morning of the injection day, the divisor was removed, and eggs were immediately collected.
Injection of one- to eight-cell stage embryos was performed with an injection mix composed as follows:

Component	Concentration/volume
Plasmid DNA	80 ng/µl
Tol2 transposase	50 ng/µl
Phenol red 1x	0.5 µl
Danieau solution 1x	0.16 µl
RNase-free water	Up to 5 µl total volume

***Table 9**: Microinjection mix solution composition.*

Danieau 1x was composed of: 58mM NaCl, 0.7mM KCl, 0.4 mM $MgSO_4$, 0,6 mM $Ca(NO_3)_2$, 5mM HEPES pH 7.6) [41].
Once the eggs were collected with a strainer, they were aligned on a glass slide, and the injection needle was loaded on the minipump injector.
The injections performed on eggs derived by incross of *TgBAC(id2b:GAL4-VP16,myl7:VP16)* fish and meant for single-neuron labeling differed only in the plasmid DNA amount injected, which was set to 40 ng/µl.
After the injections, eggs were put in a 25 ml Petri dish with fish water and incubated at 28°C with a 12h/12h light/dark cycle.
At 1 dpf, unfertilized or rotten eggs were removed and at 5 dpf, embryos were screened with Zeiss Axio Zoom V16 fluorescent microscope for fluorescence associated with the plasmid construct for single neuron labeling (GFP) together with mCherry signal which labeled the whole tectum.
Larvae were anesthetized in 1x tricaine-added 25 ml petri dish, and positive larvae were selected for confocal imaging at 8 dpf.

4.7.Genotyping

To verify the correct integration of the plasmids containing the UAS constructs that were missing the positive injection control (*bleeding heart*, BH) and to verify the genotype of *nlgn2* mutants, Polymerase Chain Reaction (PCR) genotyping was performed.

PCR is a widely used gene expression technique able to amplify genomic region of interest thanks to targeted repeated cycles of DNA replication. This is achieved through the designing of specific primers spanning the region of interest. The presence of amplified DNA can then be visualized through electrophoresis of the samples in agar gel in order to separate DNA content based on their size, and bands can be visualized through a transilluminator exciting the DNA-binding dye, (i.e. Midori Green®).

For DNA extraction, the Hot Sodium Hydroxide and Tris (HotSHOT) protocol was followed.

Adult zebrafish were anesthetized in 1x tricaine and a small piece of caudal tail fin was cut, added in 0.5 mL tubes with 40 µl NaOH 50mM and incubated at 95°C for ~20 minutes, until the samples were visibly dissolved. After this step, the samples were briefly mixed through vortex.

The extracted DNA at this step can be stored at 4°C for ~3 months and at -20°C for long-term storage.

Forward and reverse primers were generated through Primer3web (version 4.1.0) and designed specifically to amplify the 10x UAS-containing region of the plasmids. Thus, the following primers were designed:

Primer name	**Sequence**
UAS_Forward	5’ - TCACTATAGGGCGAATTGGGT - 3’
UAS_Reverse	5’ - CTCTAGAGTCGACCCTTGCC - 3’

***Table 10**: 5’-3’ sequence of primers designed for amplification of the 10x UAS element of the plasmids.*

The expected size of the amplification products was 723bp for UAS:PSD95 plasmid and ~330bp for both UAS:GPHN and UAS:Tomato-caax (#64) plasmids.

The primers used to verify the genotype of *nlg2a* mutants after confocal imaging were the following:

Primer name	Sequence
nlg2a_Forward	5’ – GGAGACCGTCGCTTTCAG – 3’
nlg2a_Reverse	5’ – CTCGGGCAAAACACCATGAA – 3’

Table 11: 5’-3’ sequence of primers designed for nlgn2a exon 3..

The PCR mix for each sample was composed as follows:

Component	Volume
RNase-free water	6.5 µl
HOT FIREPol® Blend Master Mix RTL 5X	2 µl
Forward primer (10 µM)	0.25 µl
Reverse primer (10 µM)	0.25 µl
DNA	2 µl

Table 12: PCR master mix composition.

The HOT FIREPol® mix contains a chemically modified DNA polymerase enabling hot start, preventing DNA extension at low temperatures, thus avoiding unwanted DNA amplification.
The PCR parameters were the following:

Phase	Temperature	Duration	Number of cycles
Initial denaturation	95°C	13 min.	1
Denaturation	95°C	15 sec.	34
Annealing	62°C for 10X UAS 59°C for *nlgn2a*	30 sec.	34
Extension	72°C	40 sec.	34
Final extension	72°C	5 min.	1
Hold	4°C	∞	1

Table 13: PCR parameters for genotyping.

After the PCR cycles were completed, electrophoresis was performed in 1% agarose gel in TAE for UAS genotyping, and 4% TBE for *nlgn2a*, both added with 2 µl Midori Green (Nippon Genetics) as intercalant agent.
The electrophoretic run lasted for 20 minutes at constant 110V, and gel images were acquired with Uvitec HD 9 (Eppendorf®).

4.8.Imaging

4.8.1. Confocal microscopy

Confocal imaging was performed on 8dpf alive embryos.
For live imaging, larvae were anesthetized with tricaine 1x and embedded in low-melting 2% agarose gel added with tricaine 1x on a small petri dish.
The agarose gel was pre-heated at 65°C to allow its melting and the embedding of the larvae, which were positioned dorsally. Once the gel completely solidified, the petri dish was added with 1x tricaine fish water to avoid the fish movement during z-stack acquisition. Confocal microscopy is a commonly used imaging technique characterized by higher resolution capabilities compared to standard light microscopy. Laser scanning-based confocal microscopes (LSCM) systems are the most common. Confocal microscopy principle relies on a point source of light which is focused by the objective lens on a single point of the sample. The emitted fluorescence passes through the objective lens, a pinhole to discard out of focus light, and is detected by a photomultiplier (PMT), a device which detects incident photons and converts the light signal into an electric one. Once the single point is acquired, the fast-scanning mirror focuses the excitation light on a different point of the sample, ultimately scanning the whole sample on a single confocal plane to give a high-resolution image with reduced noise given by out-of-focus light.
Once a single plane image is acquired, a new focal point is set, and the laser scanning cycle starts again. By doing so, is possible to obtain and combine together confocal image planes (z-stacks) from which 3D reconstructions of the sample can be generated [42].

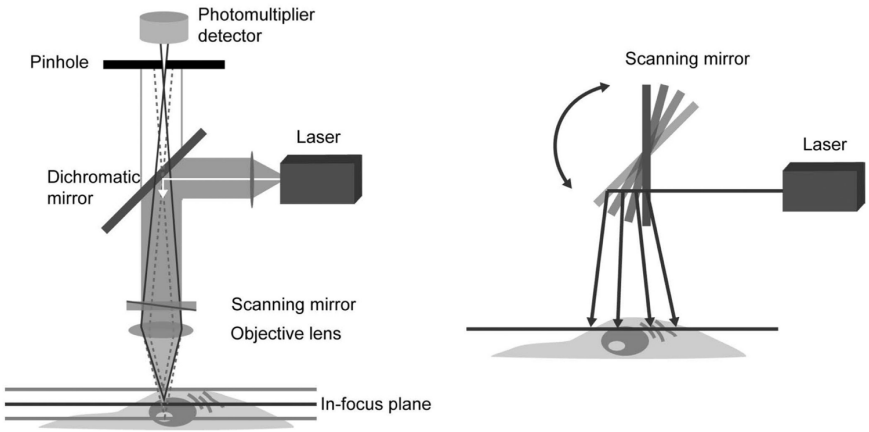

***Figure 19**: **Confocal microscopy principle and components.** The laser source light is reflected by the dichromatic mirror towards the fast-scanning mirror and the objective lens towards the sample. Reflected light then focused on the PMT (from Elliot A.D., 2020)*

Confocal microscopy was performed using Zeiss LSM900 Airyscan2 microscope with a 40x1 Numerical Aperture (NA) water immersion objective, equipped with lasers excitation filters for fluorophores of interest.
Based on the fluorophore excited, specific laser excitation and emission wavelength filters were selected:

Fluorophore	Excitation laser wavelength	Emission laser wavelength
GFP	488 nm	510 nm
TdTomato	556 nm	583 nm
mCherry	587 nm	610 nm

Table 14: Excitation and emission wavelength filter for confocal microscopy.

Stacks were acquired with 1024x1024 pixel image size, 0.8-1x zoom, 0.5-1 μm z-step size, unidirectional scanning, 2.06 μs pixel time and 2x image averaging to increase resolution.
Laser intensity was adjusted to avoid saturation or bleaching of the sample and a single neuron stack for each larva was acquired.

4.8.2. Transmission Electron Microscopy (TEM)

8 and 11dpf WT, *nlgn2a*$^{-/-}$ and *nlgn2b*$^{-/-}$ larvae heads were fixed with 2.5% glutaraldehyde (EMS, Hatfield, PA, USA) plus 2% paraformaldehyde (Sigma-Aldrich) in 0.1M sodium cacodylate buffer pH 7.4 overnight at 4°C.
Then, samples were post-fixed in 1% PFA in 0.1 M sodium cacodylate buffer for 1 hour at 4°C. After three washes, samples were dehydrated in graded ethanol series and embedded in epoxy resin (Sigma-Aldrich).
Ultrathin sections were obtained with Leica Ultracut EM UC7 ultramicrotome, counterstained with uranyl acetate and lead citrate.
Imaging was performed with a Tecnai G2 transmission electron microscope (FEI) operating at 100 kV. Images were captured with a Veleta digital camera (Olympus Soft Imaging System).

4.8.3. Brain spontaneous activity recordings with two-photon microscopy

We recorded whole brain spontaneous activity in *nlgn2a* mutant and WT fish at 7 dpf using volumetric two-photon microscopy [43]. We used Tg(elavl3:H2B-GCaMP6s*)* fish embedded in 2% low melting point agarose without anesthesia.

The custom multiphoton system is equipped with a Ti:Sapphire source (Chameleon Ultra II Coherent) tuned to 920nm for the excitation of the GCaMP6s molecule and operating with a 16x water dipping objective (Nikon Instruments). The volumetric acquisition relies on an 8 kHz lateral scanner coupled with an Electrically tunable lens (ETL, Optotune EL-10-30-C-IR) for the refocusing along the z axis. All the acquisition were set as such to acquire 2 volumes per second and 15 planes per volume, with a plane-to-plane separation of about 12 µm, with respect to a typical cell diameter of about 6.5 µm. The emitted signal was routed toward a detection arm equipped with an emission filter (Semrock Technologies, 535/50nm) and a GaAsP PhotoMultiplier Tube as detector (H7422PA-40, Hamamatsu Photonics).

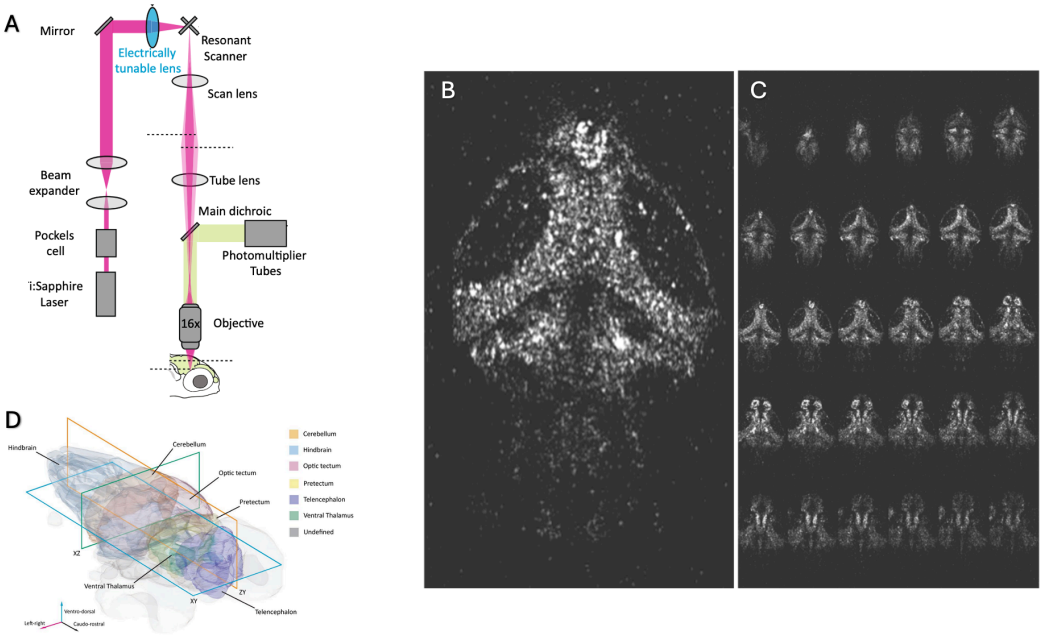

***Figure 20**: **Whole brain Multiphoton Imaging at cellular resolution.** **(A)** The hardware configuration of the custom multiphoton microscope used for the acquisition of the spontaneous brain activity, equipped with a 8 kHz resonant XY scanner and an Electronic Tunable Lens for the fast Z scan. **(B)** A single plane of the acquired volume capturing the optic tectum, the cerebellum and the hindbrain centers from fish with pan-neuronal expression of GCaMP6s (elavl3:H2B-GCaMP6s). **(C)** The different planes acquired. The System can operate at 1 volume per second with the acquisition of 30 planes or 2 volumes per second with the acquisition of 15 planes. **(D)** The anatomical organization of the zebrafish brain with the most prominent regions highlighted in different colors.*

Following 1h acquisition of the functional data for the spontaneous activity, the acquisition parameters were adjusted to obtain a higher-resolution anatomical stack for the annotation of the identified cells to specific brain regions.

The data analysis was performed by dott. Marco Salamanca and dott. Marica Albanesi. Briefly, the raw acquisition files firstly underwent motion-correction using Suite2P, a Python-scripted image processing pipeline that allows also automated cell bodies identification identifying the putative ROI. The fluorescent

intensity data were fitted to an exponential decay kernel function incorporating a decay time (τ_{off}) of 3.5 seconds to capture GCaMP6s responses.
To analyse spontaneous network dynamics, single-cell calcium signals were extracted, low-pass filtered, and normalized via Z-score. Overall network activity was represented by the population mean trace, calculated by averaging the Z-scored traces of all valid cells at each time point. To quantify the frequency distribution of this synchronous activity, we computed the Power Spectral Density (PSD) using Welch's method. The time-domain signal was divided into 60-second overlapping segments, windowed, and subjected to a Fast Fourier Transform (FFT) to compute the average periodogram. Absolute oscillatory power was then integrated across two defined frequency bands: Infra-Slow Oscillations (ISO, < 0.1 Hz) and Slow Oscillations (0.1–0.3 Hz). To rigorously evaluate the magnitude of regional differences between WT and *nlgn2a*$^{-/-}$ groups, independent of statistical limitations related to small sample sizes, we quantified the effect size using Cohen's d. This was calculated as the difference between the group means divided by the pooled standard deviation, which was weighted by the degrees of freedom to accurately estimate overall variance. By convention, positive d values denote higher power in the WT group, whereas negative values indicate higher power in the mutants. For 3D spatial mapping and regional quantification, we applied a strict threshold of $|d| > 0.8$ (standard cutoff for a "large" effect size) to exclusively isolate and visualize brain regions displaying a robust and strongly penetrant mutant phenotype.

4.9.Single-cell RNA sequencing and Gene Ontology (GO) analyses

A scRNA-seq experiment was performed on 21 dpf WT, nlgn2a$^{-/-}$ and nlgn2b$^{-/-}$ brains, with 3 brains per condition. Each fish was sacrificed in ice-added water, and the brain was extracted with sterile tweezers and scalpel.
To isolate the nuclei, we used the Minute™ Single Nucleus Isolation Kit for neuronal tissues. Each tube containing the brains was added with 700 µl of cold Buffer A and homogenized using a pestle. Then, the tubes were incubated on ice for 5 minutes and the homogenate transferred to a filter in a collection tube. After 10 minutes of incubation at -20°C, the tubes were centrifuged at 13.000 x g for 30 seconds. The flow-through was centrifuged at 600 x g for 5 minutes and the supernatant discarded. The pellet was resuspended on 200 µl PBS with 5% BSA and added to 1 ml of cold Buffer B in a new Eppendorf tube. After centrifugation at 1.000 x g for 10 minutes, the pellet was resuspended in 200 µl PBS with 5% BSA.
To fix the extracted nuclei for sequencing, we used the Evercode Nuclei Fixation v3 kit. For each sample, 100.000 counted nuclei were transferred to a BSA-coated

tube and centrifuged for 10 minutes at 500 x g at 4°C. The pellet was resuspended in 187.5 µl of nuclei Prefixation Master mix. Each sample was then transferred to a new tube through a cell strainer and added with 62.5 µl of Fixative solution and incubated on ice for 10 minutes. 20 µl of Permeabilization solution were then added, mixed by pipetting, and incubated on ice for 3 minutes.
The fixation was then blocked by adding 250 µl of Fix and Perm Stop Buffer and centrifuged for 10 minutes at 500 x g at 4°C. Each pellet was then resuspended in 100 µl of Nuclei Storage Master Mix and collected in a new 1.5 ml tube through a cell strainer. The fixed nuclei were then stored at –80°C for the following sequencing.
The scRNA-seq was then performed by the laboratory coordinated by Prof. Paolo Martini of the Department of Molecular and Translational Medicine of the University of Brescia.
Whole transcriptome single-cell RNA sequencing was performed using Parse Evercode WT kit using 8 different libraries, with a mean mapping percentage of ~42.5%.
Raw gene counts were obtained using PARSE pipeline with *Danio rerio* set as reference genome (GRCz11). Cells were filtered for a minimum of 100 features and 100 UMI counts and a mitochondrial ratio < 2%, clustered based on gene expression and assigned to specific cell types using SingleCellNet, identifying 9 distinct cell clusters.
Differential Gene expression analyses were performed using the FindMarkers function in Seurat, and finally Gene Ontology (GO) analyses were carried out.

4.10. Image and data analysis for cell morphology

4.10.1. Image processing

Stacks and maximal projections images were visualized using ImageJ/Fiji software. Three-dimensional images of single neurons to recognize tectal PyrNs were achieved with Fiji integrated 3D project plugin.
Skeletonized tracings of single neurons were generated with neuTube software [44]. Briefly, image stacks were loaded in the program, and the main process, axons and dendrites were semi-automatically traced and classified based on the tectal layer they were targeting by three-dimensionally rotating the stack.
For each neuron, a SWC file of the skeleton was generated and was later used for calculating arbor-specific total and mean lengths and spine densities values.

The retinotopic area for each dendritic arbor was calculated using Fiji software and was defined as the convex hull area for each arbor. Measurements were performed by connecting all the outer tips of each arbor on maximal projections.
Arbor-specific neurite lengths were calculated with the semi-automated neurite segmentation plugin Simple Neurite Tracer (SNT) in Fiji based on the skeletonized tracings previously generated with neuTube software.
Each SWC file contained annotations for each neurite, classified by the localization in the tectal layer (apical dendrites for SM, basal dendrite for SFGS and axon for SGC neurites). All the processes localized in each layer were measured with the analysis tool integrated in SNT as well as mean and total length values.
Spine density was measured by manually annotating spines localized in the SM-targeting layer of labeled neurons and normalized by the total length of the SM layer.
Strahler analyses were performed in SNT plugin and average bifurcation ratio values for each neuron were measured.

4.10.2. Statistics

Statistical analyses were performed using GraphPad Prism.
For each dataset, normality Shapiro-Wilk tests were performed and, accordingly, unpaired t-test (for normally distributed data) or Wilcoxon-test (for non-normally distributed data) were performed.
For multiple comparisons, one-way analysis of variance (ANOVA) followed by Tukey's HSD was carried out on normally distributed data, while Kruskal-Wallis followed by pairwise Wilcoxon tests with Holm correction for non-normally distributed data.
Differences were considered significant when $p < 0.05$ (*), $p < 0.005$ (**), $p < 0.001$ (***) and $p < 0.0001$ (****).

5. RESULTS

5.1.Neuroligin-2 gene expression

At first, we wanted to verify the spatial and temporal expression of *nlgn2a* and *nlgn2b* based on the existing data to assess whether the developmental timepoints of expression were quantitatively similar.

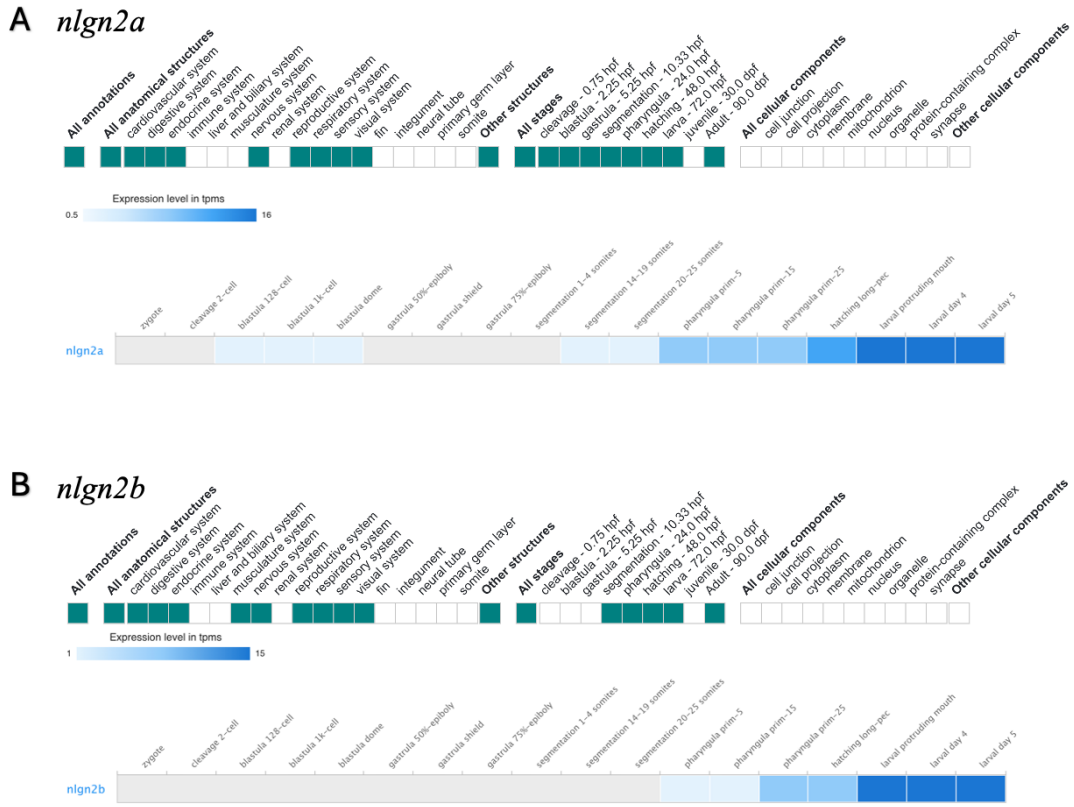

***Figure 21**: **Spatial and temporal expression of nlgn2a and nlgn2b**. (A) Expression patterns of nlgn2a transcript in anatomical structures and developmental stages, visualized in ZFIN. On the bottom, enlarged view of nlgn2a expression from zygote to larval day 5 with color-coded expression levels expressed in Transcripts per million (TPM), visualized in EMBL-EBI Expression Atlas.. (**B**) Similar plots for nlgn2b expression levels.*

As shown in Figure 21, the anatomical structures in which both paralogs are expressed is similar, except for *nlgn2b* expression detected also in musculature system. Both paralogs are expressed in cardiovascular, digestive, endocrine, nervous, reproductive, respiratory, sensory and visual systems. Regarding the temporal expression, both genes are expressed at similar levels, with consistent expression starting from the pharyngula stage (24 hpf) until 5 dpf. *nlgn2a* expression is present at low levels also at the blastula 128 cell stage, while *nlgn2b*

is not. Even though data regarding quantification of gene expression in adults is missing, RT-PCR showed consistent expression in adult brain [21].
Uniform Manifold Approximation Projection (UMAP) highlighted enriched expression of both paralogs in optic tectum and majorly the population of glutamatergic and GABAergic neurons. Temporally, the cluster expression is almost identical for both genes, with the expression in the neuronal clusters mentioned before present at later developmental stages.

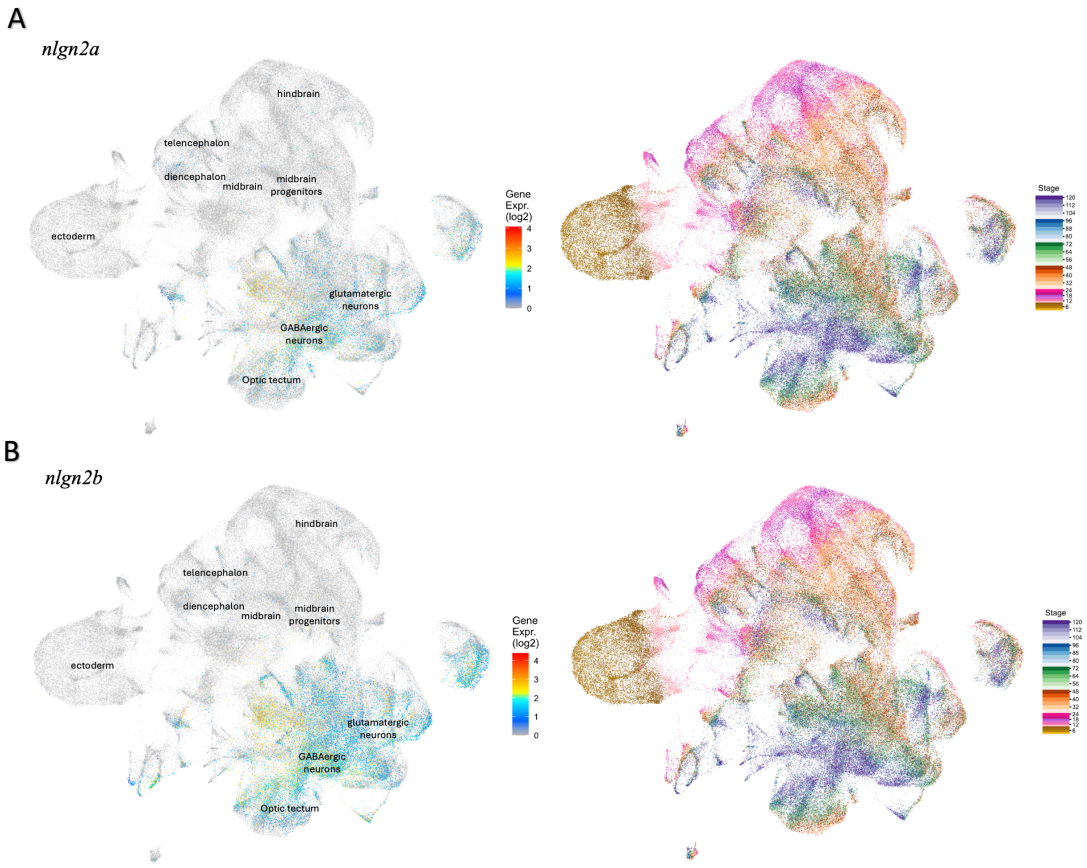

***Figure 22**: **Single-cell gene expression UMAP for nlgn2a and nlgn2b from Daniocell**. (**A**) UMAP projection of cells colored by nlgn2a gene expression (left), and developmental stage expressed in hpf (right). Cells are clustered according to different regions and neuron types. The developmental expression reports gene levels from 5 to 120 hpf. (**B**) Similar UMAP projections for nlgn2b.*

From this, we can deduce that the expression levels of *nlgn2a* and *nlgn2b* are similar both spatially and temporally.
We verified the efficacy of the CRISPR-Cas9 genome editing for the generation of *nlgn2a* and *nlgn2b* mutants evaluating the gene expression level through RT-qPCR on WT, *nlgn2a* $^{-/-}$ and *nlgn2b* $^{-/-}$ 7 dpf larvae. We normalized the relative mRNA levels on the *eef1α* housekeeping gene and relative gene expression values were calculated.

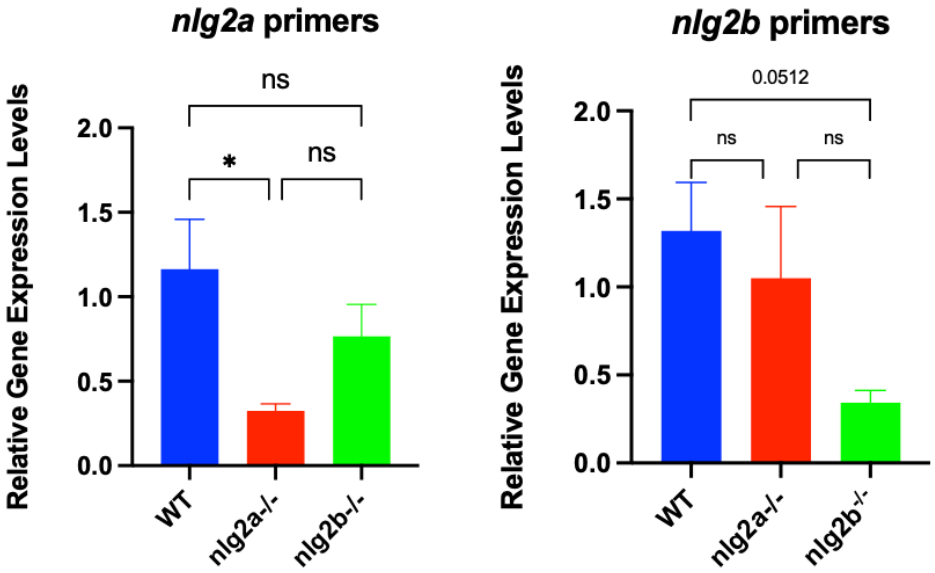

***Figure 23**: **Relative gene expression profiles of neuroligin-2 with RT-qPCR**. Quantification was performed on 3 biological replicates consisting of pools of 20 whole 7 dpf larvae (N total = 60). Data are presented as mean ± SD.*

As shown in Figure 23, the transcript levels of *nlgn2a* are significantly reduced (~70% decrease in mRNA levels) in *nlgn2a*$^{-/-}$ compared to WT, while no significant differences were found in *nlgn2b*$^{-/-}$ mutants when compared to WT.
Similarly, expression of *nlgn2b* in correspondent mutants is substantially decreased even though not significantly, while in *nlgn2a*$^{-/-}$ no differences were highlighted.
Taken together, these data indicate the decreased expression of the *nlgn2* paralog in the respective mutants and excludes the occurrence of compensatory mechanisms when one of the paralogs is mutated, at least at the mRNA level.

5.2. Viability and basic morphological characterization of *nlgn2* mutants

After confirming the effective a reduction of RNA expression for the two paralogs, we focused on the mutant fish survival rate and the anatomical features for the head and body to evaluate potential developmental delays.

5.2.1. Survival analysis

To assess whether the mutation affects the survival capabilities of the fish, 60 larvae per condition (WT, *nlgn2a*$^{-/-}$ and *nlgn2b*$^{-/-}$) at 7 dpf were selected as initial reference (100%) and put in housing tanks.

At 14, 21 and 28 dpf the relative percentage of survived larvae was measured to generate a survival Kaplan-Meier curve (Figure 24).

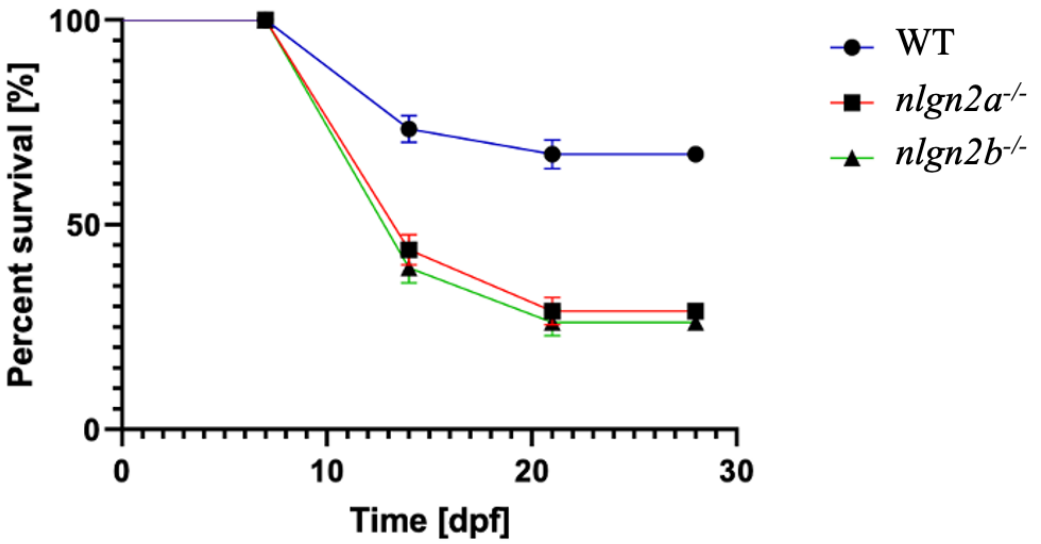

***Figure 24**: **Kaplan-Meier survival rate curve**. Data are obtained from 3 biological replicates of pools of 60 larvae per condition. Data are presented as mean ± SEM.*

In general, both *nlgn2a*$^{-/-}$ and *nlgn2b*$^{-/-}$ exhibit a significantly reduced survival rate compared to WT, with Log-rank (Mantel-cox) test p-values of WT vs nlgn2a$^{-/-}$ /nlgn2b$^{-/-}$ < 0,0001 in all the developmental timepoints considered. In fact, the mean survival rate at 28 dpf for WT is 67.2%, for *nlgn2a*$^{-/-}$ 28.9% and for *nlgn2b*$^{-/-}$ 26.1%. By looking at the curves, the most critical period, with the highest increase in mortality is evident, goes from 7 to 14 dpf. This is a critical phase, where the fish starts to feed autonomously and in which starvation is the main cause of mortality. Following this initial phase, the steepness of the curve starts to flatten and from 20 to 28 dpf it's stabilized around 30%.
These data show how the mutation significantly affects the viability of mutants, especially in the key developmental period between 7 and 14 dpf.

5.2.2. Morphometric alterations of nlgn2a/b mutants

We assessed the gross anatomical organization of the mutant fish throughout development, evaluating a number of morphological parameters across three time points (7, 14 and 21 dpf). The parameters considered were the head length (Tip to pectoral fin), posterior brain width, inter eye distance, head height, eye diameter and body length.

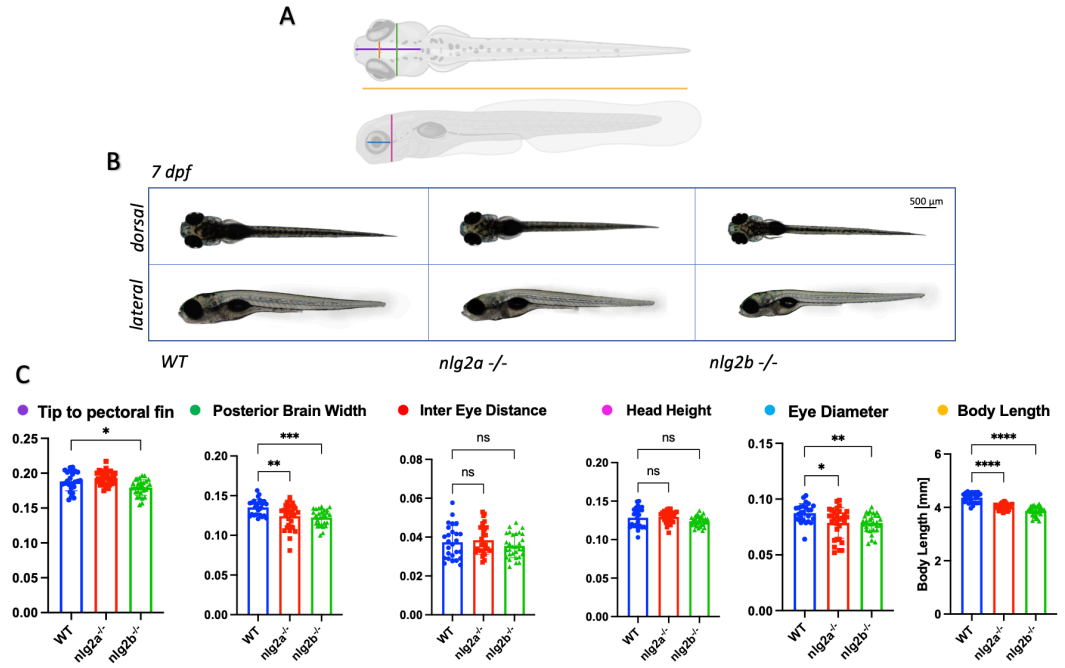

***Figure 25**: **Morphological measurements on 7 dpf WT and mutant larvae**. (**A**) Schematic representation of the morphological parameters considered. The color of the lines refers to the anatomical features of panel C. (**B**) Representative images of 7 dpf WT, nlgn2a$^{-/-}$ and nlgn2b$^{-/-}$ zebrafish considered for morphological characterization. (**C**) Quantification of morphological parameters normalized on the total body length. Data are represented as mean ± SD.*

The analysis at 7 dpf shows that the posterior brain width results significantly decreased in both mutants, as well as the eye diameter and the total body length. The tip to pectoral fin parameter is significantly reduced only in *nlgn2b*$^{-/-}$ larvae. The inter eye distance and head height are not affected.

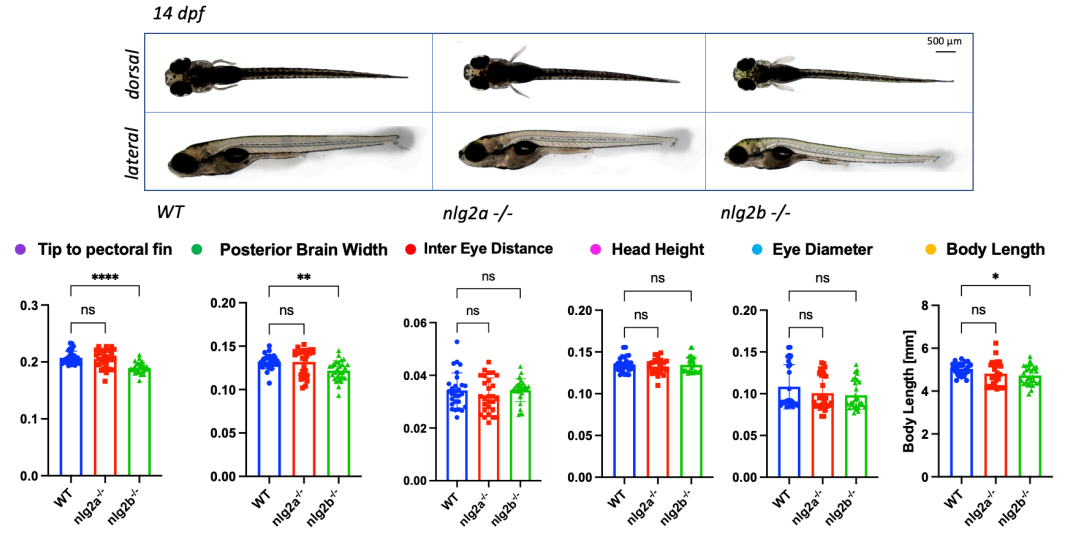

***Figure 26**: **Morphological measurements on 14 dpf WT and mutant larvae**. Representative images of 14 dpf WT, nlgn2a$^{-/-}$ and nlgn2b$^{-/-}$ zebrafish considered for morphological characterization and quantification similar to figure 25. Data are normalized on body length and presented as mean ± SD.*

At 14 dpf, significant alterations are detected only in *nlgn2b*$^{-/-}$ mutants, that exhibit reduced tip to pectoral fin, posterior brain width and total body length.

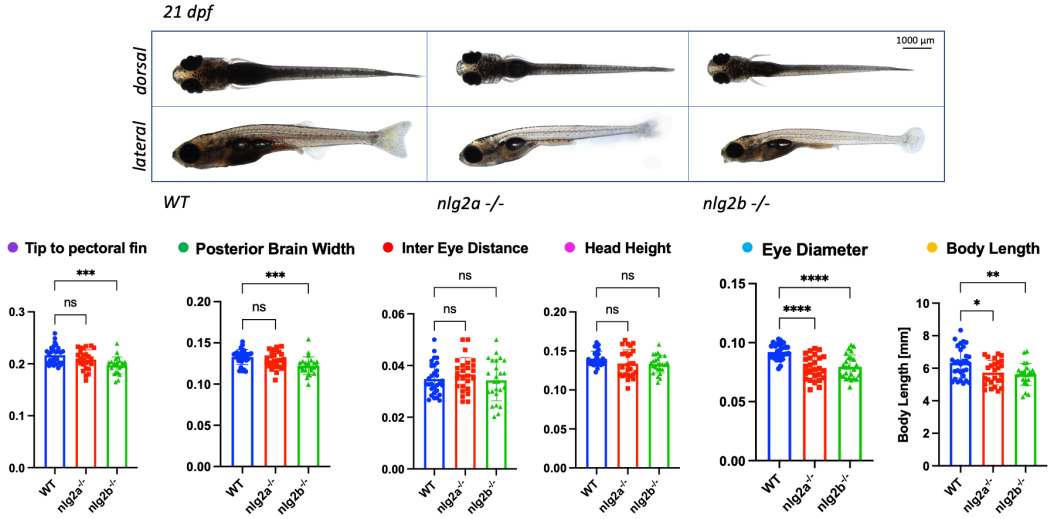

***Figure 27**: **Morphological measurements on 21 dpf WT and mutant larvae**. Images and relative quantifications were performed similarly the ones performed at 7 and 14 dpf. Data are represented as mean ± SD.*

Finally, at 21 dpf, the last timepoint considered, the alterations observed in *nlgn2b*$^{-/-}$ persisted. In *nlgn2a*$^{-/-}$ instead, we observe a significant decrease in eye diameter and body length.

Overall, these data suggest that *neuroligin-2* mutations affect the general anatomical organization of zebrafish in the fundamental developmental period that goes from the larval to the juvenile phase. The defects are persistent in *nlgn2b*$^{-/-}$, while *nlgn2a*$^{-/-}$ show a less pronounced pattern, with only significant decreased brain width and eye diameter at 7 dpf. Furthermore, the total body length is persistently decreased.

In conclusion, such features may be indicative of neurodevelopmental delays, with a stronger effect on *nlgn2b* mutants.

5.2.3. Mutants exhibit defects in photoresponse

Among the phenotypes observed, ASD is characterized also by altered locomotor activity, emerging as consequence of disrupted neural circuits, sensory processing or defective motor control.

To verify whether *nlgn2* mutants show functional alterations, we tested light-dependent locomotor activity through an established assay based on Danio Vision. For this characterization, two timepoints was evaluated, at 7 and 14 dpf, for both *nlgn2* mutants.

At 7 dpf, *nlgn2a*$^{-/-}$ larvae show increased total distance covered throughout the trial, specifically in light periods (Figure 28).

Moreover, while the WT consistently show a pattern with low locomotor activity in light and high activity in dark conditions. Indeed, evaluating the luminance perception index, i.e. the ratio between the mean value of distance covered in dark and the mean value of distance covered in light, the mutants do not show a similar pattern, and consequently exhibit a significantly decreased luminance perception index. At 14 dpf, these differences appear no more significant.

On the other hand, *nlgn2b*$^{-/-}$ mutants are characterized by a significant increase of distance covered in light at both 7 and 14 dpf (Figure 29). It's possible to see, specifically at 7 dpf, that the locomotor activity curve of the mutant shows a constant higher value of distance covered. A particular feature that emerges is also the gradual increase in activity in light periods, that in the WT is not occurring. Another interesting feature of both mutants, visible at 14 dpf, is that the locomotor activity in dark period seems to decrease progressively after each period, although only in the last one the value is lower compared to the WT one.

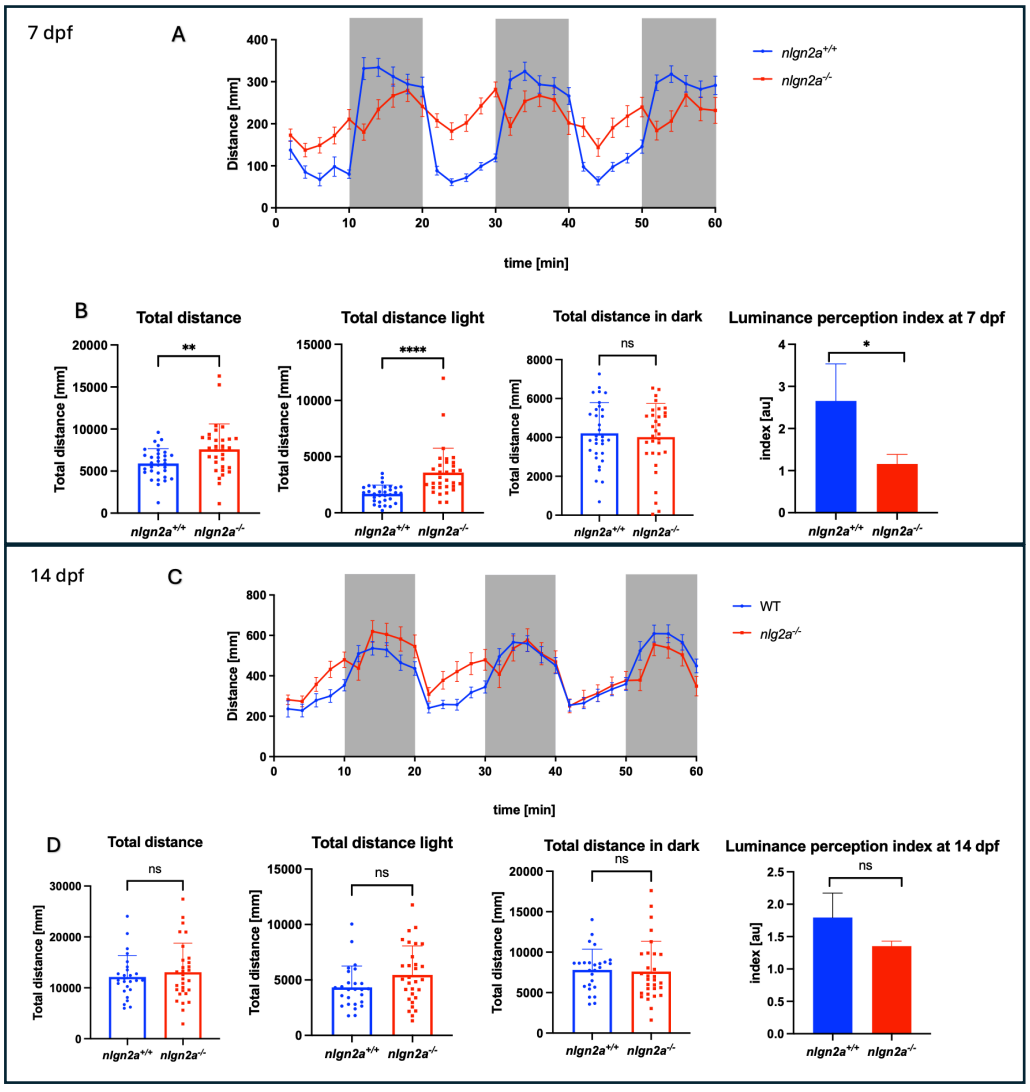

***Figure 28**: **Altered locomotor activity in nlgn2a$^{-/-}$ mutants**. (**A, C**) Locomotor activity curves in light-dark conditions obtained by 3 biological replicates of pools of 12 larvae per condition at 7 (**A**) and 14 (**C**) dpf. (**B, D**) Quantification of total distance across the whole experiment, in light or in dark conditions and luminance perception index quantification, defined as the ratio between the mean distance covered in dark and the mean distance covered in light, at 7 (**B**) and 14 (**D**) dpf. Data are presented as mean ± SD.*

.

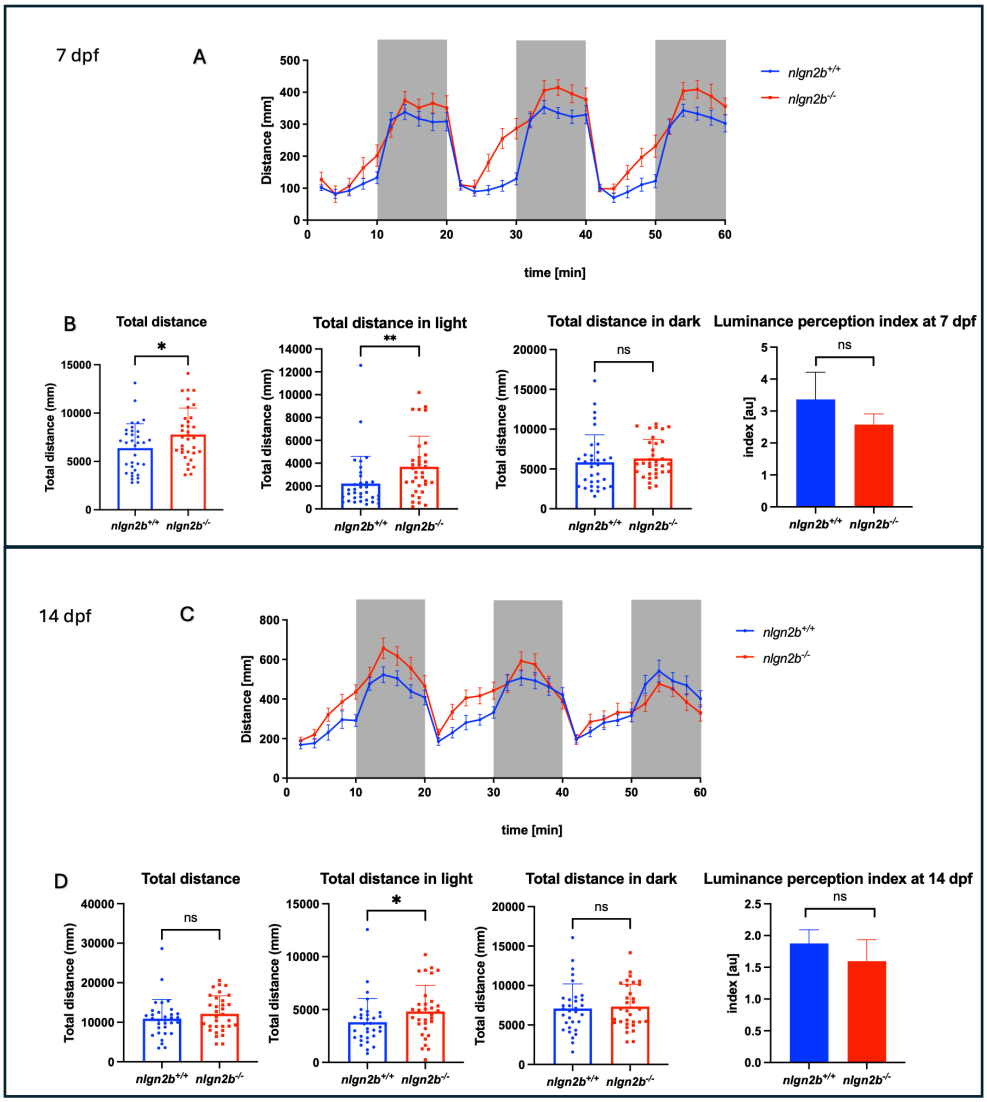

***Figure 29**: **Altered locomotor activity in nlgn2b$^{-/-}$ mutants**. (**A, C**) Locomotor activity curves in light-dark conditions obtained by 3 biological replicates of pools of 12 larvae per condition at 7 (**A**) and 14 (**C**) dpf. (**B, D**) Quantification of total distance across the whole experiment, in light or in dark conditions, and luminance perception index quantification at 7 (**B**) and 14 (**D**) dpf. Data are presented as mean ± SD.*

5.3.Neuron morphology characterization

Being NLGN2 a structural protein for the postsynaptic neuronal compartment, we wondered whether this could reflect in alterations in the morphology of the neuronal anatomy. We thus adopted a consolidated protocol combining mosaic genetic expression of a green fluorescent reporter and neuron morphology reconstruction

using the transgenic line Tg(id2b:Gal4, UAS:mCherry) driving the expression on a population of periventricular pyramidal neurons (PyrNs).

5.3.1. Microinjections, screening, single neuron acquisition and reconstruction

To perform such analysis, a specific protocol for this purpose was established.
As shown in Figure 30, WT and mutant double transgenic Tg(id2b:Gal4, UAS-mCherry) fish carrying the *mitfa*$^{-/-}$ (*nacre*) eggs were injected with the UAS plasmid encoding for the membrane-targeted GFP. The embryos were then raised to 5 dpf and the larvae expressing both the background red (mCherry^{+}) and green fluorescence (GFP) were selected. As we can see, the mCherry signal given by the transgenic line labels a diffused population of neurons localized within the tectum, as well as in the cerebellum and portions of the notochord, accordingly to the previous papers in which this transgenic line was generated and characterized.
It is possible also to observe that the fish are characterized by red fluorescence at the level of the heart, which is given by the "*bleeding heart*" control marker present in the *id2b:Gal4* construct. In contrast, the expression pattern of the injected plasmid is effectively labeling a reduced number of *id2b*$^{+}$ neurons that, compared to the mCherry^{+} signal, clearly highlight the neuronal processes. Moreover, the injected plasmid still consistently labeled the notochord, facilitating the selection of positive fish.

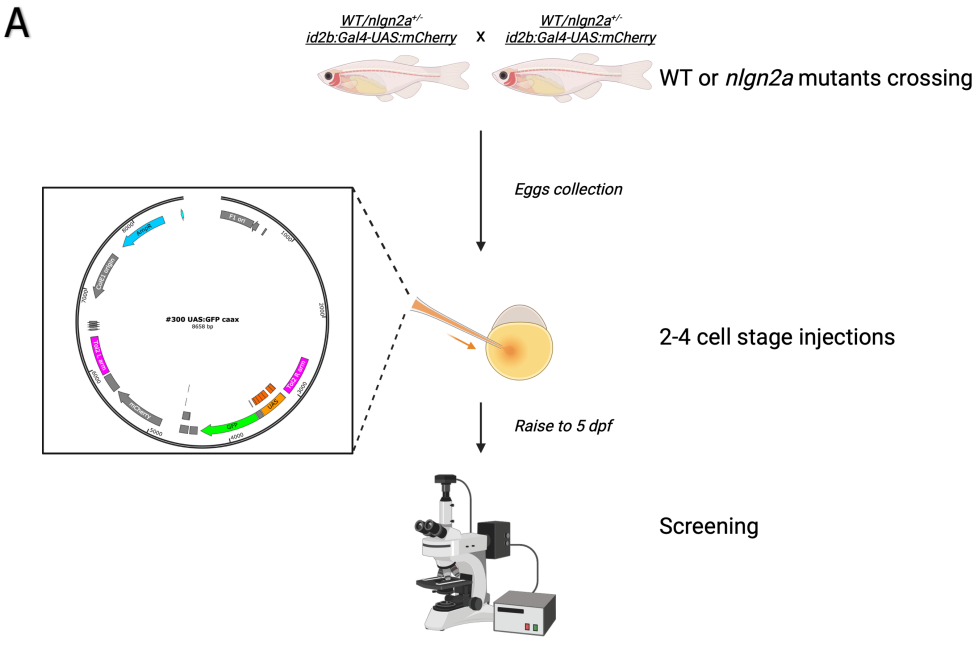

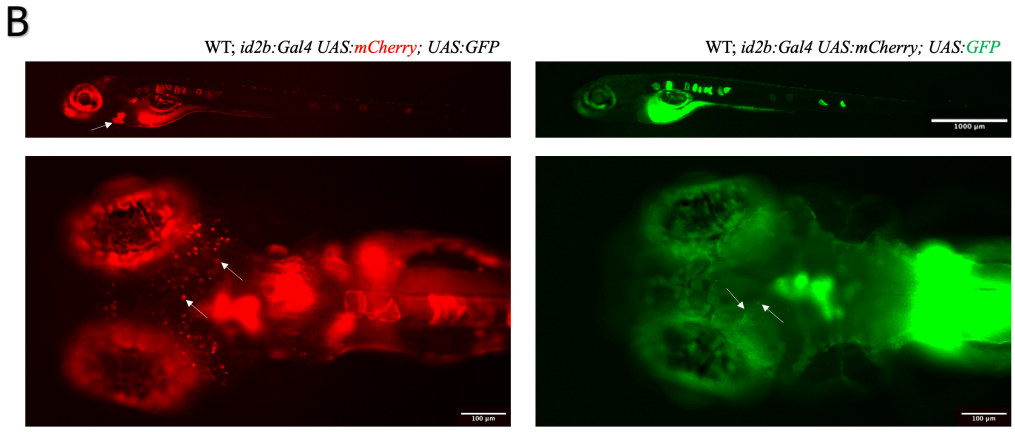

***Figure 30**: **Workflow for plasmid injection and screening**. (**A**) Schematic representation of microinjection protocol created with BioRender. Selected males and females were crossed, and newly hatched eggs were injected with a mix containing the UAS reporter plasmid. Then, larvae were raised to 5 dpf and screening at the fluorescent microscope for selection of positive fish was performed. (**B**) Lateral and dorsal views of 5 dpf WT double transgenic larvae expressing mCherry (on the left) and GFP (on the right) given by the injected plasmid. The arrow on the top left image indicates the red fluorescence expressed by the "bleeding heart" construct. The arrows on the bottom right image indicate the single neurons expressing the membrane-bound GFP.*

At 8 dpf, single neuron z-stack acquisition at the confocal microscope were performed and neuronal reconstructions were generated using Neutube software, as reported in Figure 31. The reconstructions were lately used to extract morphometry data.

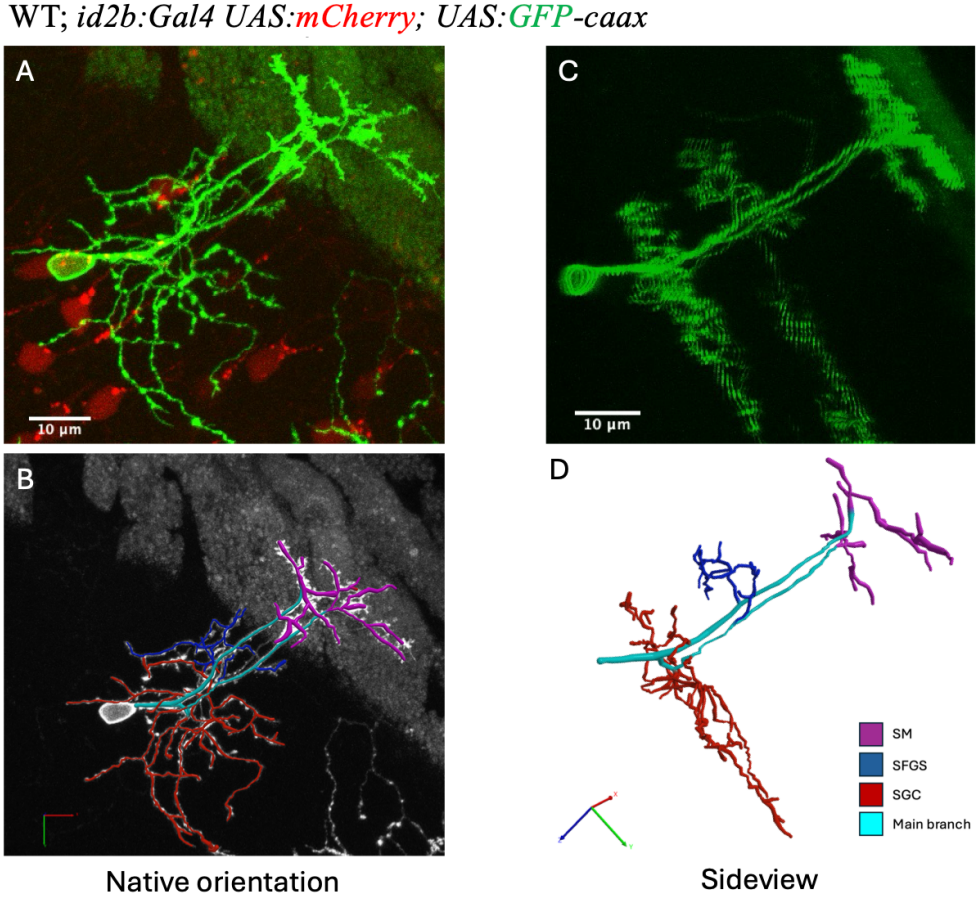

***Figure 31**: **Single neuron morphology and skeletonized reconstruction using Neutube**. (**A**) Maximal pojection image of an 8 dpf WT Tg(id2b:Gal4, UAS:mCherry) neuron expressing GFP for membrane targeting*

*in native orientation. (**B**) Maximal projection of the same neuron overlayed with the reconstruction generated with Neutube. (**C**) Sideview rotation of the neuron to identify the typical tristratified morphology consisting of two dendritic arbors and one axonal arbor targeting different layers of the neuropil; the most apical one is localized in stratum marginale (SM), the basal one in the stratum fibrosum and griseum superficiale (SFGS) and the axonal projections localized in stratum griseum centrale (SGC). (**D**) Sideview rotation of the skeletonized reconstruction of the same neuron generated with Neutube.*

5.3.2. Neuronal morphology alterations in *nlgn2a* mutants

In order to verify whether the mutation on *nlgn2a* was affecting the neuronal architecture, a series of morphometric parameters were evaluated in WT, *nlgn2a*$^{+/-}$ and *nlgn2a*$^{-/-}$ 8 dpf zebrafish. The first parameters, and the broader, considered were the retinotopic area for each layer, defined as the arbor-specific convex hull area, and the total length of branches in each layer.

The plots shown in Figure 32 highlight a significant decrease in the retinotopic area only in *nlgn2a*$^{-/-}$ mutants in the deepest tectal neuropil layer, the SGC, constisting of axonal projections of the PyrN. In contrast, the dendritic arbors localized in the SM and SFGS do not show significant differences with respect to the WT.

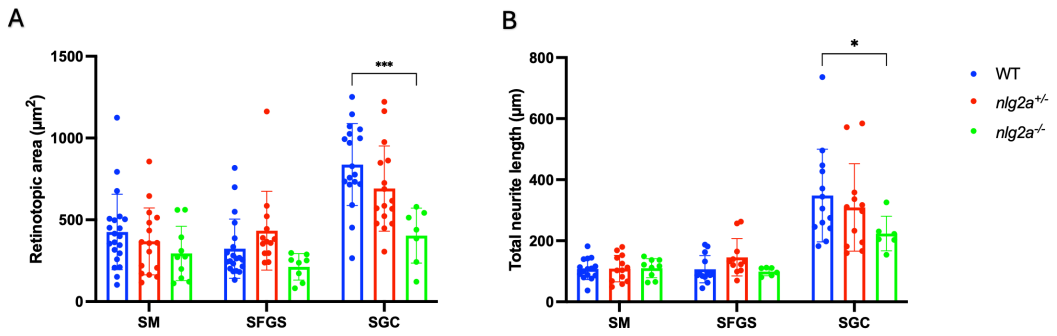

***Figure 32**: **nlgn2a$^{-/-}$ mutants exhibit reduced retinotopic area and total neurite length in the axonal compartment**. (A) Quantification of retinotopic area in each tectal layer in WT (n = 21), nlgn2a$^{+/-}$ (n = 13-16) and nlgn2a$^{-/-}$ (n = 7-10) mutants. (B) Quantification total neurite length in each tectal layer in WT (n = 12-15), nlgn2a$^{+/-}$ (n = 13-14) and nlgn2a$^{-/-}$ (n = 6-9). Data are presented as mean ± SD*

Accordingly, the total length of the branches in the SGC layer is significantly decreased in *nlgn2a*$^{-/-}$. Two other morphometric parameters considered were the spine density in the SM and the mean neurite length for each layer.

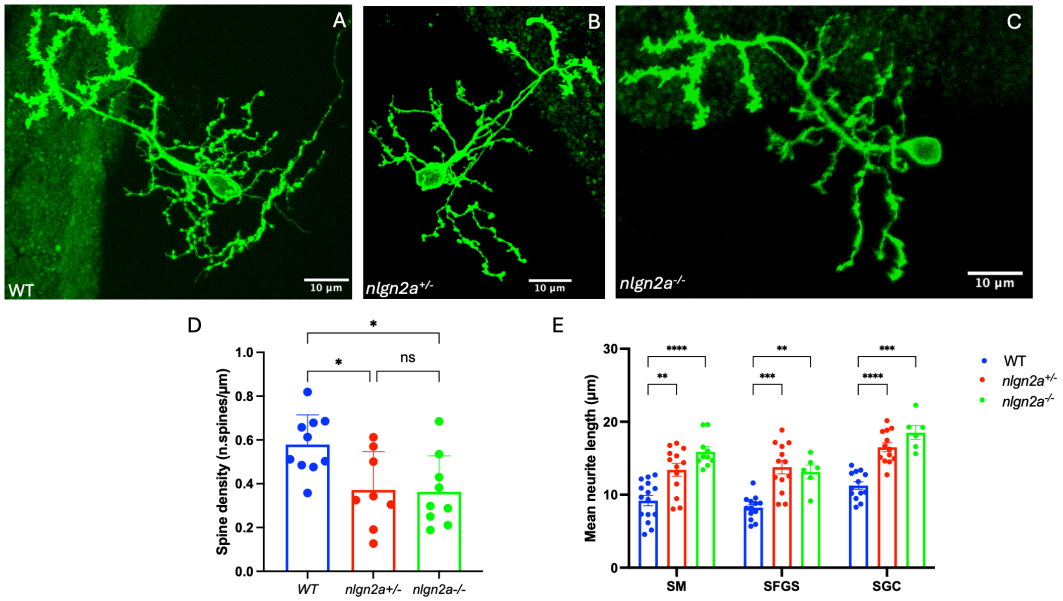

***Figure 33**: **nlgn2a mutants exhibit reduced spine density in SM and increased mean length of neurites**. (**A-C**) Representative images of 8 dpf WT, nlgn2a$^{+/-}$ and nlgn2a$^{-/-}$ single neurons expressing GFP in the membrane. (**D**) Quantification of spine density in SM, defined as the ratio between the number of spines and the total length of the SM arbor, in WT (n = 10), nlgn2a$^{+/-}$ (n = 8) and nlgn2a$^{-/-}$ (n = 9). (**E**) Quantification of mean neurite length across WT (n =15-19), heterozygous (n = 15) and homozygous (n = 7-10) nlgn2a mutants in SM, SFGS and SGC layers. Data are presented as mean ± SD.*

As shown in Figure 33, the spine density is significantly decreased in both homozygous and heterozygous mutants, as well as the mean neurite length value.
To verify whether the latter value was caused by a simpler branching architecture of the mutants, a Strahler analysis on the skeletonized reconstructions was performed.
As shown in Figure 34, the average bifurcation ratio in *nlgn2a*$^{+/-}$ and *nlgn2a*$^{-/-}$ mutants is significantly lower compared to the WT, suggesting a reduced arbor complexity.

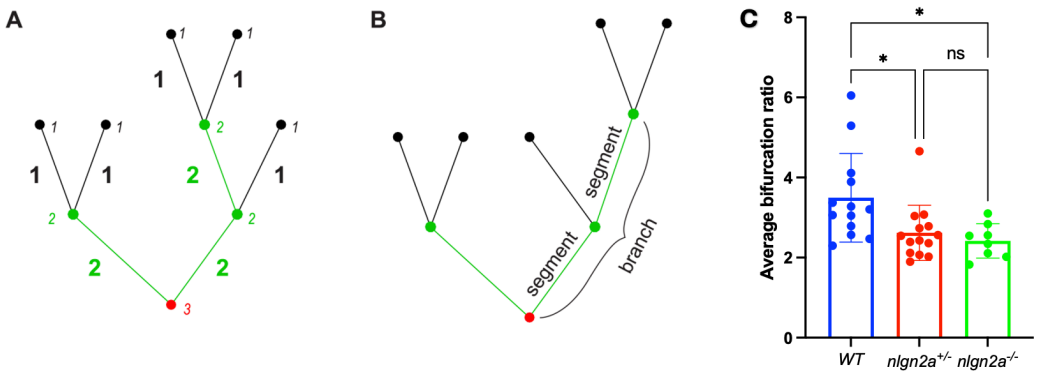

***Figure 34**: **nlgn2a mutants exhibit reduced bifurcation ratio**. (**A-B**) Schematic representation of Strahler branch ordering and differences between segments and branch. (**C**) Quantification of average bifurcation ratio in WT (n = 13), nlgn2a$^{+/-}$ (n = 14) and nlgn2a$^{-/-}$ (n = 8). Data are presented as mean ± SD.*

Taken together, these data indicate that the mutants are characterized by structural defects compared to the WT, specifically in the retinotopic organization of the axonal portion of the neuron. Along with these features, mutants are also characterized by reduced spine density in the SM layer and an increased mean length of the branches throughout all the three layers. Finally, Strahler analyses revealed that the general branching complexity of the mutants seems to be less complex compared to the WT.

5.4.Synaptic structure alterations in *nlgn2* mutants

To characterize also the alterations occurring at the synaptic level, Transmission Electron Microscopy was performed to evaluate the extension of the synaptic active zones in WT, *nlgn2a*$^{-/-}$ and *nlgn2b*$^{-/-}$ mutants at 8 and 11 dpf timepoints.
Zebrafish brain slices were included in epoxy resin and thin sections were obtained. The acquisition focused on the tectal neuropil, and a series of electron micrographs (~40 per condition) were obtained.
The criteria for the selection and definition of the active zones were:

- Presence of an electron-dense region.
- Presence of presynaptic vesicles close to the electron-dense region.
- Presence of two visible membranes delimiting the presynaptic and postsynaptic compartments.

As shown in Figure 35, both the mutants are characterized by a reduced extension of the active zones (AZs). Moreover, the *nlgn2b*$^{-/-}$ AZs appear less electron-dense, a feature observed also in 11 dpf samples.

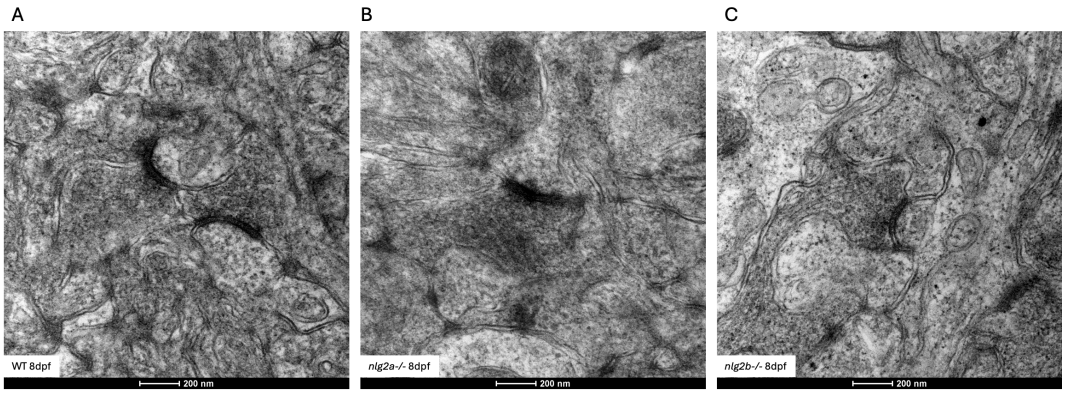

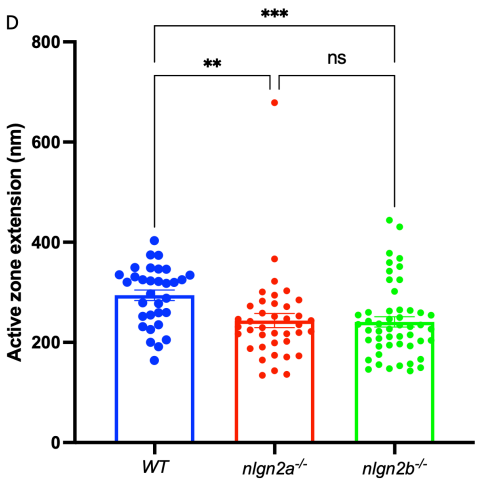

***Figure 35**: **nlgn2 mutants exhibit reduced extension of the synaptic active zone at 8 dpf**. (**A-C**) Representative TEM images of 8 dpf WT, nlgn2a$^{-/-}$ and nlgn2b$^{-/-}$ active zones. (D) Quantification of electron-dense synaptic active zone extension among the three genotypes. Data are presented as mean ± SD.*

In fact, at 11 dpf, the AZ extension is still significantly reduced, when comparing the WT with the mutants, and the intensity of the signal in *nlgn2b*$^{-/-}$ mutants is still visibly lower compared to WT and *nlgn2a*$^{-/-}$.

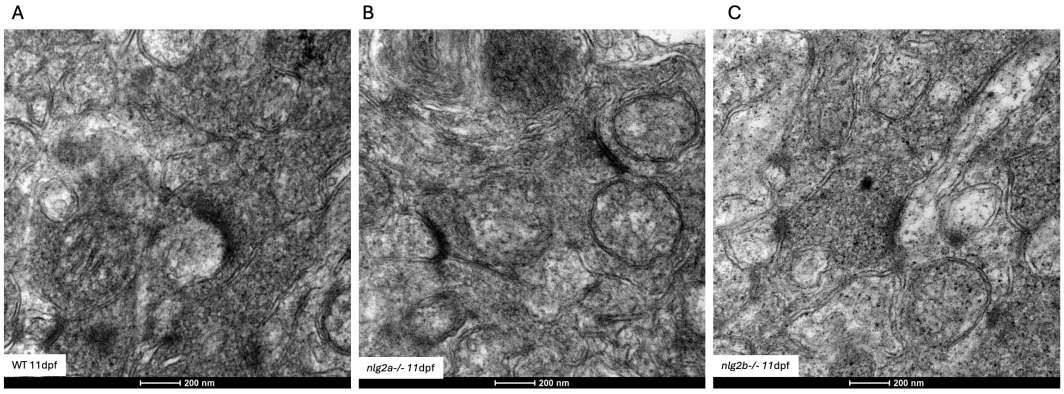

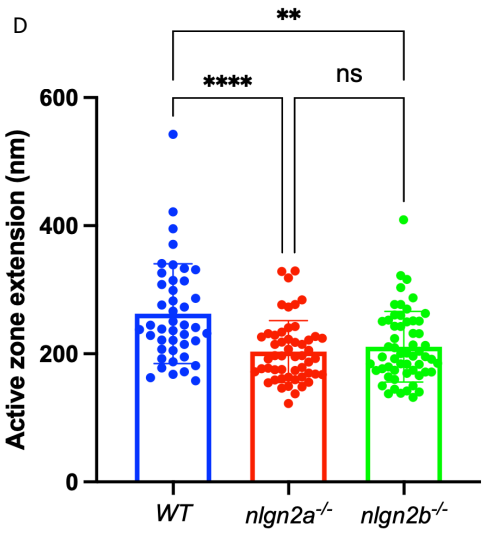

***Figure 36**: **nlgn2 mutants exhibit reduced extension of the synaptic active zone at 11 dpf**. (A-C) Representative TEM images of 11 dpf WT, nlgn2a$^{-/-}$ and nlgn2b$^{-/-}$ active zones. (D) Quantification of the electron-dense synaptic active zone extension among the three genotypes. Data are presented as mean± SD.*

5.5. Analysis of the spontaneous activity at 7 dpf in *nlgn2a*$^{-/-}$ fish

To investigate possible alteration in the brain dynamics associated with the *nlgn2a* mutation we took advantage of a cross with elavl3:H2B-GCaMP6s fish, constitutively expressing the fluorescence based neuronal activity reporter GCaMP6s in all CNS neurons. We used a custom multiphoton microscope to reconstruct whole brain activity at cellular resolution, as described in the Methods section. Resting-state calcium imaging revealed altered network dynamics in *nlg2a*$^{-/-}$ mutants compared to WT controls, characterized by prominent and highly synchronized population bursts. Spectral analysis (PSD) of the whole brain confirmed a global increase in oscillatory power in mutants, which was particularly prominent in the infra-slow frequency band (ISO, < 0.1 Hz). Regional quantification demonstrated that this ISO hyper-synchronization is a robust, brain-wide phenotype. Region-specific analysis and 3D spatial mapping revealed large negative effect sizes ($d < -0.8$) across virtually all analyzed macro-regions, indicating a strong dominance of infra-slow power in the mutant group. A similar, though slightly more variable, increase in oscillatory power was also observed in the slow oscillation band across most brain regions.

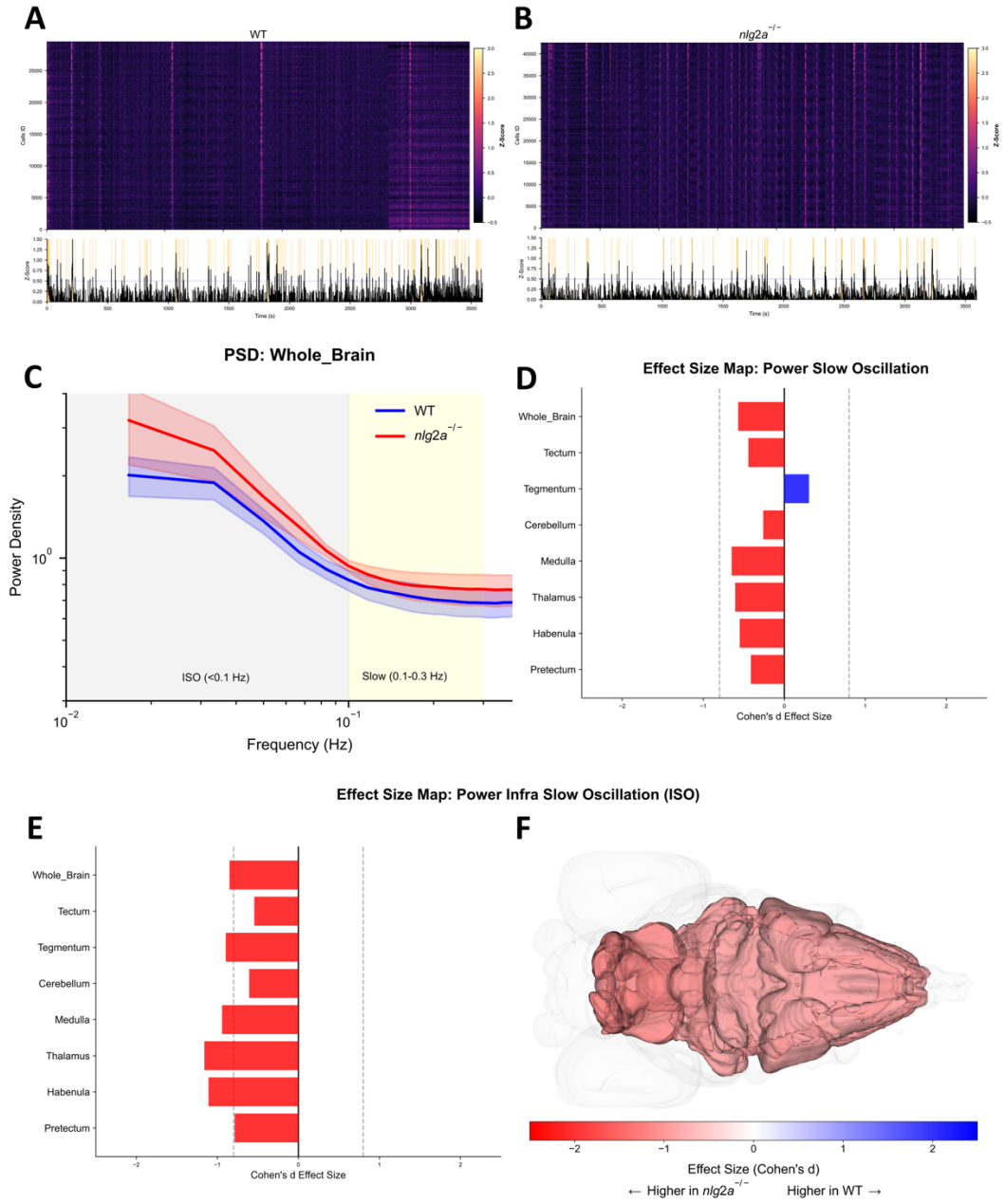

***Figure 37**: **Altered baseline network activity and increased infra-slow oscillatory power in nlg2a$^{-/-}$ mutants**. (**A, B**) Representative raster plots of Z-scored calcium activity from individual cells in a WT (**A**) and a nlg2a$^{-/-}$ mutant (**B**). Bottom traces show the continuous population mean over time, with synchronized network bursts highlighted in orange. (**C**) Average Power Spectral Density (PSD) of the whole brain. Shaded backgrounds define the Infra-Slow (ISO, < 0.1 Hz) and Slow (0.1–0.3 Hz) frequency bands. Solid lines represent the group mean ± SEM. (**D, E**) Regional quantification of Cohen's d effect size for Slow (**D**) and ISO (**E**) oscillatory power. The vertical dashed lines at ±0.8 mark the standard threshold for a "large"; effect size. Red bars indicate a negative Cohen's d (effect driven by mutants), while the blue bar indicates a positive Cohen's d (effect driven by WT). (**F**) 3D spatial map visualizing the Cohen's d effect size for ISO power across the brain. The red color gradient highlights regions with higher oscillatory power in nlg2a $^{-/-}$ mutants.*

5.6. Establishment of UAS:FingR transgenic lines for synapse imaging

The last aim of this project was that of generating two new transgenic lines capable of fluorescently label different types of synapses, with objective to evaluate possible alteration in the neuronal input-output relationship and the frequency of synaptic puncta associated with the mutations and the neuronal type, i.e. excitatory or inhibitory

In particular, we adopted an approach genetically target excitatory synapses through PSD95, and inhibitory ones through gephyrin, a known interactor of NLGN2, using the FingR strategy introduced by Son et al.. To establish these lines, as described in the methods, we performed a first *E. coli* transformation was performed in order to obtain highly concentrated plasmid vials, reported in Table 14

Plasmid	**Colony #**	**Plasmid concentration**
UAS:FingR-PSD95-eGFP	#1	270.9 ng/µl
UAS:FingR-PSD95-eGFP	#2	228.3 ng/µl
UAS:FingR-GPHN-mKate	#1	202.2 ng/µl
UAS:FingR-GPHN-mKate	#2	392.3 ng/µl

***Table 15**: Resulting plasmid DNA concentration after Midi kit extraction.*

We confirmed the correct genomic content of the plasmids, by means of an incubation with the HindIII restriction enzyme was performed. The samples transformed with the same plasmid but belonging to different colonies showed the same number and dimension of bands, suggesting successful integration (Figure 38). Moreover, injection of id2b:Gal4 zebrafish eggs with the membrane-localized UAS:TdTomato, along with UAS:FingR-PSD95-eGFP plasmid, resulted in an expected pattern of expression, with colocalization of the eGFP puncta with the neuronal processes, especially in the SM layer (Figure 39).

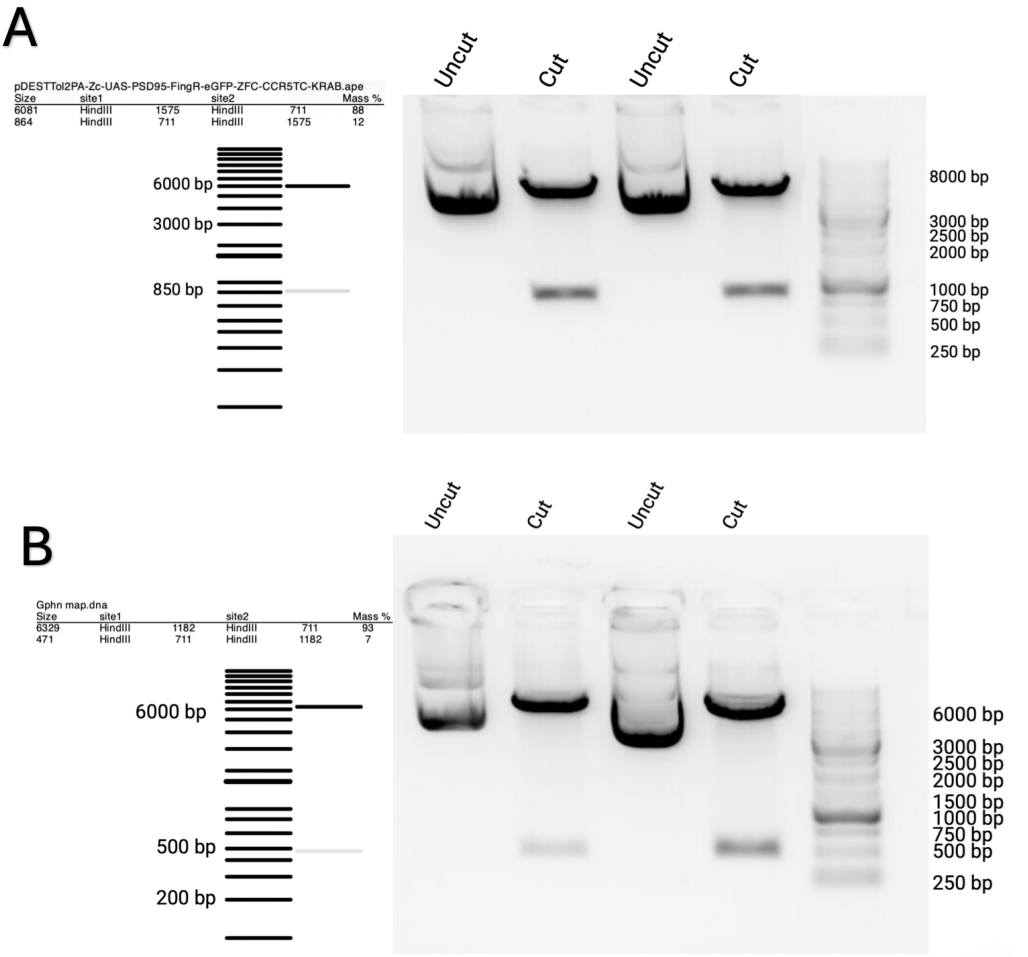

Figure 38: Resulting gel image of restriction enzyme digestion for the UAS:FingR plasmids previously amplified. *For each bacterial colony, a sample incubated with the restriction enzyme was prepared, as well as a control sample not incubated with it. (**A**) ApE predicted number and dimension of bands after HindIII digestion (left) and resulting gel images (right) of 2 colonies transfected with the UAS:FingR-PSD95 plasmid before (uncut) and after (cut) incubation. (**B**)ApE predicted number and dimension of bands after HindIII digestion (left) and resulting gel images (right) of 2 colonies transfected with the UAS:FingR-GPHN plasmid before (uncut) and after (cut) incubation.*

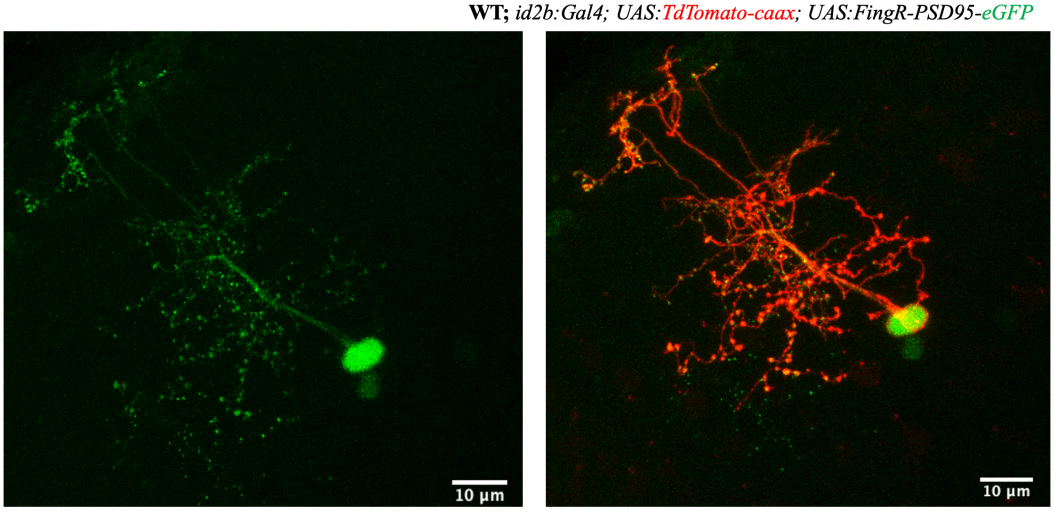

***Figure 39**: **FingR-PSD95-eGFP plasmid validation.**. Maximal projection image of an 8 dpf WT id2b:Gal4 larva injected with the membrane-localized UAS: TdTomato-caax plasmid and the UAS:FingR-PSD95-eGFP plasmid. On the left the green fluorescence channel, on the right the overlayed image with green and red fluorescent signal.*

Zebrafish eggs from WT *nacre* background injected with the plasmid at 2-4 cell stage were then raised to 1 month age, when via PCR genotyping we identified the founders (F_0). A number of FingR-GPHN and FingR-PSD95 positive F0 founders were identified, confirming successful microinjection and integration.

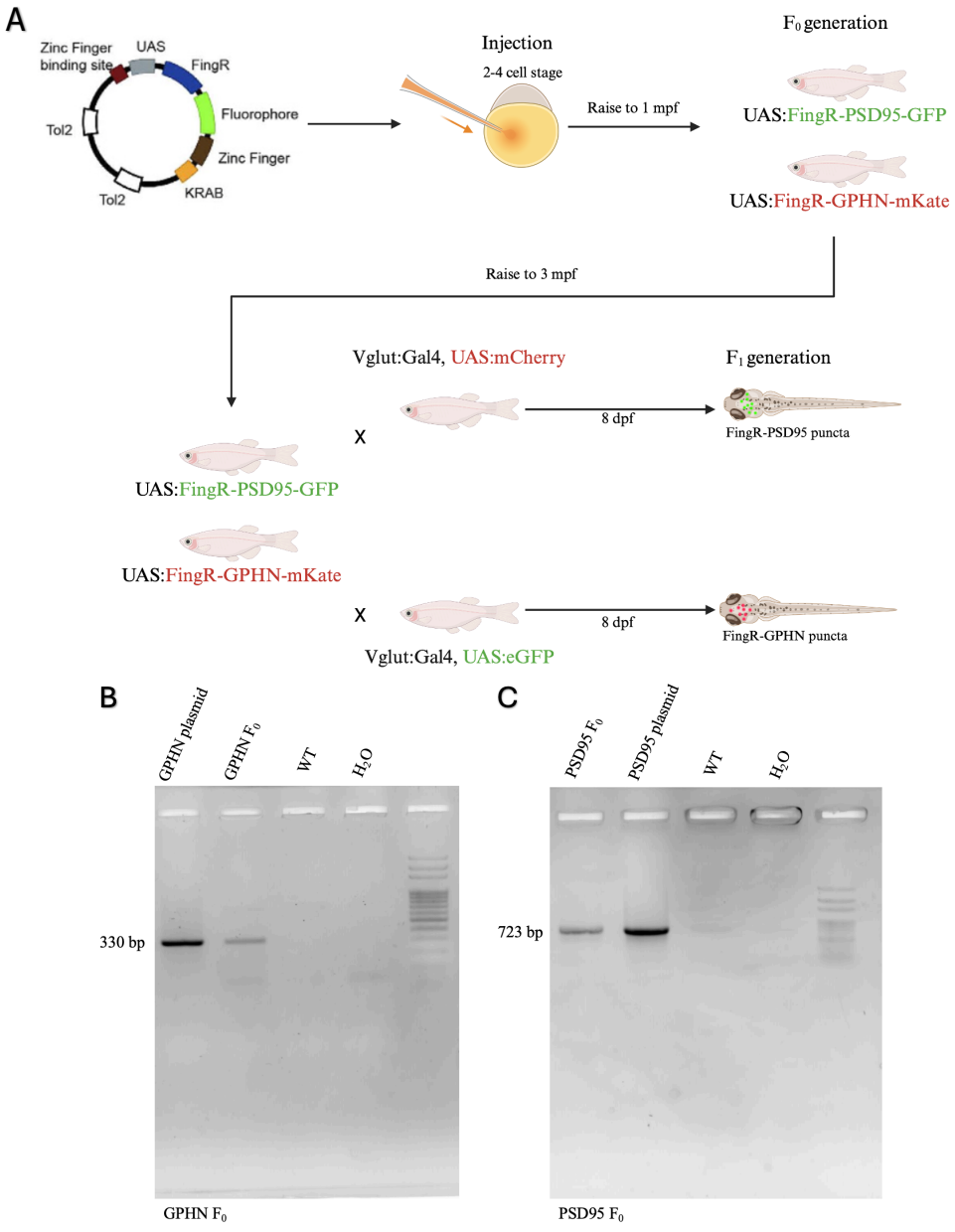

***Figure 40**: **Workflow for generation of UAS:FingR transgenic fish lines and selection of F_0 fish**. (A) Schematic representation of the strategy adopted to establish the two new lines. (B-C) Representative images of the PCR products obtained from 1 mpf old F_0 samples. The PCR included also three controls: the purified plasmid (biological and technical positive), the WT (biological negative) and H2O (technical negative), as well as a DNA marker on the right. The height of the F_0 samples bands correspond to the respective plasmid and of the expected size.*

Positive individuals were then raised to sexual maturity (~3 months age) and each one, separated from the others, was crossed with WT *nacre* fish. This was done to

verify whether the founder (F_0) fish were effectively capable of transmitting the transgene to the offspring (F_1)

The eggs were then collected and larvae raised to 5 dpf. At this time point, PCR genotyping was performed on pools of ~10 larvae from each breeding. This was done to verify whether the founder (F_0) fish were effectively capable of transmitting the transgene to the offspring (F_1) The F_0 offspring fish expressing the construct were further selected for confocal imaging.

At this stage, the properly identified F_0 founders were crossed with *vglut2a:gal4 (TgBAC(slc17a6b:GAL4FF)*, a line that expresses the Gal4 transcription factor and the associated UAS:mCherry fluorescence in glutamatergic neurons, providing a strong fluorescent signal. Larvae were then raised to 8 dpf and finally the presence of fluorescence associated with the construct was verified using confocal microscopy. For each plasmid, a z-stack of the optic tectum was acquired and subsequently genotyping was performed to confirm the presence of the construct.

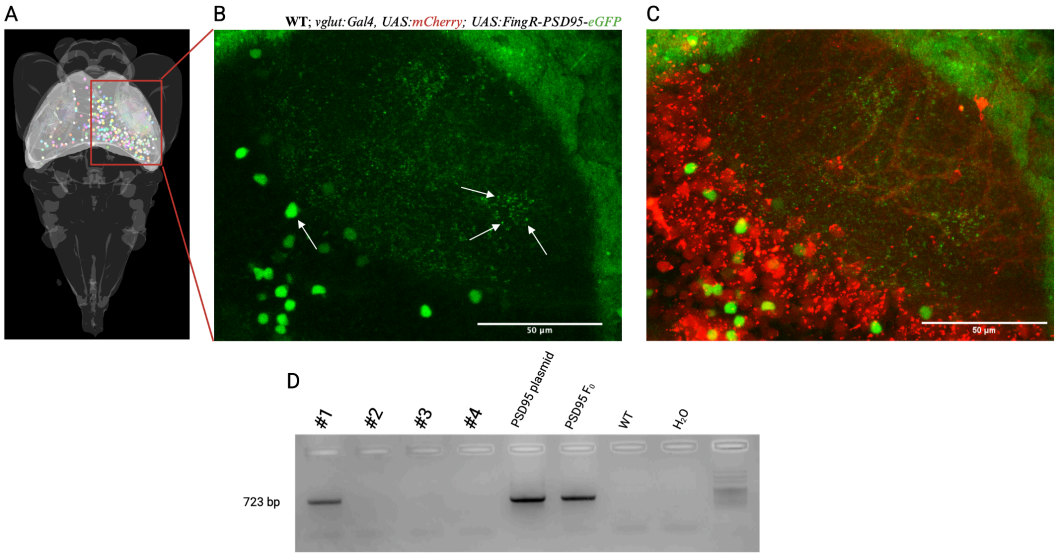

***Figure 41**: **Validation of the UAS:FingR-PSD95-eGFP line**. (**A**) Schematic representation of the region of the optic tectum from which the z-stack was acquired visualized in the Max Planck zebrafish Brain Atlas. (**B**) Maximal projection image of a 8 dpf WT transgenic larva expressing vglut:Gal4 and positive for both mCherry and FingR-PSD95, the image shows only the green channel fluorescence. (**C**) Same image of panel B, overlayed with the red fluorescence provided by UAS:mCherry (**D**) Resulting gel image of PCR products from the positive fish in panel B (#1), together with three non-fluorescent samples (#2-4). Together with these samples, two positive (plasmid and F_0 fish tail) and two negative (WT not fluorescent and H2O) controls were added. On the right, the DNA marker.*

The eGFP expression, given by the UAS:FingR-PSD95 construct, labels the soma of the neurons at high levels and a set of puncta along the neurites, mostly at the neuropil region, where the RGC axons and PVN dendrites are interacting, representing the sites where excitatory synapses are localized in the neuronal cell labelled.

The effective presence of the construct was also verified through genotyping, showing that the acquired fish was in fact expressing the transgene, in contrast to the other fish which did not show eGFP signal.
As for the UAS:FingR-GPHN-mKate transgene, transient expression did not result in any clear detectable fluorescence pattern. However, the established cross between Tg(vglut:Gal4; UAS:GFP) and F_0 founders Tg(UAS:FingR-GPHN-mKate) allowed to detect the outline of the neuron soma in red and several red puncta in the neuropil, although far less frequent and intense with respect to the Tg(vglut:Gal4; UAS:mCherry; UAS-FingR-PSD95-eGFP) fish.

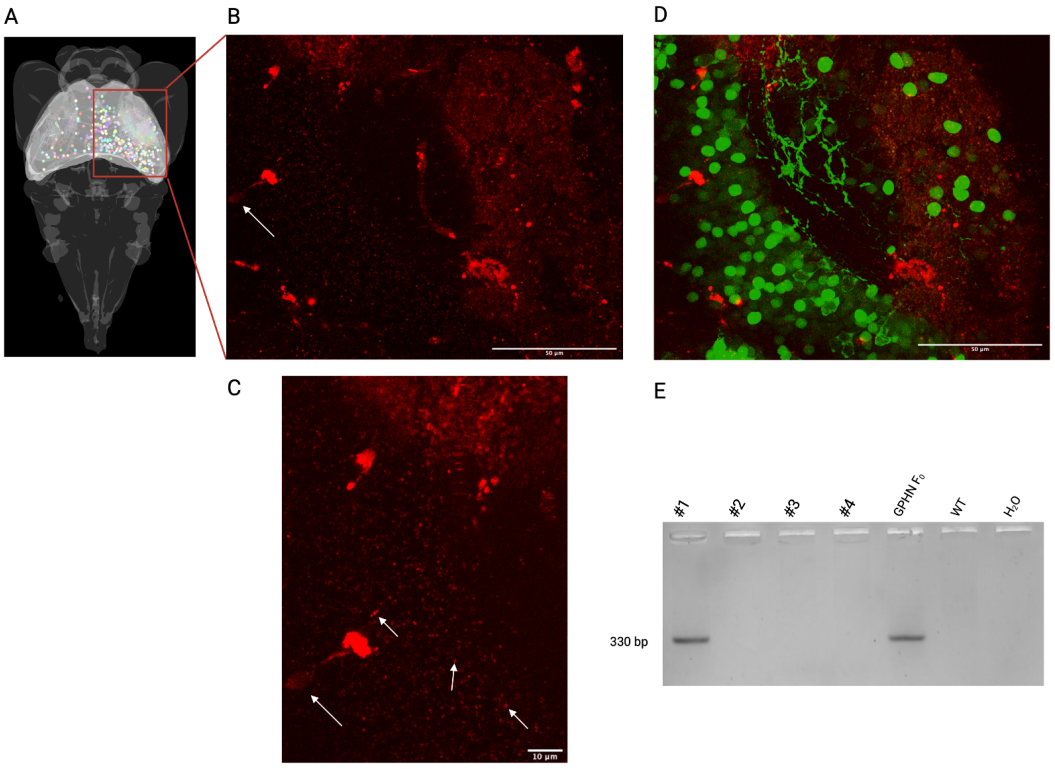

***Figure 42**: **Validation of the UAS:FingR-GPHN-mKate line**. (**A**) Schematic representation of the region of the optic tectum from which the z-stack was acquired visualized in the Max Planck zebrafish Brain Atlas. (**B**) Maximal projection image of an 8 dpf WT transgenic larva expressing vglut:Gal4 and positive for both GFP and FingR-GPHN. The soma expressing mKate is highlighted by the white arrow. (**C**) Enlarged view of the same mKate+ neuron. It is possible to visualize the soma and the initial part of the main process. The white arrows highlight also the distinct mKate punctae. (**D**) Same image of panel B, overlayed with the red fluorescence provided by UAS:GFP. (**E**) Resulting gel image of PCR products from the positive fish in panel B (#1), together with three non-fluorescent samples (#2-4). Together with these samples, one positive (F_0 fish tail) and two negative (WT not fluorescent and H2O) controls were added.*

5.7.Gene Ontology (GO) enrichment analyses for *nlgn2* mutants

Finally, a single-cell RNA sequencing was performed on 21 dpf WT, *nlgn2a*$^{-/-}$ and *nlgn2b*$^{-/-}$ brains to identify differentially expressed genes and the cellular components where they are expressed.

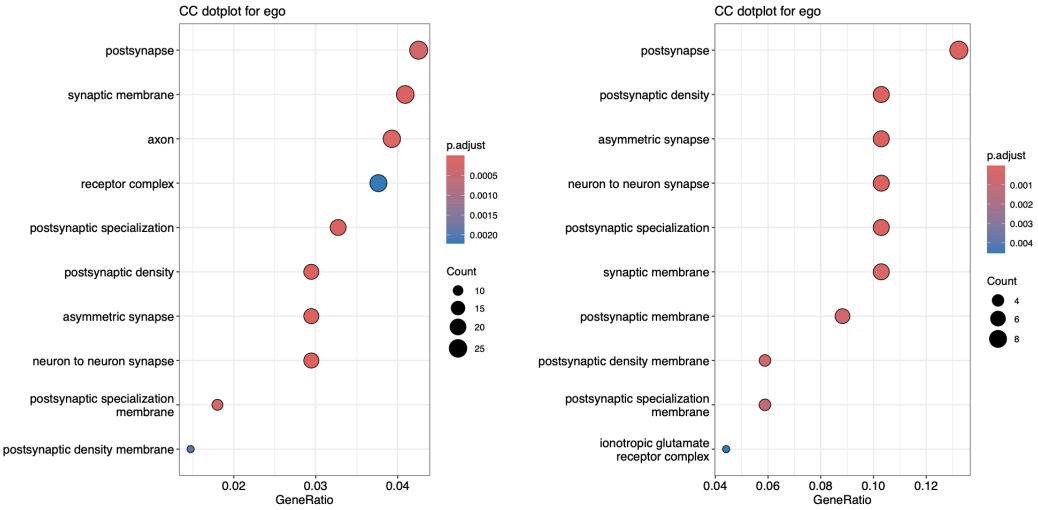

WT vs *nlgn2a*$^{-/-}$ WT vs *nlgn2b*$^{-/-}$

***Figure 43**: Gene onthology (GO) analysis of cellular components for differentially expressed genes (DEGs) in different cellular components in neuronal cells. The x-axis reports the gene ratio, while the dots indicate the number of genees contributing to each term. On the left, dotplot of cellular component enrichment analysis for nlgn2a$^{-/-}$. On the right, the same plot for nlgn2b$^{-/-}$.*

Both mutants are enriched for terms relative to the postsynaptic compartment organization and specialization, as well as the axon, suggesting an altered regulation of synaptic assembly and branch architecture (Figure 43).

Focusing on the most significantly differentially expressed genes (Figure 44), we can notice that *nlgn2a* mutants show differential expression of specific genes involved in synapse specification and architecture. For example, *shank1* is a major postsynaptic density scaffold protein, often mutated in ASD. Another key postsynaptic component differentially expressed in the mutants is *dlg4b*, the gene encoding PSD95, localized in excitatory synapses

Moreover, also *gap43*, a gene involved in neurite growth, is upregulated in both mutants. Also, *gabra3*, encoding the alpha-3 subunit of the GABA receptor, is upregulated in both mutants.

In *nlgn2b* mutants, subunits of the AMPA receptors are affected, such as *gria2b* and *gria4a.* It is possible to notice that also *srgap2*, a regulator of both excitatory and inhibitory synapse maturation and density, is upregulated.

Taken together, these preliminary results suggest an effect of the mutation of neuroligin-2 in the network regulating synapse organization and transmission in both excitatory and inhibitory compartments.

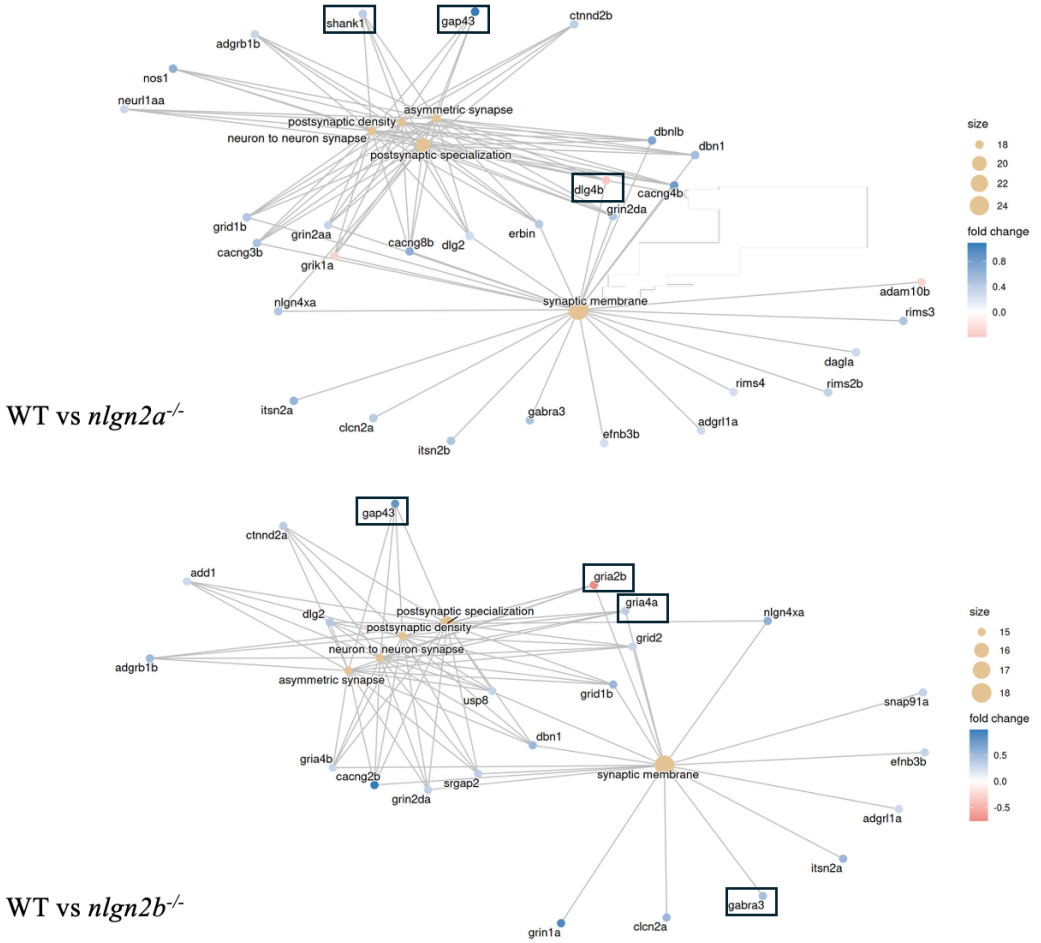

***Figure 44*: GO cellular component enrichment networks for differentially expressed genes in neural cells of nlgn2 mutants**. *The network plots display enriched GO cellular component terms for DEGs in nlgn2a$^{-/-}$ (top) and nlgn2b$^{-/-}$ (bottom). The central nodes represent the enriched cellular compartments observed in figure 43, with each gene involved in the term linked represented by a smaller node. The color-code indicated the log2FC (blue upregulated, red downregulated). The genes described in the paragraph are highlighted by the black rectangle*

6. DISCUSSION AND CONCLUSIONS

6.1. Discussion

This thesis aimed at characterizing two novel *nlgn2* mutant lines generated with CRISPR-Cas9 to dissect the contribution of this gene at different levels, from the gross anatomical parameters up to gene expression alterations. The effective reduced *nlgn2a* and *nlgn2b* expression levels were confirmed with RT-qPCR, excluding also the occurrence of compensatory mechanisms. Obviously, this downregulation can be confirmed only at the transcriptional level and does not rule out the presence of alternative splicing variants that do not include the premature stop codon. To assess whether also the protein levels are reduced or completely absent, a Western Blot assay with an effective zebrafish NLGN-2 antibody will be needed. Only after that, these two lines could be defined as either knockdown (KD) or knockout (KO). So far, unfortunately, the two NLGN-2 antibodies evaluated did not result in an un-ambiguous and specific labelling

When we evaluated the survival capability and features of microcephaly in both mutants. Even though with different extents and persistency, these results suggest that the mutations could contribute to neurodevelopmental delays or defects, core features of ASD pathology [5].

For the functional and behavioral aspects, we observed that *nlgn2* mutants are characterized by dysregulated light-dependent locomotor activity. In particular, at 7 dpf *nlgn2a*$^{-/-}$ fish are characterized by a significantly decreased luminance perception index. Zebrafish larvae show phototaxis behavior and a bias toward a darker environment act as anxiogenic stimulus, resulting in increased locomotor activity. In this sense the activity patterns, specifically of 7 dpf nlgn2a$^{-/-}$, could be interpreted in two ways. The first interpretation could propose a defective sensorimotor integration of the luminance stimulus, a process often defective in ASD. Alternatively, the altered photo-response pattern could arise from a hyperactivity feature of mutants, testified also by the increased distance covered in light in both genotypes and timepoints (except for the 14 dpf nlgn2a$^{-/-}$ mutants). This interpretation could support the idea of an altered E/I balance that is, among other things, a typical feature of ASD and a proposed downstream effect of *nlgn2* mutations [3]. We performed a preliminary functional characterization analyzing the brain spontaneous activity in *nlgn2a* mutants. As a result, PSD analysis highlighted that the infra-slow (ISO, <0.1 Hz) and slow (SO, 0.1-0.3 Hz) oscillations in mutants have a brain-wide higher contribution to the overall signal variance. This can be interpreted as hyper synchronization of the network at very

low frequencies. As a conclusion, the mutant brain appears majorly influenced by large-scale state transitions occurring over long time-scales.
Obviously, these are preliminary functional information, and two-photon functional Ca^{2+} imaging coupled with visual stimuli presentation will provide a deeper understanding of the circuit-level alterations occurring in the brain.
The use of the Tg(id2b:Gal4) line for the evaluation of PyrNs morphology in the tectum of *nlgn2a* mutants revealed an articulated pattern of alterations. First, the reduced extension and total length of the axonal compartment targeting the SGC layer could be indicative of defects in axon guidance and growth. Similar defects in axon growth have been observed in other mice models for neurodevelopmental disorders. For example, *chd8* deficient neurons, a well-known gene implicated in ASD, exhibit impaired axonal growth both *in vitro* and *in vivo* [45].
On the other hand, despite the general dendritic organization and extension of the processes targeting the SM and SFGS layers is not affected, the mean branch length is increased and the corresponding bifurcation ratio reduced, suggesting impairments in either new branch establishment or maintenance. These result in fact align with the biological role of NLGN2, an important structural component of the GABAergic synapse, needed for its stabilization and maintenance.
Interestingly, only apparently counterintuitive, we found a reduced spine density of mutant PyrNs labelled by *id2b*. In fact, dendritic spines are the main sites of excitatory input, while NLGN2 is exclusively localized in GABAergic synapses, so a regulation of those structures is strange. However, this result aligns with previous evidence in mice of the regulation of KCC2 by NLGN2, with reduced spine density observed in NL2shRNA transfected mature neurons. By contrast, the same indirect regulation mechanism in zebrafish has not been reported yet, thus further investigation is needed to confirm whether KCC2 is alternatively regulated also in zebrafish. Undoubtedly, the same morphological evaluation is needed also for the *nlgn2b* mutants, to verify whether the effects are similar.
From the analysis with Electron Microscopy, the reduced extension of the synaptic active zone in both mutants could suggest uncomplete stabilization or destabilization of the synaptic contacts, coherently with the previously mentioned role of NLGN2 in synapse maintenance. However, these analyses do not allow the discrimination of different excitatory and inhibitory synapses. Moreover, to definitively confirm whether this phenomenon is caused by defects in synapse maintenance or is caused by synaptic pruning that does not affect the transmission efficacy, electron micrographs with higher resolution should be acquired to evaluate the presynaptic vesicles density.
The scRNA-seq highlighted that, in mature neurons, several components of the synaptic membrane and its specialization are differentially expressed. The effects

of *nlgn2* mutation are not restricted solely to the inhibitory network (i.e. *gabra3*), but key players of excitatory transmission are affected, such as the PSD95 homolog (*dlg4b*), components of the NMDA glutamate receptors (*grik1a*, *grin2aa*, *gria4a*, *gria2b*), as well as genes associated with axonal and dendritic growth (*gap43*), confirming the anatomical data.

Taken together, these data suggest a broad downstream regulation of NLGN2, whose mechanism needs to be further investigated.

Finally, the generation of the two novel transgenic lines for excitatory and inhibitory synapse imaging will be useful in the study of synaptic dynamics of the mutants. In particular, quantify and compare the ratio between the density of excitatory and inhibitory synaptic puncta could further suggest alteration of the E/I balance.

6.2. Conclusions

In conclusion, this work demonstrated that the effects of *nlgn2* mutations range between different levels, from cellular to behavioral to anatomical aspects, and are coherent with several pathological traits associated with ASD.

These results thus place zebrafish and the relative *nlgn2* mutant lines as promising models for ASD modeling and characterization.

In the future, functional imaging through multi-photon microscopy will be fundamental in the investigation of the network dynamics and to determine whether E/I balance is actually altered.

Moreover, more in-depth behavioral assays focused on visuomotor adaptation, taking advantage of the OMR/OKR coupled with functional imaging, will provide a deeper understanding of the circuit level dynamics alteration occurring.

To summarize, and conclude, this work successfully laid the foundation for a first characterization of a gene predicted to have a role in ASD and identified several traits associated with it.

7. BIBLIOGRAPHY

1. Dietz PM, Rose CE, McArthur D, Maenner M. National and State Estimates of Adults with Autism Spectrum Disorder. *J Autism Dev Disord*. 2020;50(12):4258-4266. doi:10.1007/s10803-020-04494-4

2. Scattoni ML, Fatta LM, Micai M, et al. Autism spectrum disorder prevalence in Italy: a nationwide study promoted by the Ministry of Health. *Child Adolesc Psychiatry Ment Health*. 2023;17(1):125. doi:10.1186/s13034-023-00673-0

3. Ali H, Marth L, Krueger-Burg D. Neuroligin-2 as a central organizer of inhibitory synapses in health and disease. *Sci Signal*. 2020;13(663):eabd8379. doi:10.1126/scisignal.abd8379

4. Hirota T, King BH. Autism Spectrum Disorder: A Review. *JAMA*. 2023;329(2):157-168. doi:10.1001/jama.2022.23661

5. Sauer AK, Stanton JE, Hans S, Grabrucker AM. Autism Spectrum Disorders: Etiology and Pathology. In: Grabrucker AM, ed. *Autism Spectrum Disorders*. Exon Publications; 2021. Accessed February 3, 2026. http://www.ncbi.nlm.nih.gov/books/NBK573613/

6. Qin L, Wang H, Ning W, Cui M, Wang Q. New advances in the diagnosis and treatment of autism spectrum disorders. *Eur J Med Res*. 2024;29(1):322. doi:10.1186/s40001-024-01916-2

7. Wu Y, Cao H, Baranova A, et al. Multi-trait analysis for genome-wide association study of five psychiatric disorders. *Transl Psychiatry*. 2020;10(1):209. doi:10.1038/s41398-020-00902-6

8. Viggiano M, Ceroni F, Visconti P, et al. Genomic analysis of 116 autism families strengthens known risk genes and highlights promising candidates. *Npj Genomic Med*. 2024;9(1):21. doi:10.1038/s41525-024-00411-1

9. Klei L, Sanders SJ, Murtha MT, et al. Common genetic variants, acting additively, are a major source of risk for autism. *Mol Autism*. 2012;3(1):9. doi:10.1186/2040-2392-3-9

10. Iannuccelli M, Vitriolo A, Licata L, et al. Curation of causal interactions mediated by genes associated with autism accelerates the understanding of

gene-phenotype relationships underlying neurodevelopmental disorders. *Mol Psychiatry*. 2024;29(1):186-196. doi:10.1038/s41380-023-02317-3

11. Trobiani L, Meringolo M, Diamanti T, et al. The neuroligins and the synaptic pathway in Autism Spectrum Disorder. *Neurosci Biobehav Rev*. 2020;119:37-51. doi:10.1016/j.neubiorev.2020.09.017

12. Egawa J, Lemmon VP, Someya T. Editorial: Effects of autism spectrum disorder (ASD) risk genes on phenotypes of each hierarchy. *Front Neurol*. 2024;15. doi:10.3389/fneur.2024.1508494

13. Sun C, Zhang L, Chen G. An unexpected role of neuroligin-2 in regulating KCC2 and GABA functional switch. *Mol Brain*. 2013;6:23. doi:10.1186/1756-6606-6-23

14. Topchiy I, Mohbat J, Folorunso OO, Wang Z (Zephyr), Lazcano-Etchebarne C, Engin E. GABA System as the Cause and Effect in Early Development. *Neurosci Biobehav Rev*. 2024;161:105651. doi:10.1016/j.neubiorev.2024.105651

15. Peerboom C, Wierenga CJ. The postnatal GABA shift: A developmental perspective. *Neurosci Biobehav Rev*. 2021;124:179-192. doi:10.1016/j.neubiorev.2021.01.024

16. Bedell VM, Dubey P, Lee HB, et al. Zebrafishology, study design guidelines for rigorous and reproducible data using zebrafish. *Commun Biol*. 2025;8(1):739. doi:10.1038/s42003-025-07496-z

17. Doszyn O, Dulski T, Zmorzynska J. Diving into the zebrafish brain: exploring neuroscience frontiers with genetic tools, imaging techniques, and behavioral insights. *Front Mol Neurosci*. 2024;17. doi:10.3389/fnmol.2024.1358844

18. Arun G, Diermeier SD, Spector DL. Therapeutic Targeting of Long Non-Coding RNAs in Cancer. *Trends Mol Med*. 2018;24(3):257-277. doi:10.1016/j.molmed.2018.01.001

19. Peterson RT. Discovery of therapeutic targets by phenotype-based zebrafish screens. *Drug Discov Today Technol*. 2004;1(1):49-54. doi:10.1016/j.ddtec.2004.07.002

20. Garg V, Geurten BRH. Diving deep: zebrafish models in motor neuron degeneration research. *Front Neurosci*. 2024;18. doi:10.3389/fnins.2024.1424025

21. Davey C, Tallafuss A, Washbourne P. Differential expression of neuroligin genes in the nervous system of zebrafish. *Dev Dyn Off Publ Am Assoc Anat*. 2010;239(2):703-714. doi:10.1002/dvdy.22195

22. Neuhauss SCF. Zebrafish vision. 2010;29:81-122. doi:10.1016/S1546-5098(10)02903-1

23. Baier H, Scott EK. The Visual Systems of Zebrafish. *Annu Rev Neurosci*. 2024;47(Volume 47, 2024):255-276. doi:10.1146/annurev-neuro-111020-104854

24. Robles E, Laurell E, Baier H. The Retinal Projectome Reveals Brain-Area-Specific Visual Representations Generated by Ganglion Cell Diversity. *Curr Biol*. 2014;24(18):2085-2096. doi:10.1016/j.cub.2014.07.080

25. Robles E, Filosa A, Baier H. Precise Lamination of Retinal Axons Generates Multiple Parallel Input Pathways in the Tectum. *J Neurosci*. 2013;33(11):5027-5039. doi:10.1523/JNEUROSCI.4990-12.2013

26. Patterson BW, Abraham AO, MacIver MA, McLean DL. Visually guided gradation of prey capture movements in larval zebrafish. *J Exp Biol*. 2013;216(16):3071-3083. doi:10.1242/jeb.087742

27. Golzio C, Willer J, Talkowski ME, et al. KCTD13 is a major driver of mirrored neuroanatomical phenotypes of the 16p11.2 copy number variant. *Nature*. 2012;485(7398):363-367. doi:10.1038/nature11091

28. Zhang Y, Rózsa M, Liang Y, et al. Fast and sensitive GCaMP calcium indicators for imaging neural populations. *Nature*. 2023;615(7954):884-891. doi:10.1038/s41586-023-05828-9

29. Denk W, Strickler JH, Webb WW. Two-Photon Laser Scanning Fluorescence Microscopy. *Science*. 1990;248(4951):73-76. doi:10.1126/science.2321027

30. Aharon D, Marlow FL. Sexual determination in zebrafish. *Cell Mol Life Sci*. 2021;79(1):8. doi:10.1007/s00018-021-04066-4

31. Leyden C, Brüggemann T, Debinski F, Simacek CA, Dehmelt FA, Arrenberg AB. Efficacy of Tricaine (MS-222) and Hypothermia as Anesthetic Agents for Blocking Sensorimotor Responses in Larval Zebrafish. *Front Vet Sci*. 2022;9. doi:10.3389/fvets.2022.864573

32. Förster D, Arnold-Ammer I, Laurell E, et al. Genetic targeting and anatomical registration of neuronal populations in the zebrafish brain with a new set of BAC transgenic tools. *Sci Rep*. 2017;7(1):5230. doi:10.1038/s41598-017-04657-x

33. DeMarco E, Xu N, Baier H, Robles E. Neuron types in the zebrafish optic tectum labeled by an id2b transgene. *J Comp Neurol*. 2020;528(7):1173-1188. doi:10.1002/cne.24815

34. DeMarco EC, Stoner GR, Robles E. A genetic labeling system to study dendritic spine development in zebrafish models of neurodevelopmental disorders. *Dis Model Mech*. 2022;15(8):dmm049507. doi:10.1242/dmm.049507

35. Scheer N, Campos-Ortega JA. Use of the Gal4-UAS technique for targeted gene expression in the zebrafish. *Mech Dev*. 1999;80(2):153-158. doi:10.1016/S0925-4773(98)00209-3

36. Choy E, Chiu VK, Silletti J, et al. Endomembrane Trafficking of Ras: The CAAX Motif Targets Proteins to the ER and Golgi. *Cell*. 1999;98(1):69-80. doi:10.1016/S0092-8674(00)80607-8

37. Son JH, Keefe MD, Stevenson TJ, et al. Transgenic FingRs for Live Mapping of Synaptic Dynamics in Genetically-Defined Neurons. *Sci Rep*. 2016;6(1):18734. doi:10.1038/srep18734

38. Levy AM, Gomez-Puertas P, Tümer Z. Neurodevelopmental Disorders Associated with PSD-95 and Its Interaction Partners. *Int J Mol Sci*. 2022;23(8):4390. doi:10.3390/ijms23084390

39. Davis MW, Jorgensen EM. ApE, A Plasmid Editor: A Freely Available DNA Manipulation and Visualization Program. *Front Bioinforma*. 2022;2. doi:10.3389/fbinf.2022.818619

40. Kawakami K. Tol2: a versatile gene transfer vector in vertebrates. *Genome Biol*. 2007;8(1):S7. doi:10.1186/gb-2007-8-s1-s7

41. Facchinello N, Schiavone M, Vettori A, Argenton F, Tiso N. Monitoring Wnt Signaling in Zebrafish Using Fluorescent Biosensors. In: Barrett Q, Lum L, eds. *Wnt Signaling: Methods and Protocols*. Springer; 2016:81-94. doi:10.1007/978-1-4939-6393-5_9

42. Elliott AD. Confocal Microscopy: Principles and Modern Practices. *Curr Protoc Cytom*. 2020;92(1):e68. doi:10.1002/cpcy.68

43. Bruzzone M, Chiarello E, Albanesi M, et al. Whole brain functional recordings at cellular resolution in zebrafish larvae with 3D scanning multiphoton microscopy. *Sci Rep*. 2021;11(1):11048. doi:10.1038/s41598-021-90335-y

44. Feng L, Zhao T, Kim J. neuTube 1.0: A New Design for Efficient Neuron Reconstruction Software Based on the SWC Format. *eNeuro*. 2015;2(1). doi:10.1523/ENEURO.0049-14.2014

45. Xu Q, Liu YY, Wang X, et al. Autism-associated CHD8 deficiency impairs axon development and migration of cortical neurons. *Mol Autism*. 2018;9:65. doi:10.1186/s13229-018-0244-2

8. ACKNOWLEDGEMENTS

At first, I want to thank my parents and my whole family, for the unconditioned and always present support during these years of study, I hope this will be the first of many satisfactions I'll give you. A special thank goes to Sofia, the only person that helped and stood side by side with me even in the toughest times.
I want to sincerely thank my thesis supervisor Prof. Marco Dal Maschio and co-supervisor Prof. Nicola Facchinello. Thanks for introducing me to neuroscience research in the best manner I could have desired. With your always present support and patience, I had the possibility to learn both practically and mentally how research is conducted. This helped me refine my critical thinking and pushed me to ask myself many questions to which I would like to contribute giving a response in the future.
I wanted also to thank all the lab Dal Maschio group, especially dott. Marzia Frizzo for being a patient guide during the everyday work in the lab and a sincere friend outside it. I also would like to acknowledge dott. Marco Salamanca and dott. Marica Albanesi for the precious teachings and tips regarding the two-photon microscopy technique and for the analysis of the spontaneous activity.
I would like to thank Prof. Maria Elena Miletto Petrazzini for the coordination of the work regarding the scRNA-seq analysis and the group of Prof. Paolo Martini for the actual sequencing, data processing and GO analyses. I want to thank also Prof. Marco Mainardi for the suggestion about the employment and generation of the transgenic lines for excitatory and inhibitory synapse imaging in zebrafish.
Finally, my sincere thanks go to every relative, friend and colleague that has supported during this important period of my life, without your support I'm sure it would not have been possible to reach this goal, that I imagine as the beginning of a new chapter of my life.